

**ORGANIC-INORGANIC NANOCOMPOSITES FOR RENEWABLE  
ENERGY CONVERSION DEVICES**

A Dissertation  
Presented to  
The Academic Faculty

by

Jaehan Jung

In Partial Fulfillment  
Of the Requirements for the Degree  
Doctor of Philosophy in the  
School of Materials Science and Engineering

Georgia Institute of Technology

May 2015

**Copyright © Jaehan Jung 2015**

**ORGANIC-INORGANIC NANOCOMPOSITES FOR RENEWABLE  
ENERGY CONVERSION DEVICES**

Approved by:

Dr. Zhiqun Lin, Advisor  
School of Materials Science and  
Engineering  
*Georgia Institute of Technology*

Dr. Vladimir V. Tsukruk  
School of Materials Science and  
Engineering  
*Georgia Institute of Technology*

Dr. Dong Qin  
School of Materials Science and  
Engineering  
*Georgia Institute of Technology*

Dr. Elsa Reichmanis  
School of Chemical and Biomolecular  
Engineering  
*Georgia Institute of Technology*

Dr. Joseph W. Perry  
School of Chemistry and Biochemistry  
*Georgia Institute of Technology*

Date Approved: March 23, 2015

To my Family.

## ACKNOWLEDGEMENTS

During PhD studies, fortunately my journey was not alone and filled with many people who kindly support me and willingly help me both physically and spiritually.

First, I would thank my Advisor Professor Zhiqun Lin for all his kind support, insightful guidance, and encouragement during my Ph.D. life. Particularly, he guided and pushed me to try my best through my entire doctoral studies, while being understanding. I thank Prof. Vladimir Tsukruk, Prof. Dong Qin, Prof. Joseph Perry and Prof. Elsa Reichmanis for helping me to carry my dissertation to completion, and for providing me with valuable feedback.

I was very fortunate to have a chance to work with Dr. Xinchang Pang, who patiently taught me basic synthesis and guided me through the realm of polymer synthesis. Also I would like to greatly thank Young Jun Yoon for helping NMR related works and Ah-young Song for her help in IV characterization. They contributed significantly to the works in this thesis. I thank all current and former group members including Prof. Myunghwan Byun, Dr. Xukai Xin, Dr. Lei Zhao, Dr. Ming He, Chaowei Feng, Bo Li, Jame Icozzia, and many others for their help and warm friendship.

I would like to thank my collaborators: Sidney Malak for his help with transient absorption, Chun Hao Lin for helping PL related works, and Marcus J. Smith for helping analyzing TGA. The wonderful discussions and materials they provided greatly helped progress this project. I thank Dr. Kwang-sup Eom for giving a great influence in research

and being a great friend as well as for his help with XPS work and information on various topics in battery field, Jung Tae Lee for his valuable insight about batteries and TGA.

I would like to thank all of kind friends who have experience great adventure with me throughout my years here at Georgia Tech; Dr. Hangi Chae, Dr. Min Kyu Song, Dr. Min Sang Park, Dr. Il Tae Kim, Dr. Jung Hwa Park, Dr. Ikjun Choi, Dr. Beom Jin Yoon, Dr. Yoon Sang Kim, Dr. Doh-Yeon Park, Dr. Min Baek Lee, Dr. Sang Min Lee, Dr. Jung Pil Lee, Dr. Jung tae Lee, Dr. Kkotnim Oh, Dr. Minchul Chang, Dr. Sungjun Kim, Dong Chan Lee, Soo Kyung Kim, Jung Hyun Noh, Gyuhyon Lee, Youngho Jin, Yohan Park, Young jin Jang, Junhyuk Kim.

My parents have been truly supportive and encouraging during my Ph.D. studies, and even before that. I thank my parents for their endless love, sacrifices, and trust. Without their endless support, I would not have been able to achieve my degree.

# TABLE OF CONTENTS

<b>ACKNOWLEDGEMENTS</b> .....	iv
<b>LIST OF SCHEMES AND TABLES</b> .....	viii
<b>LIST OF FIGURES</b> .....	ix
<b>SUMMARY</b> .....	xvi
<b>1. Introduction</b> .....	1
<b>1.1. Motivation</b> .....	1
<b>1.2. Challenging</b> .....	2
<b>1.3. Research objectives</b> .....	4
<b>1.4. Map of dissertation</b> .....	5
<b>2. Organic-inorganic nanocomposites composed of conjugated polymers and semiconductor nanocrystals for photovoltaics</b> .....	6
<b>2.1. Introduction</b> .....	6
<b>2.2. Working principle of hybrid solar cells</b> .....	8
<b>2.3. Semiconducting conjugated polymers</b> .....	10
<b>2.4. Grafting conjugated polymers onto semiconductor inorganic nanocrystals</b> .....	16
<b>2.5. Routes to improved device performance</b> .....	25
<b>2.6. Summary and outlook</b> .....	34
<b>3. Semiconducting conjugated polymer grafted CdSe nanorod nanocomposites</b> .....	38
<b>3.1. Introduction</b> .....	38
<b>3.2. Experimental</b> .....	40
<b>3.3. Results and discussion</b> .....	45
<b>3.4. Conclusion</b> .....	64
<b>4. Semiconducting conjugated polymer grafted CdTe tetrapods nanocomposites</b> .....	66
<b>4.1. Introduction</b> .....	66

<b>4.2. Experimental</b> .....	67
<b>4.3. Results and discussion</b> .....	70
<b>4.4. Conclusions</b> .....	79
<b>5. Semiconducting conjugated polymer grafted CdSe tetrapod nanocomposites</b> .....	81
<b>5.1. Introduction</b> .....	81
<b>5.2. Experimental</b> .....	82
<b>5.3. Results and Discussion</b> .....	87
<b>5.4. Conclusion</b> .....	106
<b>6. Stokes' shift engineered CdSe/ZnS core/shell QDs for solar concentrators</b> .....	107
<b>6.1. Introduction</b> .....	107
<b>6.2. Experimental</b> .....	110
<b>6.3. Results and discussion</b> .....	112
<b>6.4. Conclusion</b> .....	122
<b>7. Conclusions and future work</b> .....	123
<b>7.1. Conclusions</b> .....	123
<b>7.2. Future work</b> .....	126
<b>References</b> .....	128
<b>VITA</b> .....	139

## LIST OF SCHEMES AND TABLES

<b>Table 2.1.</b> Performance of selected organic-inorganic hybrid solar cells. ....	24
<b>Table 6.1.</b> Optical properties of CdSe/ZnS QDs and CdSe/Cd <sub>1-x</sub> Zn <sub>x</sub> Se <sub>1-y</sub> S <sub>y</sub> /ZnS QDs ..	115
<b>Scheme 3.1.</b> Grafting ethynyl-terminated P3HT (i.e., P3HT-≡) onto (a) N <sub>3</sub> -BPA-functionalized CdSe NRs, and (b) N <sub>3</sub> CH <sub>2</sub> -BA-functionalized CdSe NRs by catalyst-free click chemistry, yielding P3HT-CdSe NR nanocomposites. ....	46
<b>Scheme 4.1.</b> Grafting ethynyl-terminated P3HT (i.e., P3HT-≡) onto azide-functionalized CdTe (i.e., CdTe-N <sub>3</sub> ) tetrapods by catalyst-free click chemistry, yielding P3HT-CdTe tetrapod nanocomposites.....	75
<b>Scheme 5.1.</b> Grafting ethynyl-terminated P3HT onto azide-functionalized CdSe tetrapods with inorganic treatment via catalyst-free click chemistry, yielding P3HT-CdSe tetrapod nanocomposites.....	92
<b>Scheme 6.1.</b> Energy alignment of (a) CdSe/ZnS QDs, and (b) CdSe/Cd <sub>1-x</sub> Zn <sub>x</sub> Se <sub>1-y</sub> S <sub>y</sub> /ZnS QDs.....	112

## LIST OF FIGURES

- Figure 2.1.** Schematic of the general working principle of polymer solar cells. ....10
- Figure 2.2.** Enhanced performance of polymer/colloidal NC hybrid solar cells after treated by ethanedithiol (EDT). (a) Device structure of polymer/CdSe NC hybrid solar cells. (b) TEM image of CdSe nanorods with a scale bar of 20 nm, and molecular structures of P3HT, PCPDTBT, and EDT. (c) Current density-voltage ( $J$ - $V$ ) curves of P3HT/CdSe hybrid solar cells treated with and without EDT. (d)  $J$ - $V$  curves of PCPDTBT/CdSe hybrid solar cells treated with and without EDT. [Reprinted with permission from ref. 58, Copyright @ 2013 American Chemical Society.].....13
- Figure 2.3.** (a) The molecular structure of ligands. (b) Proposed energy level diagram of the oligothiophene-CdSe complexes. [Reprinted with permission from ref. 92, Copyright @ 2003 Wiley-VCH.] .....18
- Figure 2.4.** Schematic illustration of “graft-onto” technique for CP-NC nanocomposites. [Reprinted with permission from ref. 89, Copyright @ 2007 American Chemical Society.] .....19
- Figure 2.5.** Illustration of grafting vinyl-terminated P3HT onto CdSe QDs utilizing bifunctional ligands (DOPO-Br). [Reprinted with permission from ref. 13, Copyright @ 2007 American Chemical Society.].....20
- Figure 2.6.** TEM images of CdS NRs within the P3HT matrix at the cadmium acetate

concentration of (a) 2.5, (b) 8.3, and (c) 12.45 mg/mL. (d) Close-up TEM image of CdSe NR. (e) FTIR spectra of P3HT, P3HT with cadmium acetate, and CdS/P3HT nanocomposites. (f, g, and h) Proposed synthesis mechanism of CdS/P3HT nanocomposites. [Reprinted with permission from ref. 34, Copyright @ 2009 American Chemical Society.] .....22

**Figure 3.1.** TEM images of (a) Br-BPA-functionalized CdSe NRs, (b) close-up of individual Br-BPA-functionalized CdSe NRs, and (c) P3HT-CdSe NR nanocomposites in P3HT matrix.....47

**Figure 3.2.** FTIR spectra of Br-BPA-functionalized CdSe NRs (black), N<sub>3</sub>-BPA-functionalized CdSe NRs (red), and P3HT-CdSe NR nanocomposites (blue). .....48

**Figure 3.3.** (a) *J*~*V* curve of photovoltaic device obtained at 1.5 AM illumination (the device configuration is shown in the inset). (b) TEM image of P3HT-CdSe NR nanocomposite film.....50

**Figure 3.4.** TEM images of CdSe NCs with different ligands with BrCH<sub>2</sub>-BA. (a) SA : BrCH<sub>2</sub>-BA = 3:1, (b) HPA : BrCH<sub>2</sub>-BA = 3:1, (c) TDPA : BrCH<sub>2</sub>-BA = 3:1, and (d) ODPA : BrCH<sub>2</sub>-BA = 3:1. ....52

**Figure 3.5.** Low-magnification TEM images of CdSe NCs at different molar ratio of BrCH<sub>2</sub>-BA to TDPA. (a) BrCH<sub>2</sub>-BA:TDPA=1:0, (b) BrCH<sub>2</sub>-BA:TDPA=1:3, (c) BrCH<sub>2</sub>-BA:TDPA=3:1, and (d) BrCH<sub>2</sub>-BA:TDPA=0:1.....54

**Figure 3.6.** <sup>1</sup>H NMR spectra of (a) BrCH<sub>2</sub>-BA and N<sub>3</sub>CH<sub>2</sub>-BA, (b) the close-up at 4.7 ppm, and (c) the close-up at 7.5 ppm.....55

<b>Figure 3.7.</b> $^1\text{H}$ NMR spectra of (a) ethynyl-terminated P3HT, and (b) P3HT-CdSe NR nanocomposites.....	55
<b>Figure 3.8.</b> FTIR spectra of BrCH <sub>2</sub> -BA-functionalized CdSe NRs (black), N <sub>3</sub> -CH <sub>2</sub> -BA-functionalized CdSe NRs (red), and P3HT-CdSe NR nanocomposites (blue). .....	56
<b>Figure 3.9.</b> (a) The absorption spectra of ethynyl-terminated P3HT (black), BBPA-functionalized CdSe NRs (red), and P3HT-CdSe NR nanocomposites (blue) prepared by click chemistry. (b) Emission spectra of ethynyl-terminated P3HT (black) and P3HT-CdTe NR nanocomposites (red). .....	57
<b>Figure 3.10.</b> Current-voltage characteristics of the hybrid solar cell devices fabricated with P3HT-CdSe NR nanocomposites at different weight ratios.....	59
<b>Figure 3.11.</b> Current-voltage measurement of the hybrid solar cell devices fabricated with P3HT/CdSe NR physical mixture and P3HT-CdSe NR nanocomposites. Thermal annealing condition was controlled (i.e., 130 °C/10min, 130 °C/15min, and 130 °C/20min).....	61
<b>Figure 3.12.</b> AFM measurement on P3HT-CdSe NR nanocomposite films. (a,c) Tapping mode AFM height image and its corresponding phase image of P3HT-CdSe NR hybrid film without methanol treatment. (c,d) Tapping mode AFM height image and its corresponding phase image of P3HT-CdSe NR hybrid film after methanol treatment. z-scale is 100 nm.....	62
<b>Figure 3.13.</b> Current-voltage curves of the P3HT-CdSe NR hybrid solar cells with and without immersion of as-prepared P3HT-CdSe NR films in methanol. ....	63

**Figure 4.1.** Low-magnification TEM images of CdTe NCs at different molar ratio of BBPA to ODPA. (a) BBPA : ODPA = 1:7, (b) BBPA : ODPA = 1:5, and (c) BBPA : ODPA = 1:4 by single injection of Te TOP solution, and (d) BBPA : ODPA = 1:4 by multiple injections of Te TOP solution.....72

**Figure 4.2.** TEM images of (a) BBPA-functionalized CdTe tetrapods; (b) close-up of individual BBPA-functionalized CdTe tetrapod, the close-up of arm marked with a dashed circle is shown as inset; and (c & d) P3HT–CdTe tetrapod nanocomposites.....73

**Figure 4.3.** FTIR spectra of BBPA-functionalized CdTe tetrapods (black), azide-functionalized CdTe tetrapods (i.e., CdTe–N<sub>3</sub> tetrapods; red), and P3HT–CdTe tetrapod nanocomposites (blue). .....75

**Figure 4.4.** <sup>1</sup>H NMR spectra of (a) ethynyl-terminated P3HT (i.e., P3HT–≡), and (b) P3HT–CdTe tetrapod nanocomposites. The peak between 3.5 and 4 ppm in (b) was assigned to the proton of –CH<sub>2</sub> from CdTe–BPA–N<sub>3</sub> tetrapods after grafting of CdTe–BPA–N<sub>3</sub> tetrapods (i.e., CdTe–N<sub>3</sub> tetrapods) onto P3HT–≡.....76

**Figure 4.5.** Thermogravimetry analysis (TGA) of (a) BBPA-functionalized CdTe tetrapods, (b) ethynyl-terminated P3HT homopolymer, and (c) P3HT–CdTe tetrapod nanocomposites prepared by click reaction. ....77

**Figure 4.6.** (a) Absorption spectra of ethynyl-terminated P3HT (black square), BBPA-functionalized CdTe tetrapods (red circle), and P3HT–CdTe tetrapod nanocomposites (blue triangle) prepared by click chemistry. (b) Emission spectra of ethynyl-terminated P3HT (black square) and P3HT–CdTe tetrapod nanocomposites (red circle).....78

<b>Figure 5.1.</b> TEM images of (a) oleic acid-capped zinc blende CdSe QD seeds, (b) close-up of zincblende CdSe QDs, (c, d) CdSe tetrapods grown from CdSe zincblende seeds.....	90
<b>Figure 5.2.</b> TEM images of (a) oleic acid-capped zinc blende CdSe QD seeds, (b) close-up of zinc blende CdSe QDs, (c, d) CdSe tetrapods grown from CdSe zinc blende seeds.	91
<b>Figure 5.3.</b> TEM images of CdSe tetrapods prepared with the seed concentration of (a) 50 $\mu$ mol/L, (b) 25 $\mu$ mol/L, and (c) 5 $\mu$ mol/L.....	91
<b>Figure 5.4.</b> FTIR spectra of as-prepared OA-capped CdSe tetrapods (blue), CdSe tetrapods treated with HBF <sub>4</sub> (black), and N <sub>3</sub> -BA functionalized CdSe tetrapods after capping with 4-azidobenzoic acid (red), and 5-bromovaleric acid capped CdSe tetrapods (brown).....	94
<b>Figure 5.5.</b> XPS spectra for O <sub>1s</sub> binding energies for 4-azidobenzoic acid (N <sub>3</sub> -BA, black square), N <sub>3</sub> -BA-capped CdSe tetrapods (red circle), and OA-capped CdSe tetrapods (blue triangle).....	95
<b>Figure 5.6.</b> FTIR spectra of HBF <sub>4</sub> treated CdSe tetrapods (black), N <sub>3</sub> -BA functionalized CdSe tetrapods after capping with 4-azidobenzoic acid (red), and P3HT grafted CdSe tetrapods (blue). .....	97
<b>Figure 5.7.</b> <sup>1</sup> H NMR spectra of (a) ethynyl-terminated P3HT and P3HT-CdSe tetrapod nanocomposites prepared by grafting P3HT with (b) N <sub>3</sub> -BA-CdSe tetrapods, and (c) N <sub>3</sub> -val-CdSe tetrapods. The inset is the close-up of spectra at around 3.5 ppm. ....	97

**Figure 5.8.** (a) Absorption spectra of ethynyl-terminated P3HT (black), N<sub>3</sub>-BA-functionalized CdSe tetrapods (red), and P3HT-CdSe tetrapod nanocomposites (blue) prepared via click coupling. (b) UV-vis spectra of P3HT/CdSe tetrapod mixture (blue) and P3HT-CdSe tetrapod nanocomposites (red). (c) Photoluminescence spectra of ethynyl-terminated P3HT (black), physical mixture of P3HT/CdSe tetrapod (red), and P3HT-CdSe tetrapod nanocomposites (blue).....98

**Figure 5.9.** Current-voltage characteristics of hybrid P3HT-CdSe tetrapod solar cells with different solvent ratio of chlorobenzene and chloroform. P3HT-CdSe tetrapods samples were prepared via a click reaction between P3HT and N<sub>3</sub>-vul functionalized CdSe tetrapods.....100

**Figure 5.10.** Current-voltage characteristics of hybrid solar cell devices fabricated with P3HT-CdSe tetrapod nanocomposites by employing (a) 5-bromovaleric acid and (b) 4-azidobenzoic acid. (c) Summary of device performance. The effect of CdSe tetrapod size on the PCE was also investigated. ....102

**Figure 5.11.** TEM images of films prepared by (a,b) P3HT-CdSe tetrapod nanocomposites with the size of CdSe tetrapod of 94 nm and its weight fraction of 50%, (c,d) P3HT-CdSe tetrapod nanocomposites with the size of CdSe tetrapod of 94 nm and its weight fraction of 80%, and (e,f) P3HT-CdSe tetrapod nanocomposites the size of CdSe tetrapod of 65 nm and its weight fraction of 50%.....104

**Figure 5.12.** Morphologies of P3HT-CdSe tetrapod nanocomposites film. (a,d) Tapping mode AFM topographies and their corresponding phase images, (b,e) Close-up of CdSe tetrapods showing aggregated region, and (c,f) Close-up showing large domain area. Z-

scale is 100 nm and 50 nm for (a) and (b,c), respectively. ....105

**Figure 6.1.** The absorption and emission spectra of (a) CdSe/ZnS QDs and (b) CdSe/Cd<sub>1-x</sub>Zn<sub>x</sub>Se<sub>1-y</sub>S<sub>y</sub>/ZnS QDs. .... 115

**Figure 6.2.** TEM images of (a) CdSe core QDs, (b) CdSe/Cd<sub>1-x</sub>Zn<sub>x</sub>Se<sub>1-y</sub>S<sub>y</sub> QDs, (c) CdSe/Cd<sub>1-x</sub>Zn<sub>x</sub>Se<sub>1-y</sub>S<sub>y</sub>/ZnS QDs (reacted for 30 min), and (d) CdSe/Cd<sub>1-x</sub>Zn<sub>x</sub>Se<sub>1-y</sub>S<sub>y</sub>/ZnS QDs (reacted for 90 min) ..... 116

**Figure 6.3.** Normalized photoluminescence of conventional CdSe/ZnS QDs prepared by air-sensitive chemical (black) and stable chemicals (blue), and CdSe/Cd<sub>1-x</sub>Zn<sub>x</sub>Se<sub>1-y</sub>S<sub>y</sub>/ZnS QDs with chemical composition gradient prepared with stable chemicals (red), upon exposure to UV irradiation in air. .... 118

**Figure 6.4.** (a) Photoluminescence spectra of CdSe/Cd<sub>1-x</sub>Zn<sub>x</sub>Se<sub>1-y</sub>S<sub>y</sub>/ZnS QDs prepared at 300°C. (b) TEM image of CdSe/Cd<sub>1-x</sub>Zn<sub>x</sub>Se<sub>1-y</sub>S<sub>y</sub>/ZnS QDs after reaction at 300 °C for 90 min (Inset is HR TEM image, scale bar is 10 nm)..... 119

**Figure 6.5.** Absorption and photoluminescence spectra of as-prepared green-, yellow-, and red- emitting CdSe/Cd<sub>1-x</sub>Zn<sub>x</sub>Se<sub>1-y</sub>S<sub>y</sub>/ZnS QDs. ....121

**Figure 6.6.** High-resolution TEM images of (a) green-, (b) yellow-, and (c) red-emitting CdSe/Cd<sub>1-x</sub>Zn<sub>x</sub>Se<sub>1-y</sub>S<sub>y</sub>/ZnS QDs. Inset are the magnified images; Scale bar = 10 nm. ...121

## SUMMARY

Despite great development of semiconductor technology, it cannot fulfill the demands for easy and low-cost manufacturing of optoelectronic devices. In this context, much effort has been devoted to fabricating solution- processable optoelectronic devices by utilizing colloidal nanocrystals (NCs), particularly in the field of solar cells. However, the applications of NCs in optoelectronic devices, including solar cells, light-emitting diodes (LEDs), and lasers have not yet been fully discovered,<sup>1</sup> in spite of recent advances in the synthesis of semiconducting nanocrystals (NCs). Meanwhile, conjugated polymers (CPs) have drawn considerable attention as promising materials in the field of solar cells, LEDs, thin film transistors, and biosensors.<sup>2</sup> Their advantageous properties such as lightweight, flexibility, low-cost, and large area producibility may open up opportunities for accessing a large variety of optoelectronic devices at low cost, especially when combined with semiconducting NCs. Nonetheless, integrating organic and inorganic semiconductors and applying them in optoelectronic devices have been sluggish regardless of time and effort devoted. To this end, the ability to enhance intrinsic properties of NCs through the design of novel nanostructured NCs as well as to craft semiconducting CP-NC nanocomposites with intriguing optical and electronic properties will allow us to meet these demands noted above.<sup>3</sup>

This thesis aims to not only fully explore optoelectronic properties of NCs but, also craft novel semiconducting CP-grafted NC nanocomposites, which exhibit enhanced optical and electronic properties as well as solution processable characteristic. In all studies, cadmium selenide (CdSe) and cadmium telluride (CdTe) were employed and

demonstrated as inorganic semiconducting components due to the following reasons. CdSe possesses much higher charge carrier mobility as compared to CPs and fullerene derivatives. In addition, the optoelectronic properties of CdSe (e.g., band gap;  $E_g = 1.72$  eV) can be easily tuned simply by controlling their size owing to the quantum confinement effect. Similarly, CdTe is an appealing inorganic semiconductor for inorganic solar cells due to its optimum band gap energy ( $E_g = 1.45$  eV) and high absorption coefficient ( $\alpha = 10^4$  cm<sup>-1</sup>),<sup>4</sup> thereby improving the light harvesting efficiency by extending into the near-infrared (NIR) range. Clearly, incorporating these inorganic semiconductor nanocrystals in CPs may result in intriguing optoelectronic properties. For the sake of easy demonstration for optoelectronic devices, P3HT was adopted as organic component for preparing all organic-inorganic nanocomposites investigated in this thesis as it is one of most widely studied CPs and serves as electron donor in photovoltaic applications.

In this thesis, the optical and electronic properties of semiconducting NCs were first optimized by controlling their size, architecture, and composition. The simple strategy to achieve graded shell architecture for highly luminescent, photostable, and Stokes' shift engineered semiconducting QDs was also explored. This thesis also presented the robust routes to crafting CP-NC nanocomposites via click coupling between two semiconducting constituents by the utilization of bifunctional short ligands. First, in order to produce NCs with desirable architecture such as quantum dots, nanorods, and tetrapods, the effects of the monomer concentration, the amount of short bifunctional ligands, and the type of surfactants on the shape of NCs were studied. In addition, solar cells were fabricated using these CP-NC nanocomposites by spin-casting. The influence

of the shape and size of NCs, the types of ligands, and the weight ratio of CPs to NCs on the device performance was explored. Crafting CP-grafted NCs and their utilization in optoelectronic devices also provided insights into the use in photovoltaics as well as a variety of other applications.

# **1. Introduction**

## **1.1. Motivation**

As the global energy demand grows, the need for more efficient and economic energy sources has become greater than ever. Fossil fuels, however, are running out and responsible for the increased concentration of carbon dioxide in the Earth's atmosphere. Therefore, it has become great challenge to develop environmentally friendly renewable energy sources in modern society. Photovoltaic (PV), the technology that directly converts light into electricity, is one of the possible solutions for energy crisis. Until now, the materials used as active layer in solar cells are mainly inorganic semiconductor materials, such as silicon, gallium-arsenide, cadmium-telluride, and cadmium-indium-selenide. The power conversion efficiency of these solar cells ranges from 10% to 30 %. However, these solar cells hardly contribute to the energy market due to their high cost and difficulty in mass production. In particular, the cost in large-scale production is one of the major obstacles. In this context, the need to develop and deploy large-scale, cost effective, and flexible renewable energy is becoming increasingly important.

Recent research on conjugated polymers (CPs) have garnered increasing attention as they offer potential applications in biosensors, thin film transistors, LEDs, and solar cells.<sup>4-5</sup> In the latter context, the use of CPs may pave a promising way to achieve easily manufactured, low-cost solar cells by capitalizing on the advantageous attributes of CPs, such as lightweight, flexibility, roll-to-roll production, low cost, and

large area.<sup>5c, 6</sup> However, the incorporation of electron accepting materials which favor the transport of electrons in hybrid solar cells is required as the hole mobility in CPs far exceeds the electron mobility. In this context, Hybrid solar cells composed of CPs and semiconductor NCs have been considered as a promising alternative to inorganic solar cells due to the complementary advantages of CPs and NCs as noted above.<sup>7</sup> It is worth noting that most of CP/NC composites are prepared by simple physical mixing of these two constituents based on ligand exchange by utilizing co-solvent or binary solvent mixture.<sup>7a, 8</sup> However, this approach has several issues such as the existence of insulating surface ligand and microscopic phase separation, thus limiting the performance of the resulting photovoltaic devices due to the decreased light collection through scattering and the reduced interfacial area and charge transfer between CPs and NCs as well as the electron transport between adjacent NCs in physically mixed composites.<sup>9</sup> In this context, the ability to chemically tether CPs onto the NC surface (i.e., forming intimate CP–NC nanocomposites) can provide an elegant means of achieving a uniform dispersion of NCs, and, more importantly, promoting the electronic interaction between these two semiconductors

In this context, a robust synthetic strategy to chemically tether CPs onto the NC surface (i.e., forming intimate CP–NC nanocomposites) is highly desirable in order to achieve a uniform dispersion of NCs, and, more importantly, promoting the electronic interaction between these two semiconductors.

## **1.2. Challenging**

Several challenging issues have found to hinder the full exploiting of

nanomaterials in hybrid solar cells. First of all, while surfactants are necessary to control the shape and size of colloidal NCs as well as to disperse NCs in desired solvent for solution-processability, they are usually insulating, and thus hinder the electronic interaction between CPs and NCs or NCs and NCs. Therefore, “ligand exchange” process,<sup>10</sup> which replaces original capping ligands with desired ones through the adsorption-desorption dynamics, is required to address this issue. In general, short ligands are introduced onto the NC surface during ligand exchange process to minimize insulating effects from ligands, thus improving electronic interaction among them. However, this in turn weakens steric hindrance, and thus results in the agglomeration of NCs. Clearly, electronic interaction and dispersion of NCs are inversely correlated when the conventional ligand exchange approach is utilized. Moreover, the ligand exchange process is generally tedious and thus detrimental for easy and low-cost manufacturing of solar cells. Furthermore, the poor miscibility of CPs with NCs is another issue. Despite the ligand exchange of NCs, the agglomeration of NCs in the CP matrix is usually observed. Once it occurs, the surface area between electron donating CPs and electron accepting NCs decreases, leading to reduced exciton dissociation, diffusion, and carrier transport.

In this context, crafting CP-grafted NCs with intimate contact between them may provide new opportunities for various optoelectronic applications as these nanocomposites are expected to address issues noted above, thus maximizing the advantages of organic-inorganic hybrid nanomaterials.

### 1.3. Research objectives

The goal of this project is to introduce simple yet robust strategy for colloidal NCs synthesis with improved optoelectronic properties as well as to craft semiconductor organic-inorganic nanocomposite materials composed of CPs that are in intimate contact with inorganic NCs as acceptors. These newly prepared CP-NC nanocomposites may offer promising opportunities to develop novel hybrid materials with improved electronic interaction. The specific objectives of this thesis are listed as follows.

- To explore novel synthetic routes to colloidal NCs with intriguing optical and electronic properties, including Stokes' shift engineering and emission peak tuning via tailoring the architecture and composition of NCs.
- To investigate the effects of the precursor concentration, the amount of bifunctional ligands, and the ratio of bifunctional ligands to aliphatic ligands on the shape of NCs.
- To rationally design semiconducting organic-inorganic nanocomposites to achieve close contact between the electron donor (i.e., CPs) and the electron acceptor (i.e., CdSe NCs, CdTe NCs) to promote charge dissociation at the donor/acceptor interface.
- To reveal the effect of the intimate contact in semiconducting organic-inorganic nanocomposites achieved through chemical coupling on the efficiency of the resulting solar cells.
- To correlate the shape and size of electron accepting NCs, the types of

bifunctional ligands, and the amount of residue aliphatic insulating ligands with the device performance.

#### **1.4. Map of dissertation**

This thesis reports robust synthetic routes for inorganic-organic nanocomposites for a large variety of potential applications, particularly photovoltaic. In Chapter 2, the current progress in organic-organic nanocomposites preparation and their applications in photovoltaics are reviewed. Chapter 3 discusses the methodology to achieve elongated architecture of CdSe NCs with bifunctional capping ligands and the route to P3HT-CdSe NR nanocomposites. Moreover, photovoltaic devices fabricated utilizing P3HT-CdSe NR nanocomposites were studied. Chapter 4 investigates the effect of bifunctional ligands on the CdTe NC shape and the strategy for crafting P3HT-CdTe tetrapod nanocomposites. CdSe tetrapods with high selectivity were prepared and coupled with P3HT by the aid of bifunctional ligands and the photovoltaic devices based on P3HT-CdSe tetrapod nanocomposites were constructed in Chapter 5. Chapter 6 studies chemical composition gradient CdSe/Cd<sub>1-x</sub>Zn<sub>x</sub>Se<sub>1-y</sub>S<sub>y</sub>/ZnS QDs with improved optical properties. Chapter 7 summarized the key findings in each chapter and provides the outlook for future research.

## **2. Organic-inorganic nanocomposites composed of conjugated polymers and semiconductor nanocrystals for photovoltaics**

Jaehan Jung, Young Jun Yoon, Ming He, and Zhiqun Lin, “*Organic-Inorganic Nanocomposites Composed of Conjugated Polymers and Semiconductor Nanocrystals for Photovoltaics*”, *Journal of Polymer Science Part B: Polymer Physics*, 2014, 52, 1641, Copyright 2014 WILEY-VCH Verlag GmbH & Co.

### **2.1. Introduction**

Polymer solar cells have received considerable attention over the past several decades due to their advantageous properties, including lightweight, flexibility, and solution processability.<sup>11</sup> However, the electron mobility of most of conjugated polymers (CPs) is a few orders of magnitude lower than their hole mobility, thereby resulting in the charge carrier recombination in photoactive layer. In this regard, incorporating electron acceptors such as fullerene derivatives or semiconductor inorganic nanocrystals (NCs) is of key importance.<sup>12</sup> The bulk-heterojunction (BHJ) structure has been recognized as the most successful architecture for polymer solar cells.<sup>13</sup> In a typical BHJ solar cell, the phase separation of donor and acceptor materials forms nanoscopic donor and acceptor domains with the size comparable to the diffusion length of CPs (approximately 10~20 nm), thus maximizing the possibility of photogenerated excitons within CP phase to diffuse to the donor/acceptor interface and dissociate.<sup>14</sup> In the meanwhile, a bicontinuous structure is favorable in BHJ devices because of much promoted charge carrier transport toward respective electrodes.<sup>15</sup> Recently, BHJ solar cells composed of CPs and fullerene

have achieved energy conversion efficiency up to 6~8%.<sup>16</sup>

Inorganic nanocrystals (NCs) possess size-dependent optical and electronic properties that open up opportunities for use in solar cells,<sup>3-4, 5b, 17</sup> LEDs,<sup>18</sup> tunable lasers,<sup>19</sup> bio-sensors,<sup>20</sup> and bio-imaging applications.<sup>21</sup> In particular, incorporating NCs (e.g., CdS, CdSe, CdTe, PbS, ZnO, etc.) in polymer solar cells would facilitate the charge dissociation and transport owing to the large surface area, high electron affinity, and excellent intrinsic carrier mobility of NCs.<sup>4, 22</sup> In this context, semiconductor NCs have been introduced as electron acceptors into hybrid solar cells (e.g., poly(3-hexylthiophene)/CdSe NCs; P3HT/CdSe).<sup>40,41</sup> However, simply physically mixing CP and NC often results in micro-scale phase segregation, thus limiting the resulting device performance.<sup>7a</sup> In addition, the insulating organic ligands capped on the NC surface hinder the electronic interaction with CPs. As a result, the ability to directly tether CPs on the NC surface would be an elegant means of achieving the intimate contact between CPs and NCs to prevent such microscopic aggregation. To this end, direct grafting and *in-situ* growth methods have been explored to create CP-grafted NCs and naked NCs in the CP matrix, respectively, for hybrid solar cells.<sup>12, 23</sup>

Polymer solar cells often suffer from insufficient light absorption despite the strong absorption coefficient of most CPs. This is because the thickness of photoactive layer is restricted due to the short charge carrier diffusion length as well as the use of large bandgap of CPs which fails to absorb solar photons in near infrared (NIR) region. In this regard, plasmonic metallic NCs (e.g., Au and Ag) and NIR-absorbing NCs (e.g., PbS and PbSe) have been utilized to further harvest solar energy.<sup>24</sup> Moreover, despite the

significant developments in interfacial treatment for efficient charge separation, control over the architecture of photoactive layer comprising CP/NC nanocomposites has not yet been exploited to its full potential for charge transport due largely to the difficulty in controlling the film morphology during the spin-casting process. Ideal device geometry should consist of bicontinuous pathway for both holes and electrons, and thus enhance charge transport as well as reduce the charge recombination.

This chapter seeks to summarize the recent progress in organic-inorganic hybrid solar cells. The working principle of hybrid solar cells and the development of semiconducting p-type and n-type CPs are introduced. The advances in the synthesis of CP-NC nanocomposites in which CP and NC are in intimate contact for hybrid solar cells are highlighted. Several approaches, including the light harvesting enhancement and the control over photoactive layer architectures, to potentially further increase power conversion efficiency of hybrid solar cells are discussed. An outlook for future research directions in this rich field is also provided.

## **2.2. Working principle of hybrid solar cells**

The general working principle of hybrid solar cells includes the following consecutive steps: (1) the absorption of photons and generation of electron-hole pairs (i.e., excitons) in donor materials, (2) the diffusion of excitons to the donor/acceptor interface, (3) the dissociation of excitons and charge carriers separation, and (4) the transport of holes and electrons to respective electrodes (**Figure 2.1**). The photon absorption is determined by the optical properties of electron donating materials as well as internal

reflection and the thickness of photoactive layer. However, electron donating semiconducting CPs (e.g., P3HT and poly[2-methoxy-5-(3',7'-dimethyloctyloxy)-1,4-phenylenevinylene] (MDMO-PPV)) often exhibit a bandgap larger than  $\sim 2$  eV, hence the light absorption at longer wavelengths above  $\sim 700$  nm is limited. Moreover, the thickness of photoactive layer cannot go beyond a certain value because of the limited charge carrier diffusion length, thereby leading to the restricted absorption of solar energy. Once photons are absorbed in an organic semiconductor, a spatially localized electron-hole pair (i.e., a Frenkel type exciton) is formed.<sup>25</sup> Typically, generated excitons in polymer solar cells are strongly bounded due to high dielectric constant of CPs. The binding energy of excitons in the most of CPs lies in the range of 0.1~0.5 eV. As excitons are electrically neutral, their migration direction is random. The range of movement can be defined by diffusion length ( $L = (D \cdot \tau)^{1/2} = \sim 10$  nm, where  $\tau$  is the exciton lifetime and  $D$  is the diffusion coefficient).<sup>26</sup> The dissociation of excitons occurs solely at the donor/acceptor interface, indicating that excitons need to migrate to the donor/acceptor interface to generate charge carriers. Because of short diffusion length, it requires nanoscale phase separation of donors and acceptors in order to maximize interfacial area for exciton dissociation. It is worth noting that the exciton dissociation can also be facilitated by the donor-acceptor lowest unoccupied molecular orbital (LUMO) energy level offset as well as internal electric field. Once free electrons and holes are generated from the exciton dissociation, they must efficiently transport to the respective electrodes without recombination. In order to achieve excellent charge carrier transport, bicontinuous percolating network structure of donors and acceptors is highly desired.

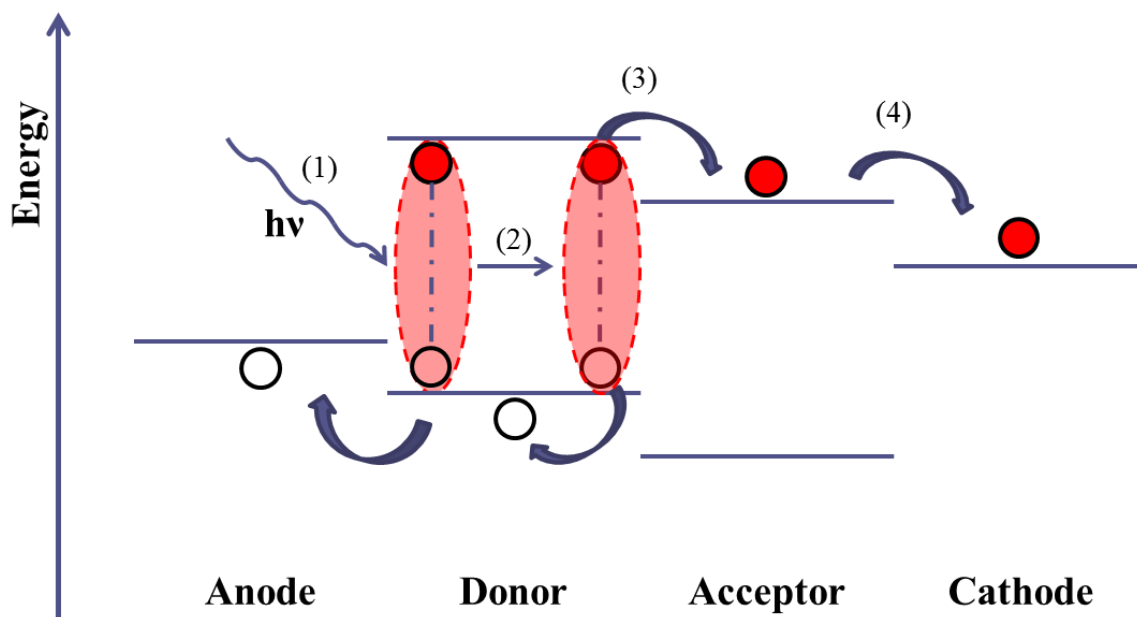


**Figure 2.1.** Schematic of the general working principle of polymer solar cells.

### 2.3. Semiconducting conjugated polymers

Conjugated polymers (CPs) have been widely regarded as promising electron-donor alternatives to their inorganic counterparts for photovoltaics, offering expanded opportunities for fabricating large-area, light-weight, flexible solar cells at low cost.<sup>27</sup> A large variety of CPs such as poly[2-methoxy-5-(3',7'-dimethyloctyloxy)-1,4-phenylenevinylene] (MDMO-PPV),<sup>28</sup> poly(2-methoxy-5-(2'-ethyl)-hexyloxy-p-phenylenevinylene) (MEH-PPV),<sup>29</sup> and poly(3-alkylthiophene)s (P3ATs) have been employed as electron donors in polymer solar cells,<sup>30</sup> in which fullerene derivatives such as [6,6]-phenyl-C<sub>61</sub>-butyric acid methyl ester (PC<sub>61</sub>BM) and/or [6,6]-phenyl-C<sub>71</sub>-butyric acid methyl ester (PC<sub>71</sub>BM) are often used as electron-acceptor materials due to their high electron mobility and ultrafast charge transfer.<sup>2</sup>

Among all CPs, poly(3-hexylthiophene) (P3HT) has been commonly employed as a prototype donor material, possessing a band gap of ~1.9 eV, high optical absorption, and proper energy level alignment with electron-acceptor fullerene materials.<sup>31</sup> On the other hand, like many organic conjugated materials, the dielectric constant of P3HT is rather low (i.e.,  $\epsilon \approx 3\sim 4$ ) as compared with that of inorganic semiconductors. Thus, the photogenerated excitons within P3HT are bounded electron-hole pairs due to the relatively strong Coulombic interaction.<sup>2</sup> Owing to the intrinsically weak electronic interactions among CP chains, the photogenerated excitons usually belong to the Frenkel exciton with a high binding energy in the range of 0.06~0.8 eV.<sup>32</sup> Therefore, the photogenerated excitons need to diffuse to the donor-acceptor interface, wherein the electron of exciton can transfer from the relatively high LUMO level of CP donor to the relatively low LUMO level of acceptor, forming a charge transfer (CT) exciton state as well as releasing extra molecular vibrational energy. If the released extra molecular vibrational energy exceeds the binding energy of the CT exciton, the exciton can eventually be dissociated into free charge carriers (i.e., hole and electron).<sup>32</sup> After dissociation, free holes and electrons need to transport to the anode and cathode, respectively, and are collected. In this context, the energy-level of both donor and acceptor materials should be well-aligned to facilitate the exciton dissociation. The area of donor-acceptor interface also needs to be maximized to promote the charge generation. The film morphology of photoactive layer should be optimized to improve the charge transport.

It is noteworthy that the photovoltaic performance of polymer hybrid solar cells is highly correlated with the energy-level alignment at the donor-acceptor interface,

where a large energy offset between the highest occupied molecular orbital (HOMO) of conjugated-polymer donors and the conduction band (CB) of inorganic NC acceptors is beneficial for achieving high open-circuit voltage ( $V_{oc}$ ). A low bandgap of CP donors, on the other hand, is favorable for extending the optical absorption, increasing the charge carrier, and improving short-circuit current density ( $J_{sc}$ ).<sup>15b</sup> Recently, the use of newly developed ‘push-pull’ alternating low bandgap copolymers has significantly improved the efficiency of polymer solar cells.<sup>27b,33</sup> The incorporation of intramolecular charge transfer (ICT) between the electron-donating (i.e., to push electron) units and the electron-withdrawing (i.e., to pull electron) units renders the low optical bandgaps, tunable HOMO/LUMO levels, and ultimately enhanced optoelectronic efficiency.<sup>27a</sup> In comparison to P3HT/CdSe nanorod (NR) hybrid solar cells, the photovoltaic performance of poly[2,6-(4,4-bis(2-ethyl hexyl)-4H-cyclopenta[2,1-b;3,4-b’]-dithiophene)-alt-4,7-(2,1,3-benzothiadiazole)] (PCPDTBT)-based hybrid solar cells was markedly enhanced, in which  $J_{sc}$  increased from 5.9 mA/cm<sup>2</sup> in P3HT/CdSe hybrid solar cells to 9.3 mA/cm<sup>2</sup> in PCPDTBT/CdSe-based devices (**Figure 2.2**). This can be ascribed to the effective harvesting of infrared photons by low bandgap PCPDTBT copolymer.<sup>34</sup> Moreover, the additional treatment of CdSe NRs with ethanedithiol (EDT) further exchanged the residual ligands on the surface of CdSe NRs, resulting in a high  $J_{sc}$  of 12.8 mA/cm<sup>2</sup> and enhanced power conversion efficiency (PCE) of approximately 4.7% in PCPDTBT/CdSe hybrid solar cells.<sup>34</sup>

All-CP solar cell (i.e., n-type CP/p-type CP device) and specific CP/NC solar cell (i.e., n-type CP/p-type NC/ device) carry several promising advantages over the CP/fullerene device, including tunable photovoltage, high absorption coefficient, and

excellent chemical properties. However, the efficiency of all-CP or such CP/NC hybrid devices has been limited due to the lack of suitable n-type CPs. In this respect, much effort has been made to synthesize n-type CPs, utilizing primarily perylene diimide (PDI) or naphthalene diimide (NDI). Zhou et al. reported PCE of 2.23% by employing PDI-based n-type CPs as acceptors and polythiophene derivatives as donors.<sup>35</sup> Comparing to PDI-based polymers, NDI-based polymers showed improved electron mobility and red-

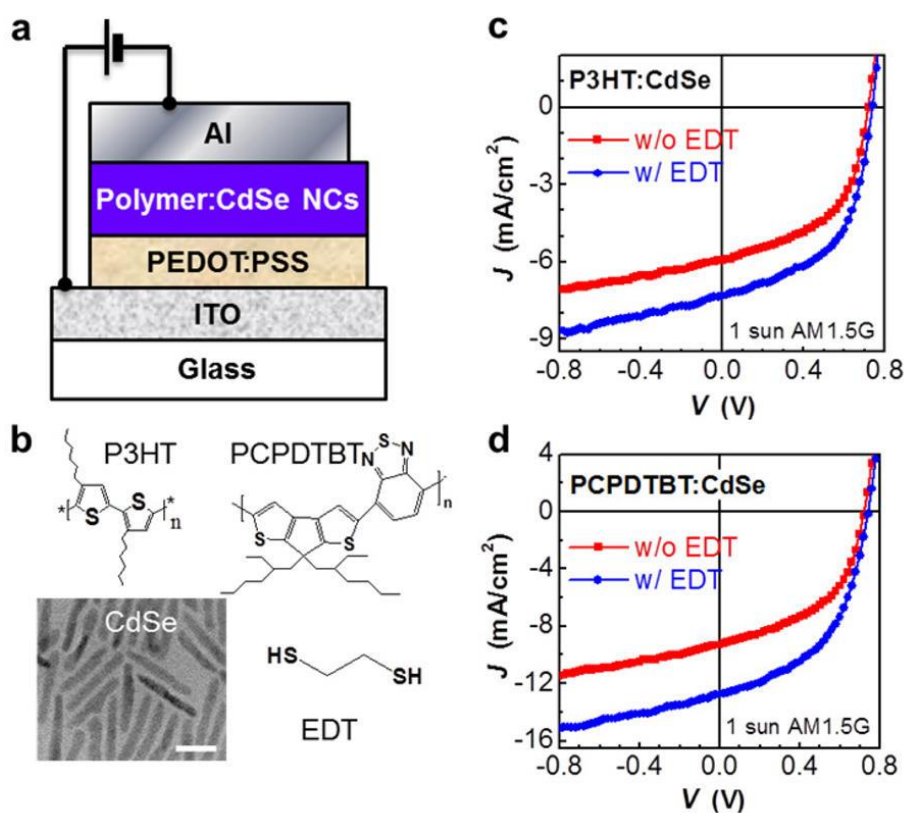


**Figure 2.2.** Enhanced performance of polymer/colloidal NC hybrid solar cells after treated by ethanedithiol (EDT). (a) Device structure of polymer/CdSe NC hybrid solar cells. (b) TEM image of CdSe nanorods with a scale bar of 20 nm, and molecular structures of P3HT, PCPDTBT, and EDT. (c) Current density-voltage ( $J$ - $V$ ) curves of P3HT/CdSe hybrid solar cells treated with and without EDT. (d)  $J$ - $V$  curves of PCPDTBT/CdSe hybrid solar cells treated with and without EDT. [Reprinted with permission from ref. 58, Copyright @ 2013 American Chemical Society.]

shifted absorption. For example, poly([N,N'-bis(2-octyldodecyl)-naphthalene-1,4,5,8-bis(dicarboximide)-2,6-diyl]-alt-5,5'-(2,2'-bithiophene)) P(NDI2OD-T2) exhibited a high electron mobility up to  $0.85 \text{ cm}^2/\text{Vs}$ .<sup>36</sup> Moore et al. fabricated a BHJ all-CP solar cell composed of a P(NDI2OD-T2) acceptor and a P3HT donor.<sup>37</sup> The PCE of ITO/PEDOT/P3HT:P(NDI2OD-T2)/Al devices was 0.21% with a  $V_{oc}$  of 0.52 V, a  $J_{sc}$  of  $1.41 \text{ mA}/\text{cm}^2$ , and a fill factor ( $FF$ ) of 0.29 regardless of high electron mobility and deep LUMO level of P(NDI2OD-T2). This can be attributed to the micro-sized phase separation and the rapid geminate recombination. Earmme et al. reported an all-CP solar cell with a 3.3% PCE utilizing a NDI-based CP as an acceptor and a thiazolothiazolidithienosilole as a donor.<sup>38</sup> A NDI-thiophene copolymer and two NDI-selenophene copolymers were synthesized and mixed with a poly[(4,4'-synthesized 2,2',3'-dithienosilole)-2,6-diyl]-alt-(2,5-bis(3-(2-ethylhexyl)thiophen-2-yl)thiazolo[5,4-d]thiazole)] (PSEHTT) donor in this study. The conjugated electron acceptor isoindigo was also used to prepare a new n-type CP, polyisoindigo with a bandgap of 1.70 eV (HOMO and LUMO levels of -5.54 eV and -3.84 eV, respectively).<sup>39</sup> The device with ITO/PEDOT:PSS/P3HT:polyisoindigo/LiF/Al structure exhibited a PCE of 0.47% ( $J_{sc} = 1.91 \text{ mA}/\text{cm}^2$ ,  $V_{oc} = 0.62 \text{ V}$ , and  $FF = 0.41$ ).

The nature of batch-to-batch variations in CPs such as molecular weight, polydispersity, purity, and solubility may lead to the difference in device performance. It has been demonstrated that the incorporation of small molecules as donors replacing CP donors can circumvent batch-to-batch variations. Walker et al. synthesized a

diketopyrrolopyrrole-based electron donating small molecule, 3,6-bis(5-(benzofuran-2-yl)thiophen-2-yl)-2,5-bis(2-ethylhexyl)pyrrolo[3,4-c]pyrrole-1,4-dione (DPP(TBFu)<sub>2</sub>).<sup>40</sup> These small molecules were mixed with PC<sub>71</sub>BM to yield small molecule-based BHJ solar cells (i.e., ITO/PEDOT:PSS/DPP(TBFu)<sub>2</sub>:PC<sub>71</sub>BM)/Al, exhibiting a PCE of 4.2% with a *J*<sub>sc</sub> of 9.0 mA/cm<sup>2</sup>, a *V*<sub>oc</sub> of 0.94 V, and a *FF* of 0.49. Recently, a novel small molecule donor was synthesized based on the acceptor/donor/acceptor framework with [1,2,5]thiadiazolo[3,4-c]pyridine (PT) units at two ends and dithieno(3,2-b; 2';3'-d)silole (DTS) unit at the center, forming 5,5'-bis{(4-(7-hexylthiophen-2-yl)thiophen-2-yl)-[1,2,5]thiadiazolo[3,4-c]pyridine-3,3'-di-2-ethylhexylsilylene-2,2'-bithiophene (DTS(PTTh<sub>2</sub>)<sub>2</sub>).<sup>41</sup> The DTS unit is more electron rich, thereby leading to strong intramolecular charge transfer. In contrast, PT unit makes DTS(PTTh<sub>2</sub>)<sub>2</sub> a good electron acceptor due to its strong electron affinity. The optical bandgap of DTS(PTTh<sub>2</sub>)<sub>2</sub> was approximately 1.5 eV with the HOMO and LUMO levels of -5.2 eV and -3.6 eV, respectively. These energy levels impart broad absorption of solar spectrum as well as excellent match with the HOMO/LUMO levels of electron accepting PC<sub>70</sub>BM (i.e., -6.1eV/-4.3eV) for photovoltaic applications. The ITO/MoO<sub>x</sub>/DTS(PTTh<sub>2</sub>)<sub>2</sub>:PC<sub>70</sub>BM/Al solar cells were fabricated via spin-casting and exhibited a *J*<sub>sc</sub> of 11.4 mA/cm<sup>2</sup>, a *V*<sub>oc</sub> of 0.80 V, a *FF* of 0.39, and a PCE of 4.5%. After the 1,8-diiodooctane (DIO) treatment, it further increased up to 6.7% with a *J*<sub>sc</sub> of 14.4 mA/cm<sup>2</sup>, a *V*<sub>oc</sub> of 0.78 V, and a *FF* of 0.59%. Interestingly, squaraine dye was also found to act as an electron donor. For example, alkyl- or alkenyl-substituted squaraine were employed in BHJ solar cells with

PC<sub>71</sub>BM.<sup>42</sup> The HOMO and LUMO levels were -3.3 eV and -5.0 eV with an absorption coefficient of  $\sim 2 \times 10^5 \text{ M}^{-1} \text{ cm}^{-1}$ . The resulting squaraine/PC<sub>71</sub>BM BHJ solar cells had PCEs of 1.39 % and 1.99 % for hexyl- and hexenyl-substituted squaraine dyes, respectively.

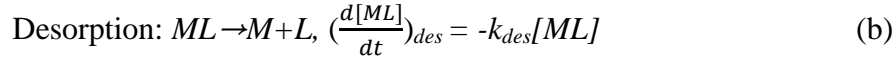
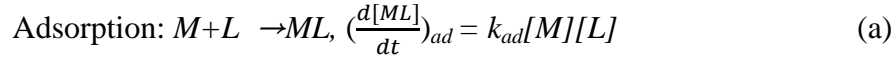
#### **2.4. Grafting conjugated polymers onto semiconductor inorganic nanocrystals**

Most of polymer solar cells have utilized fullerene derivatives as electron acceptors. However, in theory their limited charge carriers mobility promotes many studies in search of other promising materials as electron acceptors such as semiconductor inorganic nanoparticles (e.g., CdS<sup>43</sup>, CdSe,<sup>17c, 22h, 44</sup> CdTe,<sup>45</sup> PbSe,<sup>46</sup> and ZnO<sup>47</sup>). It is interesting to note that these nanoparticles possess high intrinsic carrier mobility and their bandgaps can be precisely tuned by controlling the size of nanoparticles.<sup>48</sup> Moreover, a large interfacial area between donor and acceptor due to the use of nano-sized particles ensures the effective charge separation, thereby reducing the current losses due to charge recombination.<sup>49</sup> Motivated by these advantages, hybrid solar cells utilizing inorganic NCs (i.e., CdSe NRs) as electron donor and poly(3-hexylthiophene) (P3HT) as electron acceptor were fabricated.<sup>7a</sup> The PCE of ITO/PEDOT:PSS/P3HT:CdSe NRs/Al devices was 1.7% with a  $J_{sc}$  of 5.7 mA/cm<sup>2</sup>, a  $V_{oc}$  of 0.7 V, and a  $FF$  of 0.4. However, the overall performance of hybrid devices were not satisfactory as expected when considering the intrinsically high mobility of inorganic materials. This is due possibly to the presence of insulating ligands (i.e., surfactant) in the NC synthesis and the microscale phase segregation of NCs within the CP matrix.<sup>50</sup> The insulating ligands often form a barrier of several angstroms around NCs, thus impeding the electron transport to adjacent NCs or from CPs. Moreover, charge carriers are trapped in the micro-sized domains when their

size is larger than that of the exciton diffusion length. As a result, much effort has been concentrated on the increase of interfacial area between CPs and NCs through the surface modification of NCs as discussed in the following.<sup>23b, 51</sup>

#### 2.4.1. Ligand exchange of original insulating ligand with conjugated oligomers and conjugated polymers

Ligand exchange of original ligands capped on the NC surface with the desired ones through the adsorption-desorption dynamics is commonly used to functionalize NC. The reactions and rates of adsorption-desorption dynamics can be described as follows,<sup>10</sup>



where  $M$  and  $L$  refer to the bonding sites on the surface of NCs and the free-state ligands concentration, respectively.  $[ML]$  is the concentration of ligands in the bonded state.  $k_{ad}$  and  $k_{des}$  are the adsorption and desorption reaction rate constants, respectively. The average surface ligand coverage,  $\theta$  can be described as  $\theta = [ML]/([M] + [L])$ . For a given NC system, the number of bonding sites ( $[M] + [ML]$ ) is constant. The equations (a) and (b) can thus be rewritten in terms of the change in the average surface ligand coverage,  $\frac{d[\theta]}{dt}$ :



It should be noted that  $\theta$  depends on the concentration of ligands,  $k_{ad}$ , and  $k_{des}$ . The latter two are governed by the chemical nature of ligands, which is directly related to the binding ability of functional groups of ligands to NC as well as the steric effects resulting from neighboring ligands capped on the NC surface. The most commonly used ligands include thiols, amines, carboxylic acids, phosphonic acids, and phosphine oxides.<sup>52</sup>

Recently, ligand exchange has been demonstrated to be effective in passivating the NC surface with CP ligands. For example, two conjugated oligomer (CO) ligands, that is, pentathiophene phosphonic acid (T5) and terthiophene phosphonic acid (T3) were tethered onto the surface of CdSe NCs via ligand exchange (**Figure 2.3**).<sup>53</sup> The phosphonic acid moiety at one end served as functional group that allowed strong anchoring of CO to the surface of CdSe NC. The oligohexylthiophene at another end

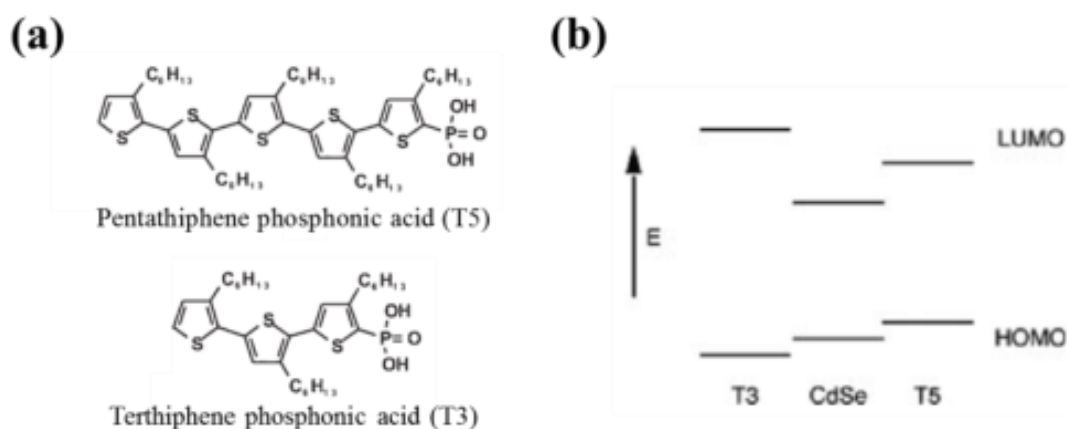


**Figure 2.3.** (a) The molecular structure of ligands. (b) Proposed energy level diagram of the oligothiophene-CdSe complexes. [Reprinted with permission from ref. 92, Copyright © 2003 Wiley-VCH.]

provided good solubility of CdSe NCs in the most of organic solvents, and good miscibility with CPs of similar chemical structures (e.g., P3HT). Querner et al. grafted carbodithioate-oligothiophenes onto the CdSe quantum dot (QD) surface via ligand exchange for solar cells.<sup>52</sup> A staggered (type II) alignment ensured the charge separation.

#### 2.4.2. Direct grafting of conjugated polymers onto nanocrystals.

Despite the simplicity of ligand exchange, the grafting density of CPs on the NC surface is usually low as the targeted CP chains are longer than the originally passivated ligands (i.e., an entropic penalty).<sup>12</sup> To address this issue, Zhang et al. recently applied a two-step approach to graft P3HT onto CdSe NRs by using a bifunctional ligand.<sup>51</sup> First, ligand exchange with rationally designed bifunctional ligands (e.g., arylbromide-functionalized phosphine oxides or thiols) was performed to exchange the original insulating ligands on the NR surface. One end (e.g., phosphine oxide) of bifunctional ligand was tethered to the surface of CdSe NR, while the other end (i.e., arylbromide) underwent the coupling reaction with end-functionalized P3HT. Second, vinyl-terminated

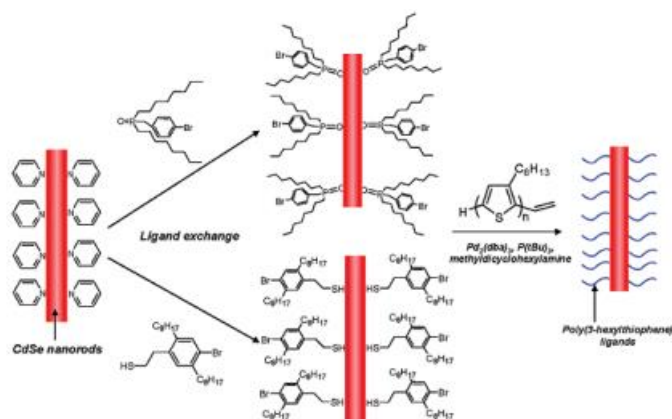


**Figure 2.4.** Schematic illustration of “graft-onto” technique for CP-NC nanocomposites. [Reprinted with permission from ref. 89, Copyright @ 2007 American Chemical Society.]

P3HT was grafted onto the CdSe NR surface through Heck coupling between arylbromide functionalities and vinyl end groups as depicted in **Figure 2.4**. The grafting density was 250 and 400 P3HT chains per CdSe NR for phosphine oxide- and thiol-functionalities, respectively. This result correlated well with the fact that thiol ligands coordinate more effectively than phosphine oxide ligands.

Xu et al. introduced a simpler way for grafting CPs on NCs and thus eliminated the need for ligand exchange process.<sup>3</sup> In their work, [(4-bromophenyl)methyl]dioctylphosphine oxide (DOPO-Br) capped CdSe QDs were first prepared. The vinyl-terminated P3HT was then directly grafted onto the CdSe QD surface via Pd-catalyzed Heck coupling in the absence of ligand exchange (**Figure 2.5**).<sup>3</sup> However, the weak binding strength of phosphine oxide with NCs may be a limitation of this approach.

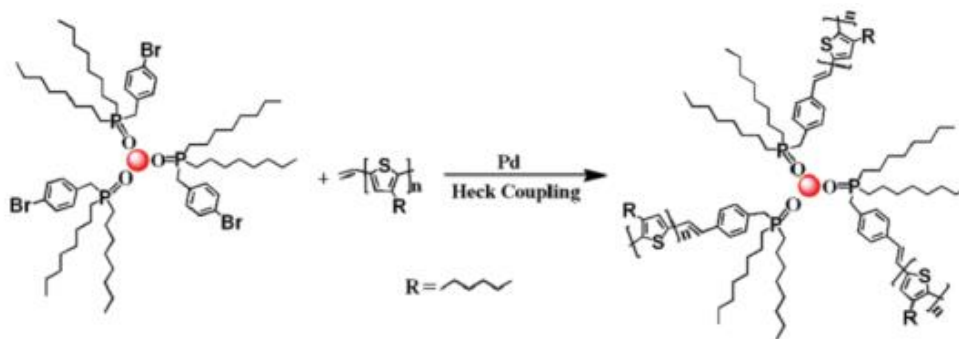


**Figure 2.5.** Illustration of grafting vinyl-terminated P3HT onto CdSe QDs utilizing bifunctional ligands (DOPO-Br). [Reprinted with permission from ref. 13, Copyright @ 2007 American Chemical Society.]

In order to fully exploit the good charge transport characteristic of semiconductor inorganic NCs (e.g., CdSe and CdTe) and enable the intimate contact of NCs with CPs for efficient charge separation, the shape of NCs (e.g., CdSe<sup>23a</sup> and CdTe<sup>23b</sup>) was controlled by utilizing bifunctional short ligands as introduced by Zhao et al.<sup>23a</sup> and Jung et al.,<sup>23b</sup> respectively. Specifically, a bifunctional ligand, 4-bromobenzyl phosphonic acid (BBPA) that coordinates strongly with (01 $\bar{1}$ 0) and (11 $\bar{2}$ 0) facets of CdSe NRs was prepared and used to promote the elongated growth of CdSe NRs, yielding BBPA-capped CdSe NRs. Subsequently, the end-functionalized P3HT (i.e., vinyl- or ethynyl -terminated) was grafted with bromide group of BBPA-capped CdSe NRs via Heck coupling or click chemistry, respectively.<sup>23a</sup> For the Heck coupling strategy, the reaction was similar to that between DOPO-Br-capped CdSe QDs and vinyl-terminated P3HT as described above.<sup>3</sup> For the click reaction, the bromide group on BBPA was converted into azide functionalities, forming N<sub>3</sub>-BPA-capped CdSe NRs. P3HT-CdSe NR nanocomposites were yielded via the catalyst-free Huisgen 1,3-dipolar cycloaddition between ethynyl-terminated P3HT and N<sub>3</sub>-functionalized CdSe NRs. It is interesting to note that P3HT-CdSe NR nanocomposites were prepared via a catalyst-free click reaction. By contrast, the Heck coupling approach required a Pd catalyst. Clearly, nanocomposites produced by click chemistry are more desirable for hybrid solar cells as there is no need for further purification to remove catalysts.

#### **2.4.3. *In-situ* growth of nanocrystals within the conjugated polymer matrix.**

Synthesizing inorganic NCs in the presence of CP as matrix represents a new route to intimate semiconductor hybrid CP-NC nanocomposites. It dispenses with the need for any further treatments, such as ligand exchange and the use of fully or partially

insulating ligands, involved in the synthesis as noted above.<sup>23c</sup> Recently, Dayal et al. synthesized CdSe nanoparticles without using a surfactant by utilizing the steric hindrance stemming from hexyl side chains of P3HT, yielding a simple mixture of CdSe/P3HT.<sup>23d</sup> Cadmium precursor, dimethylcadmium was dissolved in octadecene (ODE) and mixed with P3HT in 1,2,3-trichlorobenzene (TCB) solution. Subsequently, selenium in trioctylphosphine was injected to initiate the nucleation and growth. Interestingly, Liao et al. reported the *in-situ* growth of anisotropic CdS NCs in the P3HT matrix.<sup>23c</sup> In this work, a binary solvent (i.e., 1,2-dichlorobenzene (DCB) and dimethyl sulfoxide (DMSO)) was employed to dissolve both cadmium precursors (i.e., cadmium acetate) and P3HT. As the cadmium precursor concentration increased, the shape of NCs

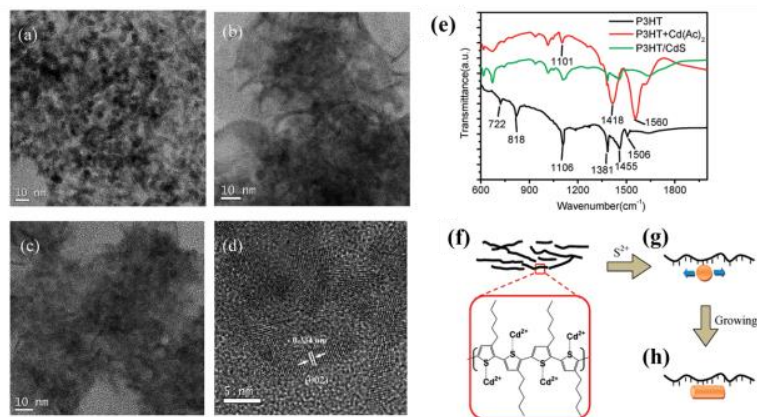


**Figure 2.6.** TEM images of CdS NRs within the P3HT matrix at the cadmium acetate concentration of (a) 2.5, (b) 8.3, and (c) 12.45 mg/mL. (d) Close-up TEM image of CdSe NR. (e) FTIR spectra of P3HT, P3HT with cadmium acetate, and CdS/P3HT nanocomposites. (f, g, and h) Proposed synthesis mechanism of CdS/P3HT nanocomposites. [Reprinted with permission from ref. 34, Copyright @ 2009 American Chemical Society.]

evolved from a spherical dot to a NR-like morphology (**Figure 2.6**). Based on the above observation, a growth mechanism for the formation of NRs was proposed and elucidated by FTIR measurement. A peak at wavenumber of  $1106\text{ cm}^{-1}$  corresponding to the S-C stretching of P3HT shifted to  $1101\text{ cm}^{-1}$  after the addition of cadmium acetate into P3HT, suggesting a reduction in bond energy of S-C (**Figure 2.6e**). This reflected that the system underwent an additional intermolecular interaction at the expense of S-C bond energy due probably to a strong dipole-dipole or ion-dipole interaction between S atoms of P3HT and  $\text{Cd}^{2+}$  from precursor. On the basis of this study, it was proposed that CdS NRs were grown along the P3HT backbone upon the anchoring of  $\text{Cd}^{2+}$  on the S atoms of P3HT as schematically illustrated in **Figure 2.6f-h**.

#### **2.4.4. The hybrid devices utilizing inorganic nanocrystals as an electron acceptor.**

Recent research progress in organic-inorganic hybrid solar cells is summarized in **table 2.1**. The power conversion efficiency (PCE) of hybrid cells reaches as high as 4.7%.<sup>34</sup> This value is still lower than that of polymer-fullerene solar cells, which exceeds 8% recently.<sup>16</sup> This is because carrier mobilities of colloidal nanocrystals (NCs) thin film are low regardless of its superior carrier mobility in bulk inorganic materials.<sup>54</sup> A critical challenge in organic-inorganic hybrid solar cells lies in the interfacial engineering between inorganic NCs and organic materials. For example, removing the insulating organic ligands of NCs is necessary to facilitate charge transfer between electron donating polymers and electron accepting inorganic NCs. However, it results the increased number of dangling bonds on the bare NCs which serves as charge trapping sites.<sup>34</sup>

**Table 2.1.** Performance of selected organic-inorganic hybrid solar cells.

Donor	Acceptor	Surface treatment	$J_{sc}$ (mA/cm <sup>2</sup> )	$V_{oc}$ (V)	FF (%)	PCE (%)	Ref
P3HT	CdSe NRs	Pyridine	5.7	0.7	40	1.7	[31]
P3HT	CdSe NRs	ethandithiol	7.4	0.73	54	2.9	[58]
PCPDTBT	CdSe NRs	ethandithiol	12.8	0.74	50	4.7	[58]
OC <sub>1</sub> C <sub>10</sub> -PPV	CdSe TPs	Pyridine	7.30	0.65	35	1.8	[121]
P3HT	ZnO NCs	Stabilized in methanol	2.19	0.69	55	0.92	[76]
P3HT	ZnO networks	<i>In-situ</i> growth in solid state film	5.2	0.75	52	2.0	[94]
MDMO-PPV	ZnO networks	<i>In-situ</i> growth in solid state film	2	1.14	42	1.1	[95]
MDMO-PPV	TiO <sub>2</sub> networks	<i>In-situ</i> growth in solid state film	0.6	0.52	42		[96]
P3HT	PbS QDs	Oleic acid	0.14	0.16	30	0.006	[113]
PDTPQx	PbS QDs	Butylamine	4.2	0.38	34	0.55	[84]
PSBTBT	PbS QDs	ethandithiol	10.82	0.63	51	3.48	[121]
P3HT	CdS NRs	Pyridine	2.28	0.85	46.2	0.89	[67]
P3HT	CdS networks	<i>In-situ</i> growth in solid state film	4.848	0.842	53.23	2.17	[68]

Pyridine is typically used as surfactant in the simple physical mixture system as the pyridine layer later can be removed during solvent evaporation process. The hybrid CdSe NCs and P3HT cells based on pyridine treated CdSe NCs exhibited the PCE of 1.7% which is comparable of that of P3HT and fullerene cells. It should be noted that ethandithiol treatment can further increase the performance up to 4.7 % by reducing the number of defect sites for charge recombination.<sup>34</sup> It is also note worth that the geometry

of NCs is important factor governing the performance of hybrid cells. For example, forming continuous network of inorganic NCs can facilitate charge carrier transport behavior, thus results increased PCE.<sup>43b, 55</sup>

## **2.5. Routes to improved device performance**

Notably, in spite of recent developments in synthesis of hybrid organic-inorganic nanocomposites, the performance of the resulting hybrid solar cells has not yet been compelling. This can be attributed to several reasons. First, hybrid solar cells may suffer from insufficient light absorption because of limited thickness of photoactive layer due to short diffusion length of charge carriers. Approximately half of solar energy in NIR region is not harvested owing to the large bandgap of most of CPs. Second, intrinsically high electron mobility of inorganic NCs for excellent charge transport has not yet been utilized to its full potential due to the difficulty in controlling the film morphology. An ideal device geometry comprising bicontinuous pathway for both holes and electrons is of key importance to enhance charge transport, thus reducing the recombination probability. In this context, several approaches to address these issues and potentially improve the device performance are followed.

### **2.5.1. Optimization of light absorption**

As noted in Section 1, due to limited thickness of photoactive layer, light absorption of CPs in polymer solar cells is not adequate as a result of short exciton diffusion length and the large bandgap of CPs. Thus, several techniques for light trapping have emerged, including the incorporation of metallic nanoparticles, diffraction gratings, and periodic nanostructures.<sup>56</sup> Among them, the inclusion of metallic nanoparticles such

as aluminum,<sup>57</sup> silver,<sup>58</sup> copper,<sup>59</sup> and gold<sup>24a, 59b</sup> was easily implemented in photoactive layer without compromising the device architecture. Gold and copper exhibit surface plasmon resonance (SPR) in the visible range,<sup>93,98</sup> while aluminum and silver display SPR in the ultraviolet range.<sup>93,98</sup> The improvement of light trapping can be ascribed to the scattering and a near-field enhancement.<sup>56a</sup> A strong interaction between the free conduction electrons in metal and the electromagnetic radiation occurs when the metal nanoparticle size is comparable or smaller than the wavelength of the incoming light. This oscillation of free electrons in accordance to the electromagnetic fields is termed as plasmons. The resonance condition when the frequency of light matches that of free electrons occurs and is defined as localized surface plasmon resonance (LSPR).<sup>57b, 59b, 60</sup> As a result, metallic nanoparticles enhance local fields in the surrounding area via the resonant plasmon excitation, thereby increasing the light absorption.<sup>56, 59c</sup> Au NCs with a size of 5~50 nm were found to enhance the local electric field up to 100 times by storing the energy in a localized plasmon modes as they acted as antennas for the incident light.<sup>60</sup> In this respect, Au NCs were incorporated either in the photoactive layer or the buffer layer (e.g., PEDOT:PSS) to further increase light absorption. The PCE of polymer solar cell with a device configuration of ITO/PEDOT:PSS/P3HT:PCBM/Ca/Al was indeed increased from 3.57% to 4.24% after incorporating 50-nm Au NCs into the PEDOT:PSS layer.<sup>24a</sup> The light absorption in Au-containing devices increased due to the LSPR-induced local field enhancement as reflected in the increase in incident photon-to-electron conversion efficiency (IPCE). The local field enhancement resulted in a rise in both  $J_{SC}$  and  $FF$  from 9.16 mA/cm<sup>2</sup> to 10.22 mA/cm<sup>2</sup>, and from 66.06% to 70.32%, respectively, while  $V_{OC}$  remained the same ( $V_{OC} = 0.59$  V). It has been reported that Au

NCs exhibit a low scattering efficiency regardless of high level of self-absorption.<sup>59b</sup> In contrast, Ag NCs show a high scattering efficiency.<sup>24b</sup> In this context, Au@Ag core/shell NCs were introduced to take advantage of both the broad LSPR absorption from Au NCs and the higher scattering characteristic from Ag NCs, respectively.<sup>24b</sup> Two devices were constructed: ITO/PEDOT:PSS/PTB7:PC<sub>70</sub>BM/TiO<sub>x</sub>/Al and ITO/PEDOT:PSS/PCDTBT:PC<sub>70</sub>BM/TiO<sub>x</sub>/Al with the incorporation of Au@Ag core/shell NCs in the PEDOT:PSS layer.<sup>24b</sup> Both the scattering and absorption were enhanced in Au@Ag NC-containing device (45 nm@10nm) compared to those in Au NC-containing device (45 nm), leading to increased PCEs: the PCE increased by 16% from 5.21% to 6.08% in PCDTBT:PC<sub>70</sub>BM-based devices, and by 12% from 7.78% to 8.74 % in PTB7:PC<sub>70</sub>BM-based devices.

Plasmonic metallic NCs were also used in photoactive layer to trap the light in the photoactive layer. Recently, Kim et al. investigated the effect of incorporating both dodecyl amine (DDA) stabilized Ag NCs (6.1 nm) and Au NCs (5.3 nm) into a poly(3-octylthiophene) (P3OT):C<sub>60</sub> photoactive layer on the device performance.<sup>61</sup> The PCEs were increased up to 70% for Au NC-incorporated device (1.7wt% Au NCs) and 50% for Ag NC-incorporated device (1.4wt% Ag NCs), respectively.<sup>61</sup> Charlie et al. reported the increase of PCE in ITO/PEDOT:PSS/poly[2,7-(9,9-dioctylfluorene)-alt-2-((4-(diphenylamino) phenyl)thiophen-2-yl)malononitrile] (PFSDCN):PCBM/LiF/Al solar cells when poly(ethylene glycol) (PEG)-capped Au NCs (18nm) were introduced to photoactive layer.<sup>62</sup> The concentration of Au NCs was varied from 0 to 6 wt%. The PCE increased by approximately 32% with the addition of 0.5wt% PEG-Au NCs, while further increase in Au NCs led to the decrease in PCE. This was due to the fact that the electrical

properties of Au NCs may counter-diminish the optical enhancement from their LSPR.<sup>62</sup> On the other hand, Topp et al. showed that the inclusion of DDA-capped Au NCs in the photoactive layer caused a reduced PCE.<sup>63</sup> The PCE decreased from 2.5% to 1.1 % in the ITO/PEDOT:PSS/P3HT:PCBM/Al device with the incorporation of 23wt% of DDA-stabilized Au NCs. This was probably because of the quenching of the excited state in P3HT<sup>63-64</sup> or the local short circuits<sup>64</sup> due to aggregation of Au NCs.<sup>95,105</sup>

We note that the strategy of incorporating plasmonic NCs in the PEDOT:PSS layer or photoactive layer of CP/fullerene BHJ solar cells discussed above may be readily extended to the CP-NC nanocomposite system for improved efficiency of hybrid CP/NC solar cells.

As discussed above, the absorption of NIR photons was limited as a direct consequence of the large bandgap of majority of electron-donating CPs. In order to absorb these long wavelength photons from the sunlight, low bandgap semiconductors such as PbS, PbSe, HgTe, FeS<sub>2</sub>, and Bi<sub>2</sub>S<sub>3</sub> were utilized. PbS NC is the most widely studied NIR absorbing material due to its intriguing properties (e.g., low bandgap, high dielectric constant, and large exciton Bohr radius (18 nm)).<sup>65</sup> In the early studies, P3HT/PbS NC hybrid nanocomposites were employed as photoactive layer.<sup>65d</sup> However, the overall performance was rather low (PCE = 0.01%) with a FF of 36%, a  $J_{sc}$  of 0.4 V, and a  $V_{oc}$  of 0.6  $\mu\text{A}/\text{cm}^2$ . Although a higher loading of PbS NCs was required, the addition of more NCs resulted in clustering. Several CPs such as poly(2,3-didecylquinoxaline-5,8-diyl-alt-Noctyldithieno[3,2-b:2',3'-d]pyrrole) (PDTPQx), poly(2,6-bis(3-n-dodecylthiophen-2-yl)-alt-N-dodecyldithieno[3,2-b:2',3'-d]pyrrole) (PDTPBT), and

poly(2,3-didecyl-pyrido[3,4-b]pyrazine-5,8-diyl-alt-N-dodecyldithieno[3,2-b:2',3'-d]pyrrole) (PDTPPPz) were also mixed with NIR absorbing PbS NCs for solar cell applications. The device based on a simple mixture of PDTPQx and PbS NCs exhibited two orders of magnitude greater efficiency (PCE = 0.55%,  $J_{sc}$  = 4.2 mA/cm<sup>2</sup>,  $V_{oc}$  = 0.38V, and  $FF$  = 34%) than that of its P3HT/PbS NC counterpart. Unfortunately, blending PbS NCs with most of CPs formed undesired type I heterojunction which is detrimental for solar cell applications. This is due mainly to low HOMO level of PbS NCs, thereby restricting the number of CPs which can be employed. Thus, the energy levels of PbS NCs were precisely controlled by tailoring the NC size. On the other hand, CPs (e.g., poly[2,6-(4,40-bis(2-ethylhexyl)dithieno[3,2-b:2',3'-d]silole)-alt-4,7(2,1,3-benzothiadiazole) (PSBTBT) with proper energy level was employed.<sup>66</sup> The explicit changes in  $V_{oc}$  and  $J_{sc}$  were observed, depending on the diameter of PbS NCs. The best PCE was found to be 3.48 % with a  $V_{oc}$  of 0.63 V, a  $J_{sc}$  of 10.82 mA/cm<sup>2</sup>, and a  $FF$  of 0.51, which was comparable to that of PSBTBT/PCBM solar cell (3.39 %).<sup>66</sup>

Utilizing NIR absorbing NCs such as PbS and PbSe is especially beneficial for singlet exciton fission photovoltaics. Singlet exciton fission is the process to generate two excitons from a high-energy single photon, thereby enabling the increase in current density.<sup>67</sup> The advantage of singlet exciton fission photovoltaics lies on the reduction of losses from thermalization.<sup>68</sup> The high-energy photons are first absorbed, generating a high-energy singlet excited state, which is later split into two low-energy states via singlet exciton fission. The produced triplet excitons have approximately half the energy of singlet excited state. Therefore, the  $V_{oc}$  of device is sacrificed to no more than half of

its previous value. Moreover, conjugated organic materials for exciton fission such as pentacene<sup>69</sup> have a large band gap, indicating that the empty absorption region of conjugated organic materials must be filled to capture low-energy photons. Thus, NIR absorbing NCs are incorporated to improve the product of photovoltage and photocurrent (i.e., power).<sup>70</sup> Ehrler et al. fabricated singlet exciton fission quantum dots solar cells utilizing pentacene and PbS NCs.<sup>70b</sup> The bilayer device structure was composed of ITO/pentacene/PbS NCs/ZnO/Al. The energy level of PbS NCs was carefully tuned so that holes can transfer from NCs to pentacene efficiently while favoring the ionization of triplet excitons of pentacene to PbS NCs. The resulting device had a PCE of 0.85% with a  $J_{sc}$  of 7.61 mA/cm<sup>2</sup>, a  $V_{oc}$  of 0.27 V, and a  $FF$  of 0.41. A similar bilayer device but employing lead selenide (PbSe) NCs as NIR absorbing materials was also studied.<sup>70b</sup> In contrast to PbS, the synthesized PbSe usually showed a narrower size distribution which enabled even close packing of NCs. The resulting singlet exciton fission device achieved a PCE up to 4.7% ( $V_{oc} = 0.48V$ ,  $J_{sc} = 19.9$  mA/cm<sup>2</sup>, and  $FF = 0.49$ ).

### **2.5.2. Geometry control over the morphology of photoactive layer**

In general, hybrid solar cells are fabricated using spin-casting or roll-to-roll processes to minimize the cost. However, microscopic phase separation usually occurs during these processes. Moreover, due to the lack of percolating network resulting from the granular and dispersed nature of the NC phase, the favorable characteristic of high intrinsic carrier mobility of inorganic NCs is not fully utilized. Several approaches to improving the device geometry for fast dissociation of excitons and transport of holes and electrons have been introduced, including (1) shape control of electron accepting NCs,<sup>23b, 27b, 71</sup> (2) *in-situ* growth of NCs within the CP film,<sup>55</sup> (3) infiltration of CPs into

mesoporous inorganic template (or NR arrays),<sup>72</sup> and (4) vertical assembly of NRs via the evaporation process.<sup>128,131-134</sup>

The structure of electron accepting NCs plays an important role in charge carrier characteristic. For example, tetrapod-shaped NCs carry a good charge carrier transport property than that of QDs and NRs.<sup>7c, 73</sup> This can be attributed to their three-dimensional structure (four arms symmetrically emanating from a central core), which enables continuous charge transport pathway in thin film regardless of their orientation.<sup>1</sup> Sun et al. reported that compared to CdSe NRs, enhanced device efficiency was obtained when CdSe tetrapods were mixed with poly(2-methoxy-5-(3',7'-dimethyl-octyloxy)-p-phenylenevinylene) (OC<sub>1</sub>C<sub>10</sub>-PPV) in ITO/PEDOT:PSS/OC<sub>1</sub>C<sub>10</sub>-PPV:CdSe NC/Al devices.<sup>71</sup>

The percolating network of NCs in the CP film can be achieved via *in-situ* growth of NCs in the presence of CPs.<sup>55</sup> In this approach, organometallic precursors dissolved in CPs solution are deposited on substrates and followed by thermal annealing, yielding NC network within the CP film. Oosterhout et al. fabricated ITO/PEDOT:PSS/P3HT:ZnO/Al solar cells using this approach.<sup>55a</sup> Specifically, a mixture of diethylzinc and P3HT was spin-coated on the substrate and annealed at 100°C, forming an interpenetrating ZnO network in P3HT film. The device showed a PCE of 2.0% ( $V_{oc} = 0.75$  V,  $J_{sc} = 5.2$  mA/cm<sup>2</sup>, and  $FF = 0.52$ ). Similarly, a network of TiO<sub>2</sub> NCs was formed in the poly[2-methoxy-5-(3',7'-dimethyloctyloxy)-p-phenylene vinylene] (MDMO-PPV) film using titanium(IV) isopropoxide.<sup>55c</sup> The resulting device with the

configuration of ITO/PEDOT:PSS/MDMO-PPV:TiO<sub>2</sub>/LiF/Al showed a  $V_{oc}$  of 0.52 V, a  $J_{sc}$  of 0.6 mA/cm<sup>2</sup>, and a  $FF$  of 0.42 under 0.7 sun intensity.

Donor/acceptor bicontinuous architecture was also crafted by infiltrating nanoporous inorganic template (or rigid NR-like structure) with CPs.<sup>72a</sup> Coakly et al. reported that P3HT infiltrated mesoporous titania film and showed that 33% of the total volume of film was filled with TiO<sub>2</sub>.<sup>72b</sup> Ravirajan et al fabricated the solar cell with a ITO/ZnO/Z907/P3HT/PEDOT:PSS/Au configuration by infiltrating P3HT into ZnO NR arrays.<sup>74</sup> The device efficiency was 0.2 % with a  $J_{sc}$  of 2 mA/cm<sup>2</sup>.

Vertically oriented assemblies of inorganic NRs have been prepared by the following methods: (1) self-evaporative drying,<sup>75</sup> and (2) utilization of external fields (e.g., magnetic field or electric field).<sup>75b, 76</sup> For the solvent-assisted evaporation technique, the pinning of three-phase contact line of a drying droplet led to the capillary flow of nonvolatile solutes (e.g., NRs) within the droplet to its edge, forming smectic or nematic superstructure. The entropically driven depletion force played a key role in assembly regardless of its weak strength.<sup>75a</sup> Vertically aligned architectures can also be achieved by applying electric field in case of NRs with intrinsic dipole moments (e.g., CdSe and CdS). The vertical assembly of NRs can be facilitated when the electric field-induced torque on NRs was greater than the thermal excitation energy ( $kT$ ).<sup>77</sup> For example, the dipole moment of CdSe NRs was calculated to be ~1450 D, and the electric field was 10<sup>7</sup> V/m. The strength of the torque applied on NRs was then  $4.872 \times 10^{-20}$  Nm.<sup>77b</sup> This value was one order of magnitude larger than thermal energy at room temperature.<sup>77b</sup> Therefore, vertical alignment of NRs was promoted with the assistance of electric field. Ahmed et al.

successfully aligned CdS NRs using electrophoresis which applies an electric field on charged particles in solution to cause electromigration of particles toward the oppositely biased electrodes.<sup>77a</sup> The perpendicular orientation of CdS NRs was formed due to their constituent dipole moment from their non-centrosymmetric wurtzite structure.<sup>77b</sup> However, it is necessary to incorporate electron donating materials (e.g., CPs) along with the aligned electron accepting NRs for photovoltaic applications. To this end, several research groups have reported vertical alignment of NRs within polymer matrices. Modestino et al. prepared vertically assembled CdSe NRs in the presence of polymer matrix such as P3HT and polyvinylcarbazole (PVK).<sup>75d</sup> However, CdSe NRs were aligned vertically, while excluding polymers from the NR arrays. Recently, corralled CdSe NR (8nm in diameter and 40nm in length) arrays were formed after phase separating from polymer matrix (e.g., PMMA and P3HT) due to the nonfavorable polymer-ligand interaction.<sup>78</sup>

### **2.5.3 Engineering conjugated polymers for high hole mobility.**

While semiconductor inorganic NCs have high electron mobility, the hole mobility of most of CPs is typically three orders of magnitude lower than that of NCs, thereby leading to charge accumulation in the film and increasing the possibility of recombination between electrons and holes in hybrid solar cells. To this end, several studies have been performed toward increasing the charge mobility of CPs. It is well-known that the mobility of CPs depends heavily on their crystallinity, the orientation of crystals with respect to the charge transport direction, and their molecular weights.<sup>79</sup> Therefore, careful control over the film morphology by judicious choice of solvent and deposition conditions is required. Recently, Ihn et al. reported the increased hole mobility

(up to  $0.1 \text{ cm}^2/\text{V}\cdot\text{s}$ ) of P3HT NWs in which P3HT chains were packed normal to the NW axis.<sup>80</sup> Greenham et al. fabricated devices utilizing CdSe NRs and P3HT nanofibers by selecting high boiling solvents (e.g., 1,2,3-trichlorobenzene (TCB), thiophene, and chloroform for comparison).<sup>81</sup> The PCE of hybrid solar cell prepared using TCB was 2.9% with a  $V_{oc}$  of 0.62 V, a  $J_{sc}$  of  $8.79 \text{ mA}/\text{cm}^2$ , and a  $FF$  of 0.5, while for the device made using chloroform, these numbers were 1.8%, 0.66 V,  $6.12 \text{ mA}/\text{cm}^2$ , and 0.41, respectively. The increase in current density for the device fabricated by TCB showed clear evidence of self-organization of P3HT, which resulted in higher hole mobility due to the electron delocalization via the  $\pi$ - $\pi$  interaction.<sup>81</sup> Kim et al. introduced a simple yet robust doping strategy to increase the hole mobility of CPs (e.g., P3HT and PTB7).<sup>82</sup> The charge-transport regions were formed after infiltrating doping of a solution-processable vanadium oxide (s-VO<sub>x</sub>). The efficiency of ITO/TiO<sub>x</sub>/P3HT:PCBM/ PEDOT:PSS/Ag devices decreased from 3.13% to 1.36% when the thickness of photoactive layer increased from 120 nm to 420 nm. Quite intriguingly, the replacement of PEDOT:PSS with vanadium oxide s-VO<sub>x</sub> led to a PCE enhancement from 3.34% (at the thickness of photoactive layer of 120 nm) to 3.45% (420 nm).

It is expected that the CP engineering strategy for enhanced hole mobility can also be applied to CP-NC nanocomposites for improved device efficiency of hybrid CP/NC solar cells.

## 2.6. Summary and outlook

In spite of recent progress in semiconductor organic/inorganic hybrid solar cells, the PCE was not satisfactory. Much effort has been focused on the following issues to

yield devices with potentially improved performance, including the optimization of light absorption by harvesting NIR photons, the efficient exciton dissociation, and the improved charge carrier transport. To enhance light harvesting, low bandgap CPs have been designed and synthesized. Utilizing NIR absorbing inorganic NCs and incorporating plasmonic NCs can also lead to improved light absorption. Crafting intimate organic-inorganic nanocomposites has emerged as an appealing strategy to enhance exciton dissociation as well as to prevent the aggregation of inorganic NCs. Although ligand exchange is the most versatile method to place functional groups on the NC surface, the grafting density of CPs on the NC surface is usually low due to the entropy loss of CPs. To overcome this problem, direct grafting of CPs and *in-situ* growth of NCs in the presence of CPs have been exploited to craft intimate contact between CPs and NCs, thus facilitating charge separation.

Moreover, newly developed star-like block copolymer nanoreactor (i.e., template) strategy for a large diversity of nearly monodisperse plain, core/shell, and hollow NCs (e.g., PbTiO<sub>3</sub>, BaTiO<sub>3</sub>, TiO<sub>2</sub>, CdSe, Au, and Pt) with precisely controlled dimensions, compositions and architectures<sup>23b</sup> can be further explored to create CP-NC nanocomposites in which CPs and NCs are not only intimately contacted as in the abovementioned direct grafting and *in-situ* growth approaches, but also permanently linked to one another, thereby imparting the long-term stability of CP-NC nanocomposites for high-performance hybrid solar cells. Specifically, in star-like diblock copolymer nanoreactor approach, an amphiphilic diblock copolymers composed of inner hydrophilic and outer hydrophobic blocks were synthesized by sequential atom transfer polymerization (ATRP) of two dissimilar polymers from a  $\beta$ -cyclodextrin core. As each

block was grown by ATRP, a living polymerization technique, the molecular weight and molecular architecture of star-like diblock copolymer were well-defined. The preferential coordination reaction between functional groups of inner hydrophilic blocks and metal moieties of precursors yielded extremely uniform NCs closely and permanently tethered with outer hydrophobic blocks that render the superior solubility in non-polar solvents and long-term stability. By extension, an intimately linked CP and semiconductor NC can also be crafted by capitalizing on amphiphilic star-like coil-rod diblock copolymers (for example, star-like poly(acrylic acid)-*block*-poly(3-hexylthiophene) (PAA-*b*-P3HT)) as nanoreactors. Such amphiphilic coil-rod diblock copolymers can be synthesized by click reaction of end-functionalized CP (e.g., ethynyl-functionalized P3HT) with star-like hydrophobic coil-like homopolymers containing complementary terminal functional groups (e.g., N<sub>3</sub>). The latter can subsequently be hydrolyzed into hydrophilic blocks in which their functional moieties (e.g., carboxyl group) provide the coordination sites to react with metal moieties of precursors of semiconductor NCs. This strategy may open an avenue to craft myriads of intimate and stable semiconductor organic-inorganic nanocomposites with well-controlled sizes and compositions for hybrid solar cells with improved device performance. It is noteworthy that similar strategy can also be employed to create CP-capped plasmonic NCs. The incorporation of such CP-functionalized metallic NCs in the photoactive layer of hybrid solar cells is expected to prevent (or largely reduce) the segregation of metallic NCs and improve the light harvesting efficiency.

Regarding charge carrier transport, the control over the morphology of CP-NC nanocomposites in photoactive layer remains a challenge. Ordered nanostructures with

bicontinuous pathways for both holes and electrons are regarded an ideal geometry for high efficiency, as they render the efficient charge transport and reduce the charge recombination. In particular, vertically aligned semiconductor CP-capped NRs formed by evaporative self-assembly may offer an opportunity for high-performance solar cells by providing vectorial charge transport and concurrently maximizing the interfacial areas of CP donors/NR acceptors. Furthermore, balancing carrier mobilities between CPs and NCs (i.e., increasing the hole mobility in the CP phase) is also the key to highly efficient solar cells as it reduces the charge accumulation in CPs. Several approaches have been developed to increase the hole mobility of CPs, for example by infiltrating doping as described above. Clearly, research on semiconducting CPs needs to be advanced, including tailoring their bandgaps and increasing their charge carrier mobilities. Moreover, interfacial control and engineering would also remain as an active area of exploration for hybrid solar cells with improved performance.

### **3. Semiconducting conjugated polymer grafted CdSe nanorod nanocomposites**

Jaehan Jung, Young Jun Yoon, and Zhiqun Lin, “*Semiconducting Conjugated Polymer-inorganic Nanorods Nanocomposites for Hybrid Photovoltaics*” (manuscript in preparation)

#### **3.1. Introduction**

Conjugated polymers (CPs) have drawn considerable attention as promising materials in the field of solar cells, light-emitting diodes (LEDs), thin film transistors, and biosensors. Their advantageous properties such as lightweight, flexibility, and large area producibility open up new opportunities for easy and low-cost manufacturing of optoelectronic devices. Among various types of CPs, poly(3-hexylthiophene) (P3HT) is one of the most extensively studied semiconducting CPs owing to its solution-processability, tailorable electrochemical properties, and high hole mobility. Semiconducting NCs exhibit tunable optoelectronic properties, including band gap, emission, and absorption range due to their quantum-confined nature, rendering them a wide range of applications in photovoltaic cells, tunable lasers and LEDs. Moreover, they possess high electron mobility, especially compared to that of CPs, thus are an appealing candidate as electron acceptors.

Organic/inorganic solar cells composed of semiconducting CPs and NCs are favorable alternative to inorganic solar cells due to the complementary advantages of NCs and CPs. However, hybrid cells prepared using simple physical blending between CPs and NCs suffered from several problems, including microscopic phase separation as well as the existence of insulating interfacial layer, thus limiting the performance of the resulting devices due to the poor charge transfer and transport from CPs to NCs or NCs to CPs. To address these problems, the chemical tethering of CPs onto the NC surface was introduced to achieve an excellent dispersion of NCs in the CP matrix as well as to promote the electronic interaction between these two semiconductors. Recently, P3HT-CdSe NC nanocomposites prepared via click coupling of P3HT onto CdSe NC surface showed an excellent charge transfer from P3HT to CdSe in comparison to the simple physical mixture of P3HT/CdSe NC.

In this study, we first aimed to craft P3HT-CdSe nanorod (NR) nanocomposites via a click chemistry utilizing bifunctional ligands (i.e., 4-bromobenzyl phosphonic acid and 4-bromomethyl benzoic acid). Although our previous work used 4-bromobenzyl phosphonic acid as bifunctional ligands, in the present study we discovered a synthetic route to CdSe NRs by utilizing 4-bromomethyl benzoic acid because of its ease of displacement of halide group (i.e., bromide) into azide group compared to 4-bromobenzyl phosphonic acid. Compared to QDs where multiple hopping process is required, the long axis of NRs provides continuous path way for carrier transport, which is advantageous. It is noteworthy that the device performance may be enhanced if the proper alignment of NRs can be achieved (i.e., vertical alignment of NRs to the substrate). Specifically, P3HT-CdSe NR nanocomposites were synthesized utilizing bifunctional ligands via

catalyst-free click chemistry. 4-bromomethyl benzoic acid (BrCH<sub>2</sub>-BA) and 4-bromobenzyl phosphonic acid (Br-BPA) were employed as bifunctional ligands in this study as carboxylic acids and phosphonic acids are most widely used capping agent for CdSe NCs and their bromine moiety can be coupled with end-functionalized CPs. We then used P3HT-CdSe NR nanocomposites as an active layer to prepare hybrid bulkheterojunction solar cells. To this end, BrCH<sub>2</sub>-BA-functionalized CdSe NRs and Br-BPA-capped CdSe NRs were prepared by hot injection method and bromine moiety of BrCH<sub>2</sub>-BA and Br-BPA were converted into azide group, yielding N<sub>3</sub>CH<sub>2</sub>-BA-functionalized CdSe NRs or N<sub>3</sub>-BPA-capped CdSe NRs. Subsequently, synthesized ethynyl-terminated P3HT were grafted onto CdSe NR surface via click chemistry, producing P3HT-CdSe NR nanocomposites. The success of grafting was confirmed by Fourier transform infrared spectroscopy (FTIR) and nuclear magnetic resonance spectroscopy (<sup>1</sup>H NMR). The optical properties of P3HT-CdSe NR nanocomposites were explored with absorption and photoluminescence studies. Solar cell devices were fabricated by spin-casting the as-prepared P3HT-CdSe NR nanocomposites. The influence of weight ratio of CdSe NRs and P3HT on the device performance was examined.

### 3.2. Experimental

All chemicals, including 4-bromomethyl benzoic acid, 4-bromobenzyl bromide, triethyl phosphite, cadmium oxide, sodium azide, selenium powder, sodium azide, 2,5-dibromo-3-hexylthiophene, Ni(dppp)Cl<sub>2</sub>, tert-butylmagnesium chloride (2mol/L in

diethyl ether), and ethynylmagnesium bromide (0.5 mol/L in THF) from Sigma Aldrich, hexylphosphonic acid (HPA, 97%), tetradecyl phosphonic acid (TDPA, 97%), octadecyl phosphonic acid (ODPA, 97%), stearic acid (SA, 97%), and tri-n-octylphosphine (TOP, 90%), from Alfa Aesar, and tri-n-octylphosphine oxide (TOPO, 90%) from Strem chemicals were used as received. THF (VWR, 99%) was refluxed over sodium wire and distilled from sodium naphthalenide solution.

***Synthesis of 4-bromobenzyl phosphonic acid (Br-BPA):*** Bifunctional ligand in this study was synthesized using Arbuzov reaction. 4-bromobenzyl bromide and triethyl phosphite at 1:2 molar ratio were heated under Ar at 150°C for 5 h, yielding diethylphosphonate ester. The excess triethyl phosphite and byproducts were removed by rotary evaporator at 100°C for several hours. Diethylphosphonate ester was hydrolyzed with concentrated aqueous HCl by heating at 100°C overnight, yielding bromobenzylphosphonic acid (BBPA). After cooling to room temperature, BBPA was filtered, redissolved in acetonitrile, and finally recrystallized in ethyl acetate.

***Synthesis of ethynyl-terminated poly(3-hexylthiophene) (P3HT):*** Ethynyl-terminated P3HT (i.e., P3HT≡) was synthesized through a quasi-living Grignard metathesis (GRIM) method. 2,5-dibromo-3-hexylthiophene (0.815g, 2.5 mmol) was dissolved in anhydrous THF (5ml) in a round bottom flask (250 ml) and stirred under Ar. Subsequently, tert-butylmagnesium chloride (1.25ml, 2.5mmol) was added and then the mixture was stirred for 2 h at room temperature. After it was diluted with 25mL of anhydrous THF, the addition of Ni(dppp)Cl<sub>2</sub> (56 mg, 0.1 mmol) was followed to initiate polymerization. The resulting solution was stirred for 30 min at room temperature,

producing intermediate P3HT; it was then reacted with ethynylmagnesium bromide (2ml, 1mmol) in THF for 30 min, yielding ethynyl-terminated P3HT (P3HT≡). The product was obtained by precipitating the reaction mixture in methanol, filtering in an extraction thimble, and washing by Soxhlet extraction with methanol, hexane, and chloroform sequentially. It was recovered after chloroform evaporated.

***Preparation of Br-BPA-capped CdSe NRs:*** Cadmium selenide (CdSe) NRs with approximately 5 nm in a diameter and 40 nm in a length capped with 4-bromobenzylphosphonic acids (Br-BPA) were synthesized via hot injection technique by following the previous report. A mixture of 67 mg of Br-BPA, 333 mg of n-octadecyl phosphonic acid (ODPA), 1.5g of trioctyl phosphine oxide (TOPO), and 0.1 g of CdO was degassed at room temperature in vacuum and subsequently at 120°C for 60 min in a 25 ml three-neck flask connected to a Liebig condenser. It was then heated under Ar slowly until the CdO decomposed, and the solution turned clear and colorless. Next, 0.7 ml of TOP was added, and the temperature was further raised to 320 °C. Next, 36 mg selenium dissolved in 0.5 ml TOP was rapidly injected to the vigorously stirred Cd precursor and the NR was allowed for 5 min. The heating mantle was then removed to stop the reaction. After cooling the solution to 60°C, 2 ml THF were added to the flask. The Br-BPA-capped CdSe was isolated by repeated dissolution in THF and precipitation in methanol for three times.

***Preparation of BrCH<sub>2</sub>-BA -capped CdSe NRs:*** BrCH<sub>2</sub>-BA-functionalized CdSe NRs were synthesized by modifying from the previous study. 1 mmol of CdO, 0.5 mmol of 4-bromomethyl benzoic acid (BrCH<sub>2</sub>-BA), 1.5 mmol of alkyl ligands (i.e., TDPA, HPA,

ODPA, and stearic acid), and 1.2 g of TOPO were placed in three neck flask. The mixture then degassed at 120°C for 60 min and was then heated to 300 °C under Ar to result the decomposition of CdO. After the solution became clear and colorless, 0.7 ml of 1M Se/TOP solution injected swiftly at 300 °C to initiate the nucleation and growth. Then heating mantle was removed to stop the reaction. When the solution cooled down to 60°C, 2 ml of THF were added. The BrCH<sub>2</sub>-BA-capped CdSe NRs were purified by precipitation with the excess amount of methanol. For the study of the shape evolution of CdSe NCs under different molar ratio between BrCH<sub>2</sub>-BA and alkylphosphonic acid, the ratio of TDPA: BrCH<sub>2</sub>-BA was controlled to be 1:0, 3:1, 1:3, and 0:1.

***Grafting ethynyl-terminated P3HT onto CdSe NRs:*** Sodium azide (NaN<sub>3</sub>) was added to Br-BPA-capped CdSe NRs (or Br-CH<sub>2</sub>-BA-capped CdSe NRs) in THF solution. The mixture was then sealed and stirred at room temperature for three days. Excess amount of NaN<sub>3</sub> was removed by centrifugation for three times. The resulting azide-benzylphosphonic acid-capped CdSe NRs (N<sub>3</sub>-BPA-CdSe NRs) or azidomethyl benzoic acid (N<sub>3</sub>CH<sub>2</sub>-BA-CdSe NRs) were then precipitated with the excess amount of methanol. Subsequently, 50 mg of P3HT≡ and 50 mg of N<sub>3</sub>-BPA-CdSe NRs (or N<sub>3</sub>CH<sub>2</sub>-BA-CdSe NRs) were mixed in 20 ml THF and stirred at 65°C under Ar for two days. The final product (i.e., P3HT-CdSe NR nanocomposites by coupling P3HT≡ with N<sub>3</sub>-BPA and N<sub>3</sub>CH<sub>2</sub>-BA) was cooled to room temperature and diluted 10 times with THF. The resulting solution was precipitated with methanol twice to remove uncoupled P3HT.

***Fabrication of photovoltaic devices:*** Photovoltaic devices were fabricated by following the procedure developed in the group. ITO glasses (2.5 cm by 1.5 cm) were

etched with hydrochloric acid and zinc powder to pattern lines with a width of 0.5 cm in the center. Patterned ITO glasses were washed with acetone, methanol, and isopropanol, respectively, followed by drying with nitrogen flow. Subsequently, PEDOT:PSS (Poly(3,4-ethylenedioxythiophene):poly(styrenesulfonate)) layer of 40 nm thickness were spin-casted on oxygen plasma cleaned ITO glasses and annealed at 140 °C for 40 min in air. P3HT-CdSe NR nanocomposites dissolved in chloroform (or chloroform and chlorobenzene mixture) with a concentration of 30mg/ml were spin-coated, forming approximately 100~200-nm thick photoactive layer. For thermal annealing process, samples were annealed at 130 °C for 10, 15, and 20 min. The 100 nm of aluminum electrode was deposited with a thermal evaporator at  $10^{-6}$  torr. All the fabrication was done in the inert atmosphere. Devices were characterized at 25 °C under AM1.5 conditions.

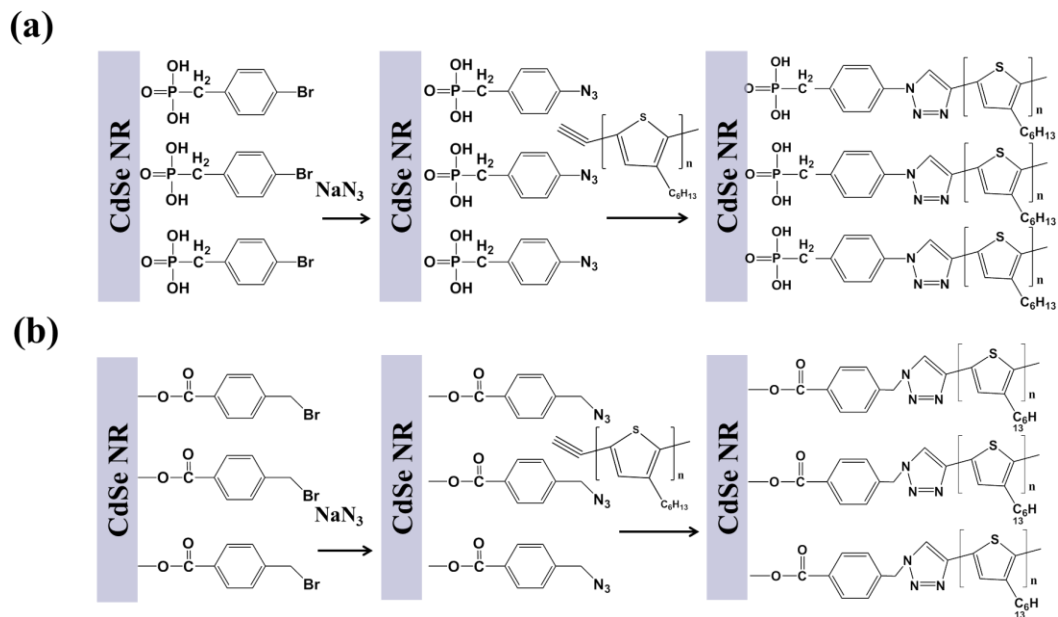
*Characterizations:* The morphology of CdSe NRs and P3HT-CdSe NR nanocomposites were characterized by low-resolution and high-resolution transmission electron microscopy (TEM) (JEOL 100CX, JEOL 4000EX, and Tecnai F30). For TEM sample preparation, the nanocomposite solution was dropped on the carbon TEM grid and dried in air. In order to confirm the occurrence of grafting between P3HT-≡ and N<sub>3</sub>-BPA-CdSe NRs (or BrCH<sub>2</sub>-BA-capped CdSe NRs), the <sup>1</sup>H NMR spectra (Varian VXR-400 spectrometer) and Fourier transform infrared spectroscopy (FTIR) were examined. The absorption spectra were recorded with a UV-Vis spectrometer (UV-2600, Shimadzu).

### 3.3. Results and discussion

It has been reported that end-functionalized P3HT can successfully be grafted onto [(4-bromophenyl)methyl]dioctylphosphine oxide (DOPO-Br) functionalized CdSe QD surface via Heck coupling between bromide group of NCs and vinyl moiety of CPs. Grafting of CPs onto NC surface can be an elegant means of achieving the intimate contact between two semiconductor constituents as well as excellent dispersion of NCs in CPs matrix. However, it was not feasible to achieve anisotropic shape of NCs even at high monomer concentration owing to the nature of phosphine oxide ligands. Extremely rapid growth of NCs in phosphate at the high monomer concentration hindered the ability to adjust the monomer rate in the whole growth regime, thus resulting in primarily isotropic dot-like NCs. In contrast, phosphonic acid can not only effectively adjust the growth rate of NCs due to their stronger coordination with cadmium monomers than phosphine oxide but also bind selectively to (01 $\bar{1}$ 0) or (11 $\bar{2}$ 0) facets of CdSe NCs, leading to anisotropic growth of NCs.

Taken together, CdSe NRs were prepared in the presence of phosphonic acid ligands with the bifunctional ligands containing both anchoring group for NCs and functional moiety for chemical coupling. Semiconducting CP-grafted CdSe NR nanocomposites were synthesized via catalyst-free click coupling between ethynyl functionality in CPs and azide group in CdSe NRs, with no need for ligand exchange process. In this study, 4-bromomethyl benzoic acid (BrCH<sub>2</sub>-BA) and 4-bromobenzyl phosphonic acid (Br-BPA) were employed as bifunctional ligands with alkylphosphonic acid (e.g., tetradecylphosphonic acid (TDPA)) as carboxylic and phosphonic acid groups are broadly used anchoring agents for CdSe NC synthesis as well as bromine functional

moiety can easily be utilized for coupling reaction. It should be noted that additional aliphatic phosphonic acid ligands (e.g., TDPA) was added in order to avoid the aggregation or uncontrolled shape of NCs by providing enough hindrance among NCs as well as to induce elongated growth of CdSe NCs as phosphonic acids were selectively



**Scheme 3.1.** Grafting ethynyl-terminated P3HT (i.e., P3HT≡) onto (a) N<sub>3</sub>-BPA-functionalized CdSe NRs, and (b) N<sub>3</sub>CH<sub>2</sub>-BA-functionalized CdSe NRs by catalyst-free click chemistry, yielding P3HT-CdSe NR nanocomposites.

bound to (01 $\bar{1}$ 0) or (11 $\bar{2}$ 0) facets. Specifically, Br-BPA (or BrCH<sub>2</sub>-BA)-capped CdSe NRs were prepared employing bifunctional ligands followed by azidation of bromine group into azide group (**Scheme 3.1**). Subsequently, ethynyl-terminated P3HT were grafted onto azide-capped CdSe NR surface via catalyst-free click chemistry between these two constituents. Semiconducting P3HT-CdSe NR nanocomposites with Br-BPA bifunctional ligands were first synthesized via a click coupling. First, high quality Br-BPA-capped

CdSe NRs were prepared with the molar ratio of TDPA:BBPA of 4:1 to trigger anisotropic growth but to prevent the formation of branched structure which usually occurs when highly mobile and reactive monomers are used. The high-resolution TEM images revealed that CdSe NRs were 40 nm in length with a diameter of 5 nm and exhibited a good crystallinity (**Figure 3.1a and 3.1b**). The reason that CdSe NRs dispersed well was owing to the hindrance effect resulted from TDPA surfactant. The local weak aggregation was due to the self-assembly of Br-BPA capped CdSe NRs on the TEM grid during the solvent evaporation.

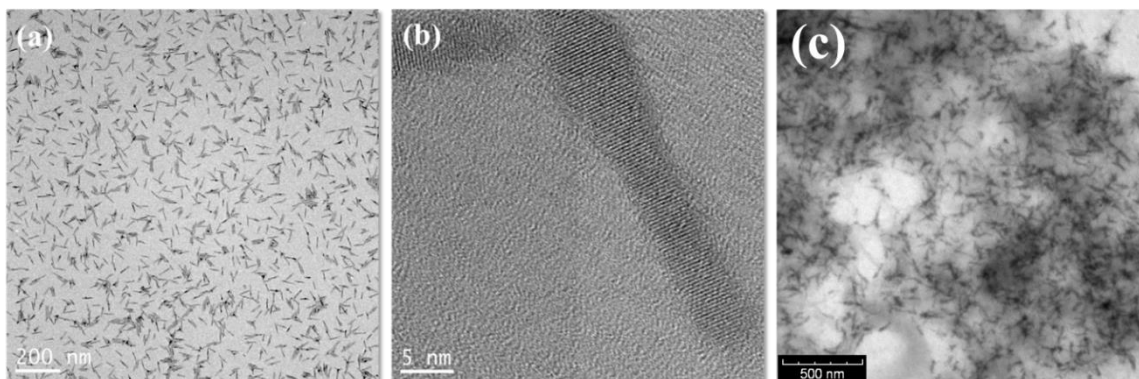


**Figure 3.1.** TEM images of (a) Br-BPA-functionalized CdSe NRs, (b) close-up of individual Br-BPA-functionalized CdSe NRs, and (c) P3HT-CdSe NR nanocomposites in P3HT matrix.

As illustrated in **Scheme 3.1**, the bromine end functional group of Br-BPA-capped CdSe NRs converted to azide, resulting in  $N_3$ -BPA-functionalized CdSe NRs. Subsequently, ethynyl-terminated P3HT was grafted onto  $N_3$ -BPA-functionalized CdSe NRs via a catalyst-free click coupling of azide of  $N_3$ -BPA with ethynyl end functionality of P3HT, yielding P3HT-CdSe NR nanocomposites. Notably, the resulting P3HT-CdSe

NR nanocomposites can be readily dispersed in the P3HT homopolymer matrix (**Figure 3.1c**).

The success of grafting P3HT chains onto N<sub>3</sub>-BPA-capped CdSe NRs was confirmed by the Fourier transform infrared (FT-IR) spectroscopy study (**Figure 3.2**). Alkyl chains in P3HT and ligands (i.e., TDPA) showed strong absorption at 2954 cm<sup>-1</sup>, 2915 cm<sup>-1</sup>, and 2850 cm<sup>-1</sup> due to the asymmetric C-H stretching vibrations in -CH<sub>3</sub>, -CH<sub>2</sub>,

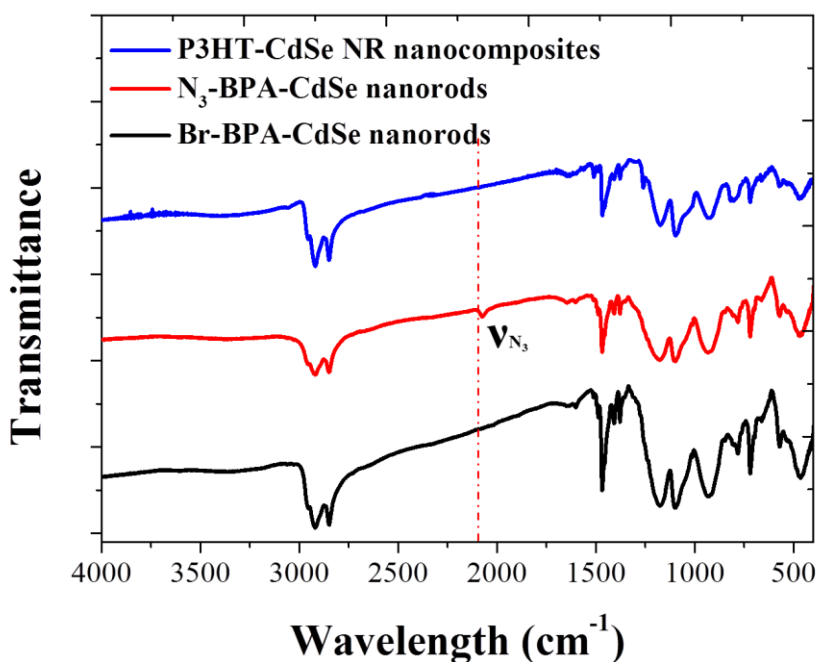


**Figure 3.2** FTIR spectra of Br-BPA-functionalized CdSe NRs (black), N<sub>3</sub>-BPA-functionalized CdSe NRs (red), and P3HT-CdSe NR nanocomposites (blue).

and the symmetric C-H stretching vibration in -CH<sub>2</sub>, respectively. Notably, the azide vibration characterization peak was appeared at 2040 cm<sup>-1</sup> after the substitution of bromine group into azide, indicating the successful conversion. It is noteworthy that N<sub>3</sub>-

BPA capped CdSe NRs were washed with water for three times and extracted with organic solvent to completely remove residue  $\text{NaN}_3$ . This peak was then completely disappeared when ethynyl-terminated P3HT was grafted onto  $\text{N}_3$ -BPA-functionalized CdSe NR surface, clearly suggesting the success of click chemistry.

The organic-inorganic hybrid bulkheterojunction (BHJ) solar cell devices were fabricated by utilizing P3HT-CdSe NRs nanocomposites as photoactive layer. The weight ratio between CdSe NRs and P3HT of P3HT-CdSe NR nanocomposites was 7:3 as determined by thermogravimetric analysis (TGA). The device structure was consist of ITO/PEDOT:PSS/P3HT-CdSe NR/Al as shown in **Figure 3.3a**. Specifically, oxygen plasma cleaned ITO glasses was spin-coated with PEDOT:PSS to improve the contact between PEDOT:PSS and P3HT-CdSe NR nanocomposites as well as to efficiently transport holes but to block electrons. Subsequently, as-synthesized P3HT-CdSe NR nanocomposites were dissolved in chloroform (CF) and chlorobenzene (CB) mixture at a concentration of 30mg/ml with CB of 20% by volume, and then spin-casted at 1200 rpm for 40 s on the PEDOT:PSS/ITO substrate without any further purification procedure. All the devices were annealed at 130 °C for 15 min in order to improve crystallinity of P3HT. The thickness of active layer was determined to be around 100 nm by AFM and profilometer. The resulting devices exhibited the power conversion efficiency (PCE) of 0.01 % with a short circuit current density ( $J_{sc}$ ) of 0.605  $\text{mA}/\text{cm}^2$ , an open circuit voltage ( $V_{oc}$ ) of 0.167 V, and a fill factor ( $FF$ ) of 27.56 (**Figure 3.3a**). The morphology of P3HT-CdSe NR nanocomposites film was examined using TEM as shown in **Figure 3.3b**. For the preparation of P3HT-CdSe NR nanocomposites film, the 40-nm thick P3HT-CdSe NR nanocomposites film coated on PEDOT:PSS were floated in water and scooped with a

TEM grid. Obviously, it was observed that P3HT-CdSe NRs were dispersed well in P3HT matrix in spite of rather low performance of the resulting devices compared with previously reports in literature. Further studies on electronic properties of P3HT-CdSe NR nanocomposites film will be required, which the subject of future study.

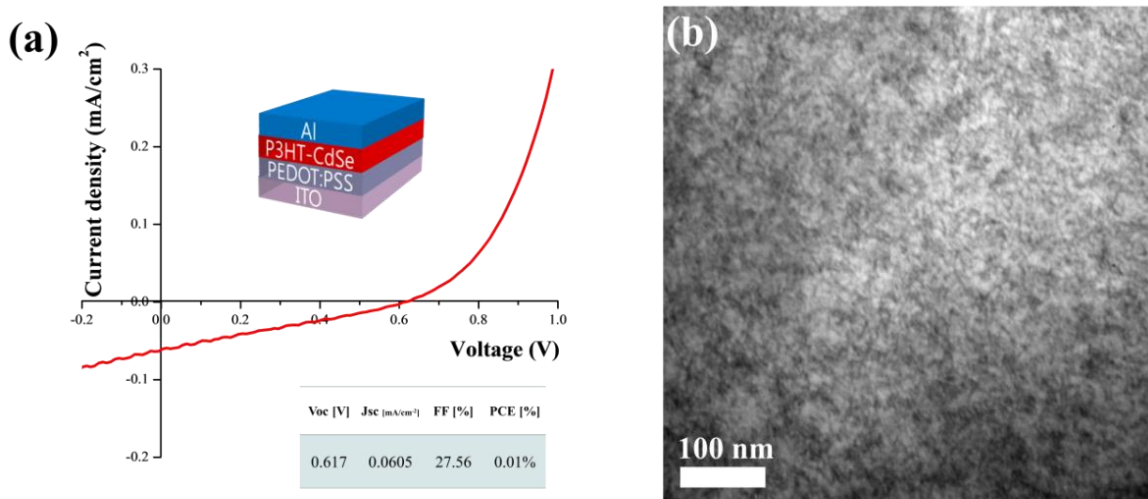


**Figure 3.3.** (a)  $J\sim V$  curve of photovoltaic device obtained at 1.5 AM illumination (the device configuration is shown in the inset). (b) TEM image of P3HT-CdSe NR nanocomposite film.

In addition, BrCH<sub>2</sub>-BA-capped CdSe NRs were synthesized in the presence of additional aliphatic ligands (i.e., TDPA) as the size and shape of CdSe NCs cannot be well controlled when only BrCH<sub>2</sub>-BA ligands were utilized (**Figure 3.5d**). The effect of the type of anchoring group (i.e., aliphatic carboxylic acid and phosphonic acid) and alkyl chain length of phosphonic acid ligands on the CdSe NC shape was investigated. First, CdSe NCs were grown in the presence of aliphatic ligands (i.e., stearic acid (SA), hexylphosphonic acid (HPA), tetradecylphosphonic acid (TDPA), or octadecylphosphonic acid (ODPA)) and bifunctional ligands (i.e., BrCH<sub>2</sub>-BA). The molar

ratio between aliphatic ligands and BrCH<sub>2</sub>-BA was 3:1 in all cases. When stearic acid (SA, aliphatic carboxylic acid ligands) was employed with BrCH<sub>2</sub>-BA, only spherical CdSe QDs were appeared (**Figure 3.4a**) regardless of the high mobile and reactive nature of BrCH<sub>2</sub>-BA ligands. This result was in stark contrast to the ODP: BrCH<sub>2</sub>-BA system where anisotropic CdSe structure was observed although this ligand had the same number of carbon (i.e., 18 carbons) as SA. This can be attributed to the binding nature of ligands such as the nature of the interface between the NCs and the ligands and the binding energy of ligands with surface facets. In general, phosphonic acids are known to bind strongly with cadmium atoms compared to other anchoring ligands (e.g., phosphine, amine, and carboxylic acid), thereby effectively adjusting the growth rate of NCs during the whole reaction regime and thus enabling elongated growth of NCs by avoiding sudden depletion of monomer precursors at the early stage. More importantly, phosphonic acid is known to bind stronger to the (01 $\bar{1}$ 0) or (11 $\bar{2}$ 0) surfaces than to the (0001) and (000 $\bar{1}$ ) facets (c-axis direction).<sup>45</sup> On the other hand, the binding energy of carboxylic acid with cadmium atoms was twice as small as that of phosphonic acid, thus resulted in more rapid growth of NCs, yielding usually larger spherical NCs instead of anisotropic NCs.

Notably, the use of phosphonic acids (i.e., hexylphosphonic acid, tetradecylphosphonic acid, and octadecyl phosphonic acid) with BrCH<sub>2</sub>-BA (i.e., BrCH<sub>2</sub>-BA: aliphatic phosphonic acid = 1:3) induced the anisotropic structure of CdSe NCs (**Figure 3.4bcd**). Interestingly, the use of HPA resulted in hyperbranched CdSe NCs instead of NRs because of the less steric hindrance effect resulted from the short alkyl chains as well as much mobile and reactive nature of Cd-HPA complexes compared to

their longer chain counterparts (i.e., Cd-ODPA or Cd-TDPA). Utilization of both TDPA and ODPA ligands lead nanorod architecture as longer alky chains provided enough steric hindrance, and reduces mobility and reactivity of monomers even in the presence of BrCH<sub>2</sub>-BA, thus prohibiting branched structure which is usually triggered by stacking

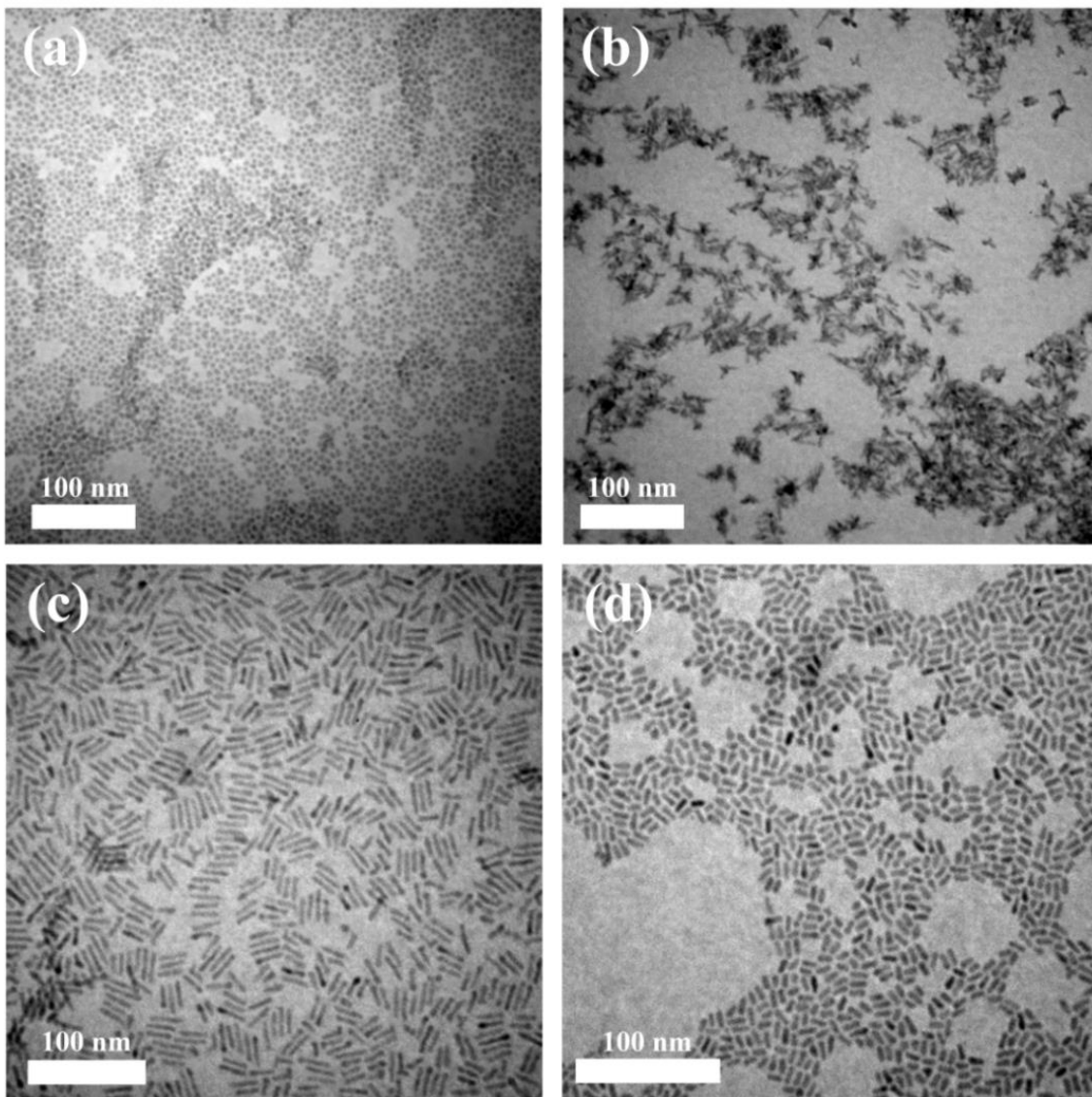


**Figure 3.4.** TEM images of CdSe NCs with different ligands with BrCH<sub>2</sub>-BA. (a) SA : BrCH<sub>2</sub>-BA = 3:1, (b) HPA : BrCH<sub>2</sub>-BA = 3:1, (c) TDPA : BrCH<sub>2</sub>-BA = 3:1, and (d) ODPA : BrCH<sub>2</sub>-BA = 3:1.

faults and twinning defects at the rapid reaction condition. Notably, phosphonic acid ligands with 18 carbons (i.e., ODPa) produced shorter nanorods compared to those prepared with tetradecylphosphonic acids (i.e., 14 carbons), which can be explained by the higher reactivity and mobility of Cd-TDPA than Cd-ODPA.

In order to investigate the influence of the molar ratio between alkyl phosphonic acid and short bifunctional ligands on the shape of CdSe NCs, TDPA/BrCH<sub>2</sub>-BA system was selected and the ratio between them were controlled to be 1:0, 3:1, 1:3, and 0:1, respectively. TEM studies revealed that CdSe QDs were synthesized when only TDPA was utilized while the addition of short mobile ligands (i.e., BrCH<sub>2</sub>-BA) caused anisotropic or branched structures, depending on the molar ratio of TDPA and BrCH<sub>2</sub>-BA. However, uncontrolled shape was observed in the absence of TDPA (**Figure 3.5d**) because mobile and reactive nature of Cd-BA-CH<sub>2</sub>Br monomers resulted in faster growth and thus more susceptible to defects such as stacking faults or twinning defects, showing extensive branching. It is noteworthy that BrCH<sub>2</sub>-BA clearly played a significant role in determining the shape of NCs, which can serve as indirect evidence of the existence of BrCH<sub>2</sub>-BA ligands on CdSe NR surface.

Semiconducting P3HT-CdSe NR nanocomposites based on BrCH<sub>2</sub>-BA bifunctional ligands were synthesized via click reaction (**Scheme 3.1b**). Similarly, the bromine end functional group of BrCH<sub>2</sub>-BA-capped CdSe NRs was converted to azide, resulting in N<sub>3</sub>CH<sub>2</sub>-BA-functionalized CdSe NRs and followed by grafting ethynyl-terminated P3HT onto N<sub>3</sub>CH<sub>2</sub>-BA-functionalized CdSe NRs via a catalyst-free click chemistry of N<sub>3</sub>CH<sub>2</sub>-BA with ethynyl moiety of P3HT, yielding P3HT-CdSe NR

nanocomposites. To confirm the conversion of bromine moiety into azide group in BrCH<sub>2</sub>-BA, <sup>1</sup>H NMR spectra was examined. Specifically, BrCH<sub>2</sub>-BA (1mmol) was dissolved in THF and then stirred with sodium azide (NaN<sub>3</sub>, 2mmol) for 12 h, which was the same condition when BrCH<sub>2</sub>-BA capped CdSe NRs were converted into N<sub>3</sub>CH<sub>2</sub>-BA capped CdSe NRs. The characterization peaks from protons from benzene rings and –

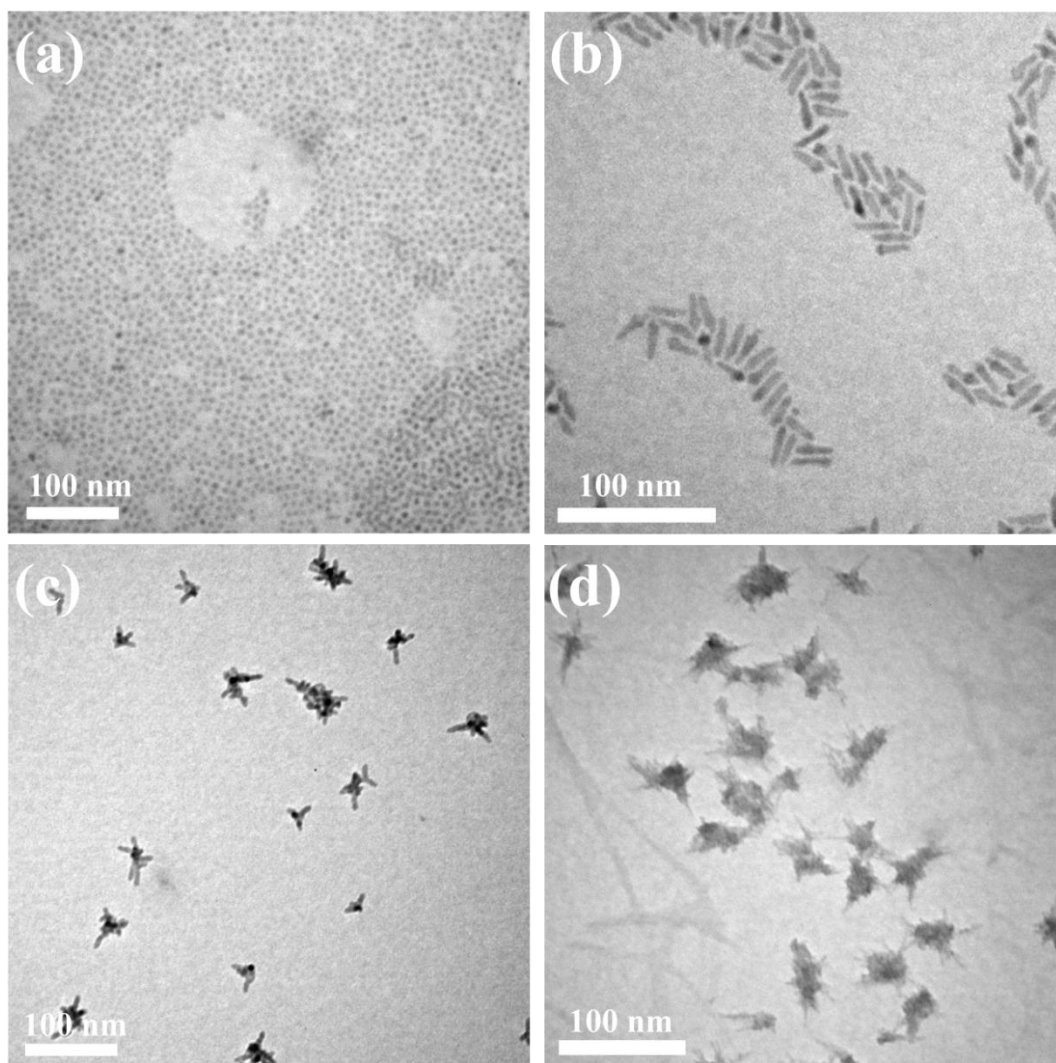


**Figure 3.5.** Low-magnification TEM images of CdSe NCs at different molar ratio of BrCH<sub>2</sub>-BA to TDPA. (a) BrCH<sub>2</sub>-BA:TDPA=1:0, (b) BrCH<sub>2</sub>-BA:TDPA=1:3, (c) BrCH<sub>2</sub>-BA:TDPA=3:1, and (d) BrCH<sub>2</sub>-BA:TDPA=0:1.

CH<sub>2</sub> near bromine adjacent to bromine moiety shifted to 4.53 ppm after converting bromine into azide (**Figure 3.6b**). The peaks at 7.90 and 7.53 ppm which can be assigned to the protons in a benzene ring were also shifted to 7.94 and 7.46 ppm, respectively, indicating the success of conversion.

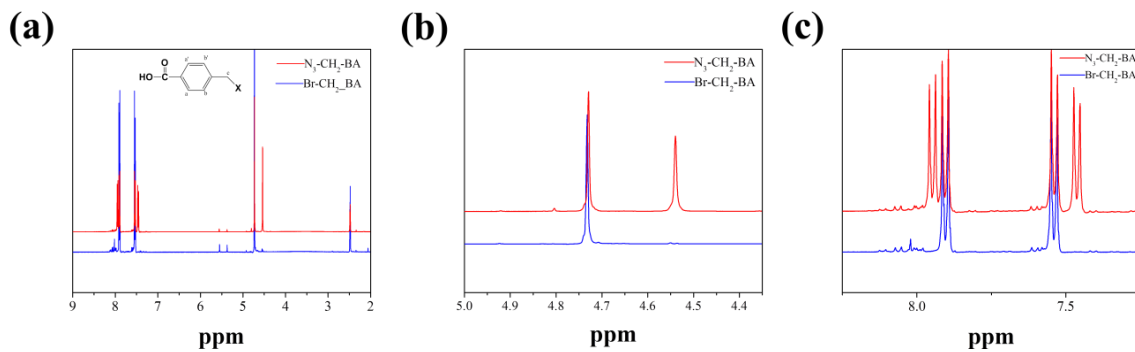


**Figure 3.6.** <sup>1</sup>H NMR spectra of (a) BrCH<sub>2</sub>-BA and N<sub>3</sub>CH<sub>2</sub>-BA, (b) the close-up at 4.7 ppm, and (c) the close-up at 7.5 ppm.

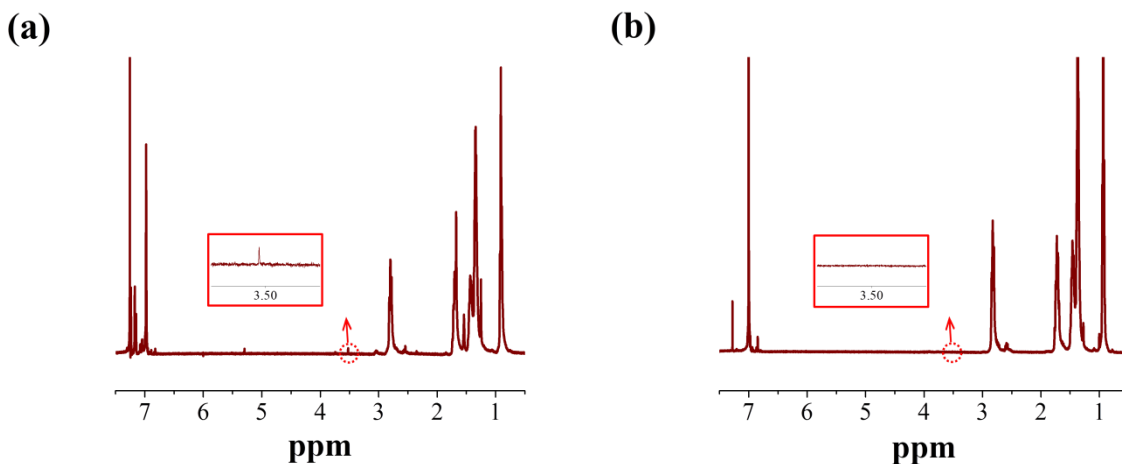


**Figure 3.7.** <sup>1</sup>H NMR spectra of (a) ethynyl-terminated P3HT, and (b) P3HT-CdSe NR nanocomposites.

The success of grafting P3HT chains onto  $N_3CH_2$ -BA-functionalized CdSe NRs was confirmed by the Fourier transform infrared (FT-IR, **Figure 3.8**) and  $^1H$  NMR measurements (**Figure 3.7**). Strong absorption at  $2954\text{ cm}^{-1}$ ,  $2915\text{ cm}^{-1}$ , and  $2850\text{ cm}^{-1}$  were assigned to the asymmetric C-H stretching vibrations in  $-CH_3$ ,  $-CH_2$ , and the symmetric C-H stretching vibration in  $-CH_2$ , respectively, from the alkyl side chains in P3HT and ligands. Obviously, the characteristic  $-N_3$  vibration was appeared at  $2040\text{ cm}^{-1}$  after the bromine groups of  $BrCH_2$ -BA-functionalized CdSe NRs were converted into azide groups, forming  $N_3CH_2$ -BA-functionalized CdSe NRs. This peak was then weakened after the  $N_3CH_2$ -BA-functionalized CdSe NRs coupled with ethynyl-

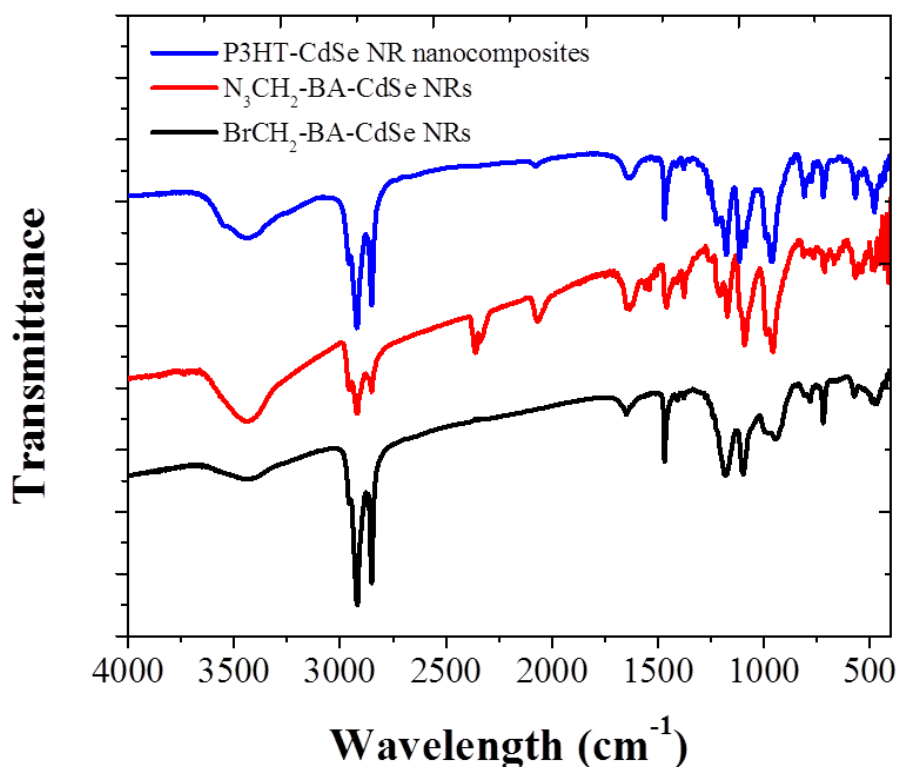


**Figure 3.8.** FTIR spectra of  $BrCH_2$ -BA-functionalized CdSe NRs (black),  $N_3$ - $CH_2$ -BA-functionalized CdSe NRs (red), and P3HT-CdSe NR nanocomposites (blue).

terminated P3HT via 1,3-dipolar cycloaddition between ethynyl group and azide group, suggesting some fraction of  $\text{N}_3\text{CH}_2\text{-BA}$  ligands on CdSe NRs were still remain. It should be noted that a proton signal at 3.5 ppm from the ethynyl group on the P3HT chain was completely disappeared after click chemistry of P3HT with  $\text{N}_3\text{CH}_2\text{-BA}$ -functionalized CdSe NRs, although the  $^1\text{H}$  NMR sample was prepared without separating detached P3HT. On the basis of the disappearance of ethynyl peak at 3.5 ppm from  $^1\text{H}$  NMR and the existence of weakened azide peak at  $2040\text{ cm}^{-1}$  from FTIR, it is clear that the amount of azide functional groups on the CdSe NR surface was enough to render the complete coupling of ethynyl groups on ethynyl-terminated P3HT.

Photophysical properties of P3HT-CdSe NR nanocomposites,  $\text{N}_3\text{-CH}_2\text{-BA}$  capped CdSe NR, and ethynyl-terminated P3HT in THF were explored by UV-vis absorbance and photoluminescence (PL) studies spectroscopy as shown in **Figure 3.9**.

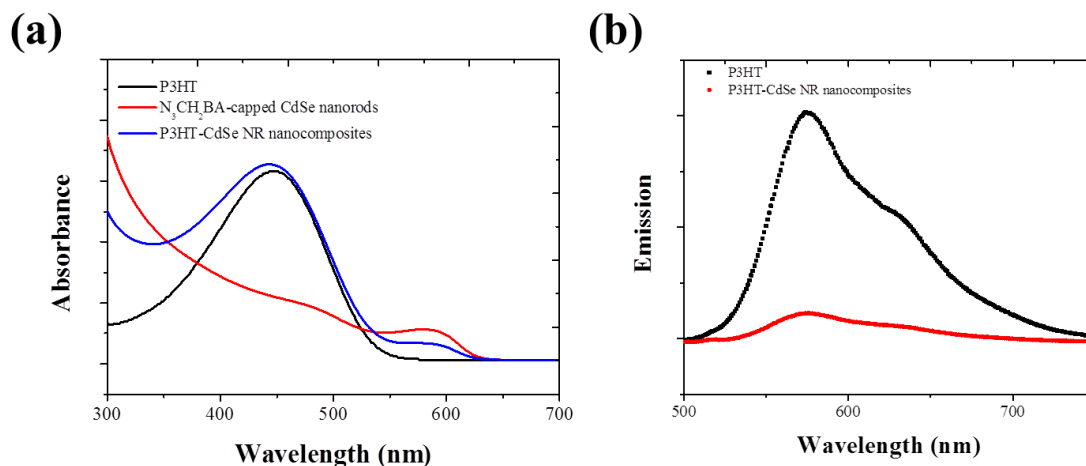
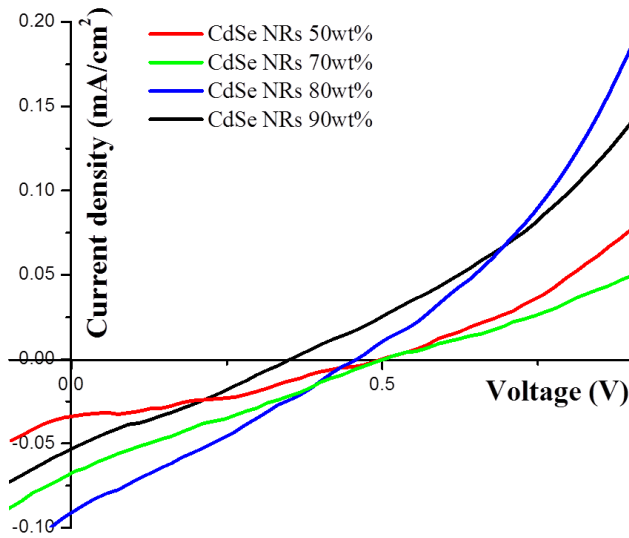


**Figure 3.9.** (a) The absorption spectra of ethynyl-terminated P3HT (black), BBPA-functionalized CdSe NRs (red), and P3HT–CdSe NR nanocomposites (blue) prepared by click chemistry. (b) Emission spectra of ethynyl-terminated P3HT (black) and P3HT–CdTe NR nanocomposites (red).

Obviously, the absorption of P3HT-CdSe NR nanocomposites showed the characteristic peaks from both constituents, with a 445-nm peak from P3HT and the absorption edge around 600 nm originated from CdSe NRs; this served as another evidence of the successful formation of nanocomposites. Notably, the nearly complete quenching of the emission of nanocomposites relative to the pristine P3HT homopolymer was observed, indicating the efficient charge transfer.

The photovoltaic devices consisting of ITO/PEDOT:PSS/P3HT-CdSe NR/Al configuration were fabricated using P3HT-CdSe NR nanocomposites prepared by click coupling of ethynyl-terminated P3HT with  $N_3CH_2$ -BA-functionalized CdSe NRs in photoactive layer. PEDOT:PSS coated ITO substrate and Al electrode were used as cathode and anode to extract holes and electrons, respectively. The entire solar cell fabrication was conducted under an inert argon atmosphere to prevent undesired oxidation or degradation. For photoactive layer preparation, a spin-casting method was used as as-synthesized P3HT grafted CdSe NRs are expected to form a film with intrinsic nanoscale donor-acceptor integrated structure while keeping excellent dispersion of CdSe NRs in P3HT due to the advantageous properties of P3HT-CdSe NR nanocomposites. The focus of our work in this thesis is to produce nanocomposites which are suitable for solution processable manufacturing of solar cells. First, the weight ratio between CdSe NRs and P3HT was optimized. P3HT-CdSe NR nanocomposites with the weight ratio of CdSe NRs of 50wt%, 70wt%, 80wt%, and 90wt% were prepared. It should be noted that the amount of  $N_3CH_2$ -BA molecules capped on CdSe NR surface was enough to render all the coupling of P3HT at the weight ratio of 50wt%. **Figure 3.10** displays the current density ( $J$ ) versus voltage ( $V$ ) characteristics of the hybrid solar cells based on P3HT-

CdSe NR nanocomposites with the CdSe NR weight ratio of 50wt%, 70wt%, 80wt%, and 90wt%. The devices fabricated with 80wt% of CdSe NRs exhibited the highest power conversion efficiency (PCE) of 0.012 % with a short circuit current density ( $J_{sc}$ ) of 0.079 mA/cm<sup>2</sup>, an open circuit voltage ( $V_{oc}$ ) of 0.433 V, and a fill factor ( $FF$ ) of 33. As the



	CdSe NRs 50 wt%	CdSe NRs 70 wt%	CdSe NRs 80 wt%	CdSe NRs 90 wt%	
$V_{oc}$	0.538	0.521	0.453	0.332	V
$J_{sc}$	0.022	0.059	0.079	0.042	mA/cm <sup>2</sup>
$FF$	0.585	0.343	0.330	0.443	
$PCE$	0.007	0.011	0.012	0.006	%

**Figure 3.10.** Current-voltage characteristics of the hybrid solar cell devices fabricated with P3HT-CdSe NR nanocomposites at different weight ratios.

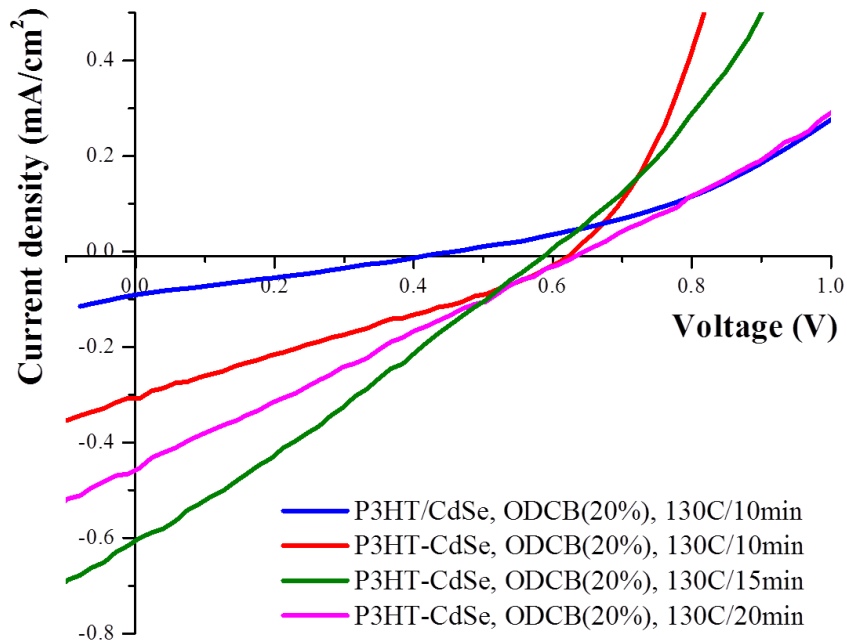
amount of CdSe NRs increased (i.e., up to 80wt%), it showed the improved PCE and  $J_{sc}$ , which was possibly due to the enhanced electron transport as the electron hopping procedure was facilitated at the high fraction of electron donors (i.e., CdSe NRs). However, the PCE and  $J_{sc}$  decreased in case of devices with 90 CdSe NRs wt%, which

can be attributed to the agglomeration of CdSe NRs in P3HT matrix as the number of P3HT chains was not enough to render good dispersion of CdSe NRs in the polymer matrix.

The performance of hybrid cells with P3HT/CdSe NRs physically blended and hybrid cells with P3HT-CdSe NR nanocomposites was compared and shown in **Figure 3.11**. Specifically, 80wt% of N<sub>3</sub>-CH<sub>2</sub>-BA-capped CdSe NRs were blended with P3HT in chloroform/ODCB (20 volume% of ODCB) by vortex mixing, to yield CdSe NRs (80wt%)/P3HT simple physical mixture solution. Subsequently, devices using the P3HT/CdSe NRs solution and P3HT-CdSe NR nanocomposites (80 CdSe NR wt%) were fabricated. It is noteworthy that the use of high boiling point solvent led to significantly improved mobility of P3HT film due to their highly self-ordered microcrystalline structure formed during the retarded solvent evaporation. Moreover, thermal annealing process (130 °C/15 min) was followed to further enhance the crystallinity of P3HT. The PCE of devices with physical blending of CdSe NRs/P3HT was 0.012 % with a  $V_{oc}$  of 0.453 V, a  $J_{sc}$  of 0.079 mA/cm<sup>2</sup>, and a  $FF$  of 33.0. Notably, the improved PCE of 0.0536 % ( $V_{oc}$ =0.641 V,  $J_{sc}$ =0.307 mA/cm<sup>2</sup>, and  $FF$ =27.2) at the same fabrication condition can be achieved probably because of improved contact between P3HT and CdSe NRs as reported from previous work done by our group. In order to achieve high hole mobility of the P3HT film by forming their crystalline structure, the annealing condition was optimized. Prepared hybrid cells with P3HT-CdSe NR nanocomposites were annealed at 130 °C for 10 min, 15 min, and 20 min, respectively. The highest PCE of 0.0975% with a  $V_{oc}$  of 0.596 V, a  $J_{sc}$  of 0.601 mA/cm<sup>2</sup>, and a  $FF$  of 27.3 was obtained with the annealing condition of 130 °C for 15 min. However, prolong annealing (i.e., 20 min) resulted in

reduced PCE of 0.0743% ( $V_{oc}=0.645$  V,  $J_{sc}=0.453$  mA/cm<sup>2</sup>, and  $FF=25.5$ ) which was due possibly to the degradation of P3HT films.

Despite of the promoted electronic interaction between CdSe NRs and P3HT, and improved dispersion of CdSe NRs in P3HT film of as-synthesized P3HT-CdSe NR nanocomposites, the device performance was not satisfactory when compared with



Thermal annealing	P3HT/CdSe NR Simple blending		P3HT-CdSe NR nanocomposites		V
	130°C/10min	130°C/10min	130°C/15min	130°C/20min	
$V_{oc}$	0.453	0.641	0.596	0.645	
$J_{sc}$	0.079	0.307	0.601	0.453	mA/cm <sup>2</sup>
FF	33.0	27.2	27.3	25.5	
PCE	0.012	0.0536	0.0975	0.0743	%

**Figure 3.11.** Current-voltage measurement of the hybrid solar cell devices fabricated with P3HT/CdSe NR physical mixture and P3HT-CdSe NR nanocomposites. Thermal annealing condition was controlled (i.e., 130 °C/10min, 130 °C/15min, and 130 °C/20min).

previous literature (PCE= ~2%). Hence, we hypothesized that the existence of alkyl ligands (i.e., TDPA) or  $N_3-CH_2-BA$  was the main obstacle for achieving excellent device performance. Hence, the experiment was designed to investigate the influence of

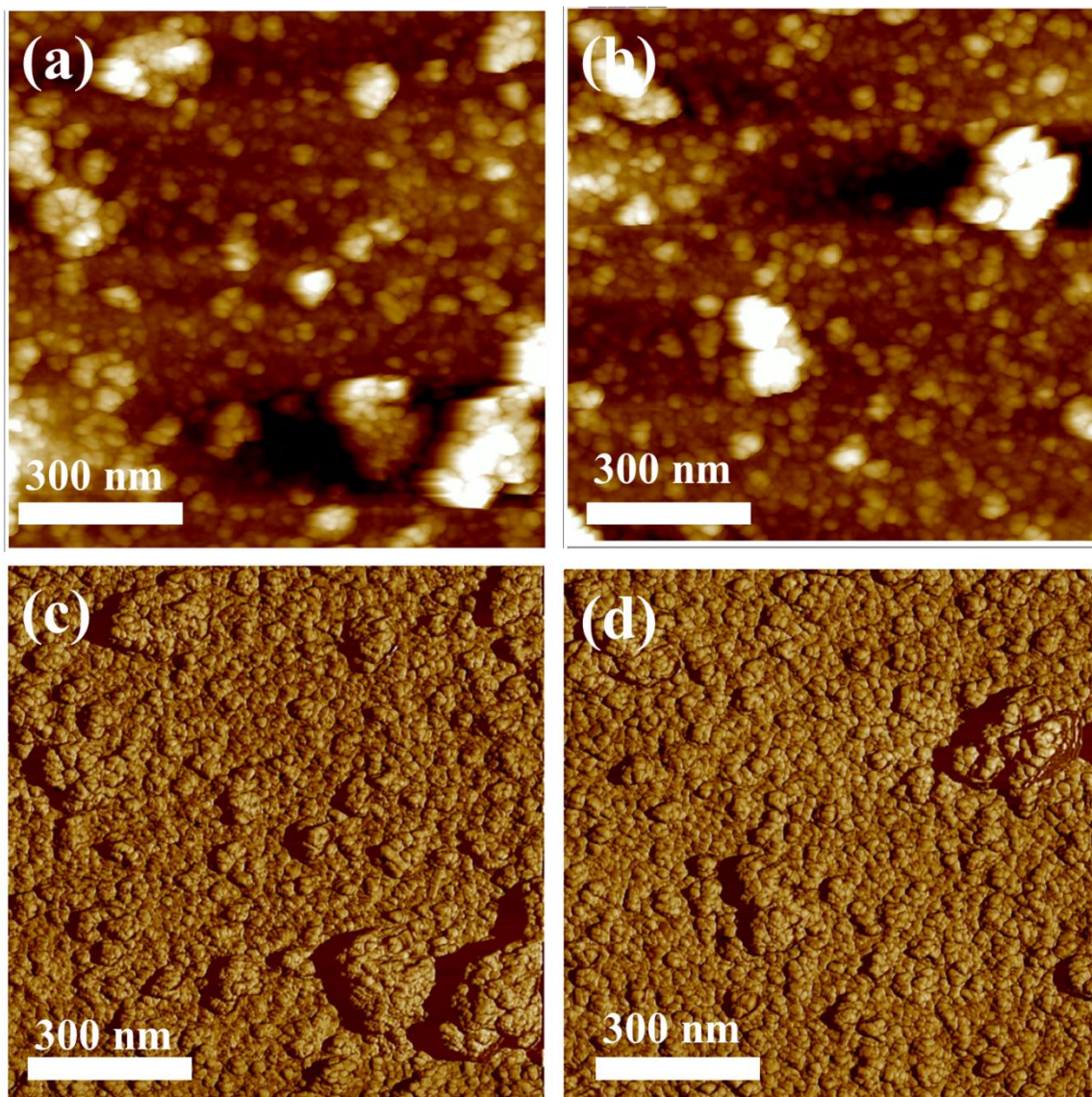


**Figure 3.12.** AFM measurement on P3HT-CdSe NR nanocomposite films. (a,c) Tapping mode AFM height image and its corresponding phase image of P3HT-CdSe NR hybrid film without methanol treatment. (c,d) Tapping mode AFM height image and its corresponding phase image of P3HT-CdSe NR hybrid film after methanol treatment. z-scale is 100 nm.

extra tetradecylphosphonic acid ligands or  $N_3\text{-CH}_2\text{-BA}$  on the device power conversion efficiency. Specifically, the devices fabricated using P3HT-CdSe NR nanocomposites were immersed in methanol solution to remove excess ligands (i.e., tetradecyl phosphonic acid or  $N_3\text{-CH}_2\text{-BA}$ ). **Figure 3.12** shows the atomic force microscopy (AFM) height and phase images of P3HT-CdSe NR nanocomposites film before and after methanol treatment. The hybrid layer showed no noticeable change in the surface topology and the root-mean square surface roughness, which remained at  $\sim 35\text{nm}$ . However, the PCE

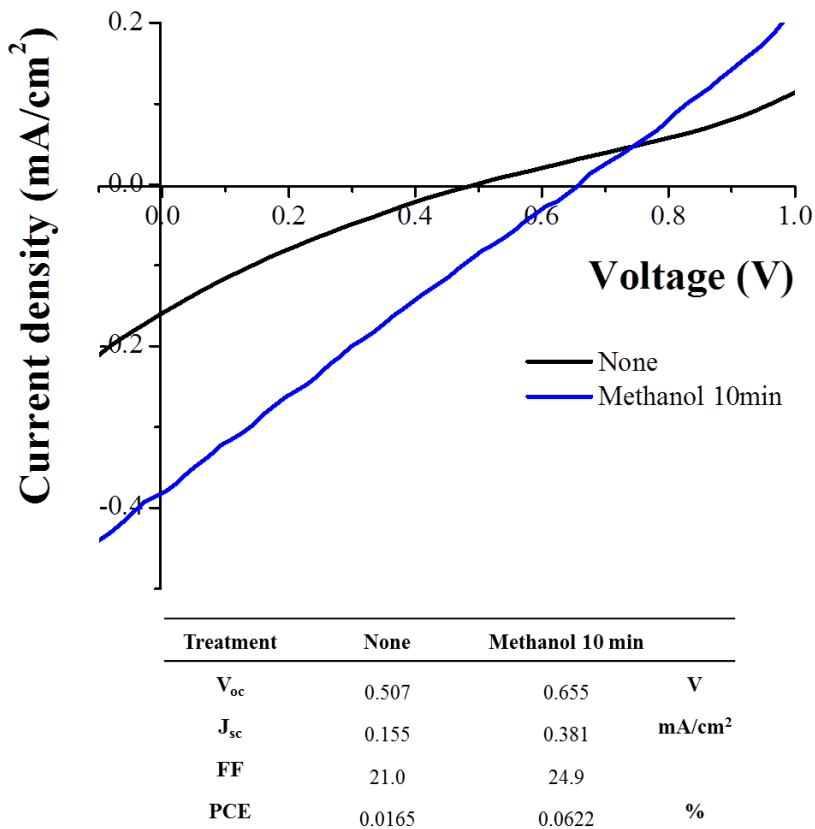


**Figure 3.13.** Current-voltage curves of the P3HT-CdSe NR hybrid solar cells with and without immersion of as-prepared P3HT-CdSe NR films in methanol.

improved from 0.0165 % to 0.0622 % after methanol treatment as shown in **Figure 3.13**, which can be attributed to the result of removal of excess tetradecyl phosphonic acid or 4-azidomethylbenzoic acid through methanol treatment. This observation strongly suggested that the detrimental influence of fatty insulating ligands on the electron transport in the devices.

### 3.4. Conclusion

In this study, we have successfully crafted P3HT-CdSe NR nanocomposites via click chemistry between ethynyl group in P3HT and azide moiety in functionalized CdSe NRs, dispensing with need for ligand exchange process, by utilizing bifunctional ligands during the synthesis of CdSe NCs. The influence of the type of anchoring group, the ratio between aliphatic ligands and aryl ligands, and the length of alkyl chain of aliphatic ligands on the shape of CdSe NCs was investigated to provide guidelines for the optimization of CdSe NRs shape for a variety of future applications but not limited to photovoltaics. These parameters had a significant impact on the shape evolution of CdSe NCs.

The grafting of ethynyl terminated P3HT with azide functionalized CdSe NRs were successful as confirmed by FTIR and  $^1\text{H}$  NMR. The complete disappearance of ethynyl peak and the weakened absorption of azide characterization peak clearly demonstrated the occurrence of coupling. Moreover, the weakened azide peak obviously suggested that the amount of  $\text{N}_3\text{CH}_2\text{-BA}$  molecules on the CdSe NR surface was enough to enable complete grafting of ethynyl-terminated P3HT.

We have also fabricated photovoltaic devices utilizing P3HT-CdSe NR

nanocomposites. The effect of weight ratio and annealing condition on the device performance was studied. Despite of the optimization of fabrication condition, the performance of resulting devices fabricated using our P3HT-CdS NR nanocomposites was rather low compared with other reports. From the correlation between the time for elimination of excess ligands and the device performance, it was speculated that excess ligands which is inevitable in the synthesis CdSe NCs with desired shape played significant role in electronic behavior of the resulting photoactive film. Nonetheless, this novel yet robust method for crafting CP-NC nanocomposites may offer opportunities in other optoelectronic applications including LEDs, lasers, and bio-imaging.

## 4. Semiconducting conjugated polymer grafted CdTe tetrapods nanocomposites

Reproduced with permission from Jaehan Jung, Xinchang Pang, Chaowei Feng, and Zhiqun Lin, “*Semiconducting Conjugated Polymer-inorganic Tetrapods Nanocomposites*”, *Langmuir*, 2013, 29, 8086, Copyright 2013 American Chemical Society.

### 4.1. Introduction

In comparison to quantum dots (QDs) in which hopping transport occurs, and nanorods (NRs) where the alignment of NRs perpendicular to the substrate may be necessary to realize the full potential of high electron mobility in QDs and NRs, tetrapods enable more effective charge transport due to their intrinsically three-dimensional structures. CdTe is an appealing inorganic semiconductor for inorganic solar cells due to its optimum band gap energy ( $E_g = 1.45$  eV) and high absorption coefficient ( $\alpha = 10^4$  cm<sup>-1</sup>),<sup>4</sup> thereby improving the light harvesting efficiency by extending into the near-infrared (NIR) range. Clearly, the replacement of CdSe with CdTe renders the absorption of higher amount of solar radiation as CdSe only absorbs the UV and visible photons (i.e., higher band gap). Additionally, CdTe possesses a much higher electron mobility than CdSe.<sup>4</sup>

Herein, we report a robust strategy to place P3HT onto the surface of CdTe tetrapods in the absence of ligand exchange. CdTe tetrapods carry great advantages over CdSe QDs (or QRs) for use in solar cells due to the largely reduced recombination of

electrons and holes, while retaining their large interfacial area.<sup>73, 83</sup> This can be attributed to their three-dimensional structure (four arms symmetrically emanating from the central core), which enables continuous charge transport pathway in the thin film regardless of their orientation.<sup>1</sup> The catalyst-free click reaction was employed to yield P3HT–CdTe tetrapod nanocomposites. First, CdTe tetrapods were synthesized by utilizing a bifunctional ligand (i.e., 4-bromobenzyl phosphonic acid (BBPA) with phosphonic acid and aryl bromide at each end). The aryl bromide groups of BBPA were then transformed into azide groups, forming N<sub>3</sub>-functionalized CdTe tetrapods. Finally, ethynyl-terminated P3HT synthesized by a quasi-living Grignard metathesis (GRIM) method was grafted onto N<sub>3</sub>-functionalized CdTe tetrapods through a catalyst-free alkyne-azide cycloaddition, yielding intimate P3HT–CdTe tetrapod nanocomposites without introducing any metallic impurities, which could be detrimental to the photovoltaic device performance. The success of click reaction was confirmed by Fourier transform infrared spectroscopy (FTIR) and nuclear magnetic resonance spectroscopy (NMR). The number of P3HT chains tethered on the CdTe tetrapod surface was estimated by thermogravimetric analysis (TGA). The absorption and photoluminescence measurements suggested the intimate contact between P3HT and CdTe tetrapods. A nearly complete quench of P3HT emission in P3HT–CdTe tetrapod nanocomposites was indicative of the efficient charge transfer from electron-donating P3HT onto electron-accepting CdTe tetrapods.

## 4.2. Experimental

All chemicals, including 4-bromobenzyl bromide, triethyl phosphite, cadmium oxide, tri-n-octylphosphine (TOP, 90%), tellurium powder, sodium azide, 2,5-dibromo-3-

hexylthiophene, Ni(dppp)Cl<sub>2</sub>, tert-butylmagnesium chloride (2mol/L in diethyl ether), and ethynylmagnesium bromide (0.5 mol/L in THF) from Sigma Aldrich, octadecyl phosphonic acid (ODPA, 97%) from Alfa Aesar, and tri-n-octylphosphine oxide (TOPO, 90%) from Strem chemicals were used as received. THF (Fisher, 99%) was refluxed over sodium wire and distilled from sodium naphthalenide solution.

**Synthesis of bromobenzylphosphonic acid (BBPA):** 4-bromobenzyl bromide and triethyl phosphite at 1:2 molar ratio were heated under Ar at 150°C for 5 h, yielding diethylphosphonate ester. The excess triethyl phosphite and byproducts were removed by rotary evaporator at 100°C for several hours. Diethylphosphonate ester was hydrolyzed with concentrated aqueous HCl by heating at 100°C overnight, yielding bromobenzylphosphonic acid (BBPA). After cooling to room temperature, BBPA was filtered out, redissolved in acetonitrile, and finally recrystallized in ethyl acetate.

**Synthesis of BBPA-capped CdTe nanocrystals (NCs):** BBPA-capped CdTe NCs were synthesized by modifying the reported method for CdTe NCs.<sup>84</sup> In all experiments, the molar ratio of cadmium to phosphonic acid ligands (i.e., ODPA and BBPA) was set to 1:1.8 while the BBPA/ODPA ratio was changed. A mixture of CdO (0.5 mmol), ODPA, BBPA, and TOPO (2 g) were degassed in a three-neck flask for 1 h at 120°C before increasing the temperature under Ar to above 300°C, at which the solution turned clear and colorless. Subsequently, 0.2 M Tellurium/trioctylphosphine (Te TOP) solution was prepared in the glove box. The temperature was decreased to 300°C, and 0.5 ml Te TOP solution was rapidly injected to initiate the nucleation and growth. In addition to the single injection method as noted above, 0.1 ml of 0.2M Te TOP solution was injected 10

times at the interval of 1 min (i.e., multiple injection method) to prepare CdTe tetrapod with longer arms. CdTe NCs were allowed to grow at 300°C for 10 min. The heating mantle was then removed to stop reaction. After the solution was cooled to 60°C, 2ml THF was added. The resulting BBPA-capped CdTe NCs were precipitated twice with methanol and dissolved in THF.

***Synthesis of ethynyl-terminated P3HT:*** Ethynyl-terminated P3HT (i.e., P3HT–≡) was synthesized by a quasi-living Grignard metathesis (GRIM) method.<sup>85</sup> Briefly, 2,5-dibromo-3-hexylthiophene (0.815g, 2.5 mmol) was dissolved in THF (5ml) in a three-neck flask and stirred under Ar. Tert-butyilmagnesium chloride (1.25ml, 2.5mmol) was added. The mixture was stirred for 2 h at room temperature. Subsequently, it was diluted to 25mL with THF, followed by the addition of Ni(dppp)Cl<sub>2</sub> (11.2 mg, 0.020 mmol). The resulting solution was stirred for 30 min at room temperature, producing intermediate P3HT; it was then reacted with ethynylmagnesium bromide (2ml, 1mmol) in THF for 30 min. The product, P3HT–≡, was obtained by precipitating the reaction mixture in methanol, filtering in an extraction thimble, and washing by Soxhlet extraction with methanol, hexane, and chloroform sequentially. It was recovered after chloroform evaporated. The regioregularity of P3HT was greater than 97%, as determined by <sup>1</sup>H NMR. The number average molecular weight and polydispersity index (PDI) of P3HT were 50kDa and 2.2, respectively, as measured by gel permeation chromatography (GPC). Yield: 41.2 %

***Synthesis of P3HT–CdTe tetrapod nanocomposites by click reaction:*** Sodium azide (NaN<sub>3</sub>) was added to BBPA-capped CdTe tetrapods THF solution. The mixture was

then sealed and stirred at room temperature for three days. Excess amount of  $\text{NaN}_3$  was removed by centrifugation. The resulting azide-benzylphosphonic acid-capped CdTe tetrapods ( $\text{CdTe-N}_3$ ) were then precipitated with methanol. Subsequently, 50 mg P3HT-≡ and 50 mg  $\text{CdTe-N}_3$  tetrapod were mixed in 10 ml THF and kept at  $65^\circ\text{C}$  under Ar for two days. The final product (i.e., P3HT-CdTe nanocomposites) was cooled to room temperature and diluted 10 times with THF. The resulting solution was precipitated with methanol twice to remove free P3HT which was not coupled with CdTe tetrapods.

**Characterization:** The morphology of CdTe NCs and P3HT-CdTe tetrapod nanocomposites were imaged by low-resolution and high-resolution transmission electron microscope (JEOL 100cx and Tecnai F30). The  $^1\text{H}$  NMR spectra were taken using a Varian VXR-400 spectrometer. The grafting density of P3HT chains on the CdTe tetrapod surface was determined by thermogravimetry analysis (TGA; TA Instrument TGA Q50) in nitrogen atmosphere. The temperature was increased to  $800^\circ\text{C}$  at the rate of  $5^\circ\text{C}/\text{min}$ . The absorption and emission spectra were recorded with a UV-Vis spectrometer (UV-2600, Shimadzu) and a spectrofluorophotometer (RF-5301PC, Shimadzu), respectively. All samples were excited at  $\lambda_{\text{ex}} = 445 \text{ nm}$  and the emission were collected at  $\lambda_{\text{em}} > 500 \text{ nm}$ .

### 4.3. Results and discussion

CdTe NCs functionalized with bifunctional ligands were synthesized in the absence of ligand-exchange procedure. 4-bromobenzyl phosphonic acid (BBPA) was employed as bifunctional ligands as phosphonic acids are the most widely used as ligands

and they are powerful additive to control the branching and anisotropic growth.<sup>84</sup> The effect of molar ratio of BBPA to octadecyl phosphonic acid (ODPA) on the shape of the resulting CdTe NCs was studied. As shown in **Figure 4.1a**, BBPA-functionalized CdTe QDs were produced at the BBPA/ODPA ratio of 1:7. As the ratio increased to 1:5, the anisotropic NCs including rods, dipods, and tripods were obtained (**Figure 4.1b**). More regular CdTe tetrapods were yielded at the BBPA/ODPA ratio of 1:4 (**Figure 4.1c**), which was due to the influence of small molecules (i.e., ligands) that triggered the twinning as well as anisotropic growth.<sup>84</sup> Clearly, the higher the BBPA/ODPA ratio, the more branched and elongated CdTe NCs were observed (**Figures 4.1a-c**). In order to extend the length of each arm, the multiple injection method (i.e., 10 times in the present study) was used by simple replenishing Te (i.e., Te TOP solution) to the reaction solution at certain time interval.<sup>45, 86</sup> **Figure 4.1d** shows the TEM micrograph of CdTe tetrapods with the increased size and aspect ratio as compared to those obtained from the single injection method (**Figure 4.1c**).

The BBPA-functionalized CdTe tetrapods prepared by the multiple injection method (**Figure 4.1d**) were then utilized to synthesize P3HT–CdTe tetrapod nanocomposites as these tetrapods have advantageous size and shape for use in hybrid solar cells as compared to other structures in **Figures 4.1a-c**. Given the typical thickness of hybrid solar cells ranging from 70 to 200 nm, the intrinsic three-dimensional structures of CdTe tetrapods are beneficial for efficient charge transport to the electrode in comparison to the corresponding QDs where electron hopping between particles would be required. The high-resolution TEM images revealed that CdTe tetrapods were  $85 \pm 10$  nm in size with a diameter of  $5 \pm 0.3$  nm for each arm. The HRTEM image clearly showed

the tetrapod morphology of CdTe NCs (**Figure 4.2b**). Interestingly, planar defects were observed in some arms of CdTe tetrapods (the inset in **Figure 4.2b**), which may be due to the effect of short ligand (i.e., BBPA).<sup>84</sup> The formation of tetrapods can be rationalized according to the multiple-twin model.<sup>84</sup> In multiple-twin model the arms grow from an

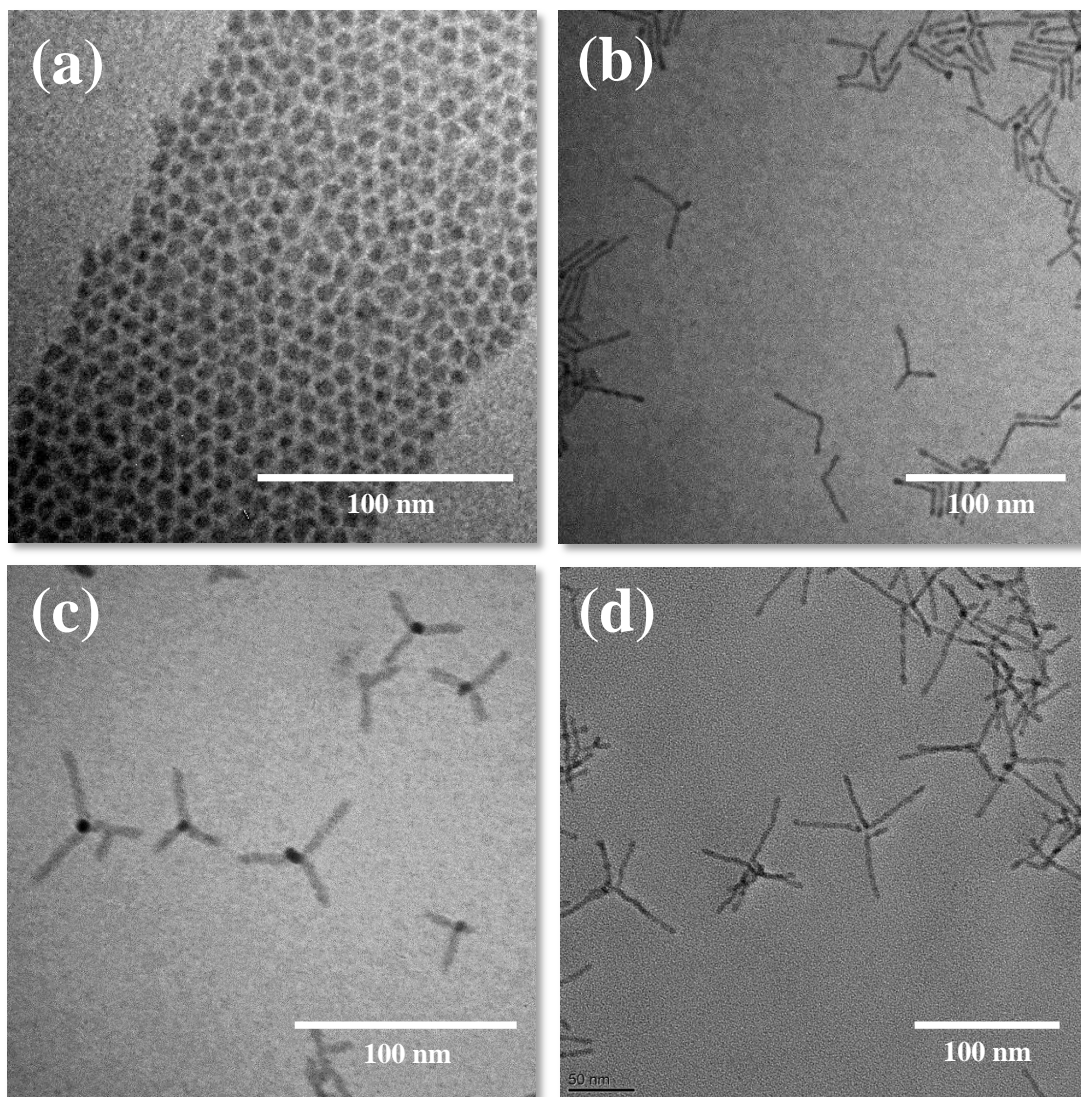


**Figure 4.1.** Low-magnification TEM images of CdTe NCs at different molar ratio of BBPA to ODPA. (a) BBPA : ODPA = 1:7, (b) BBPA : ODPA = 1:5, and (c) BBPA : ODPA = 1:4 by single injection of Te TOP solution, and (d) BBPA : ODPA = 1:4 by multiple injections of Te TOP solution.

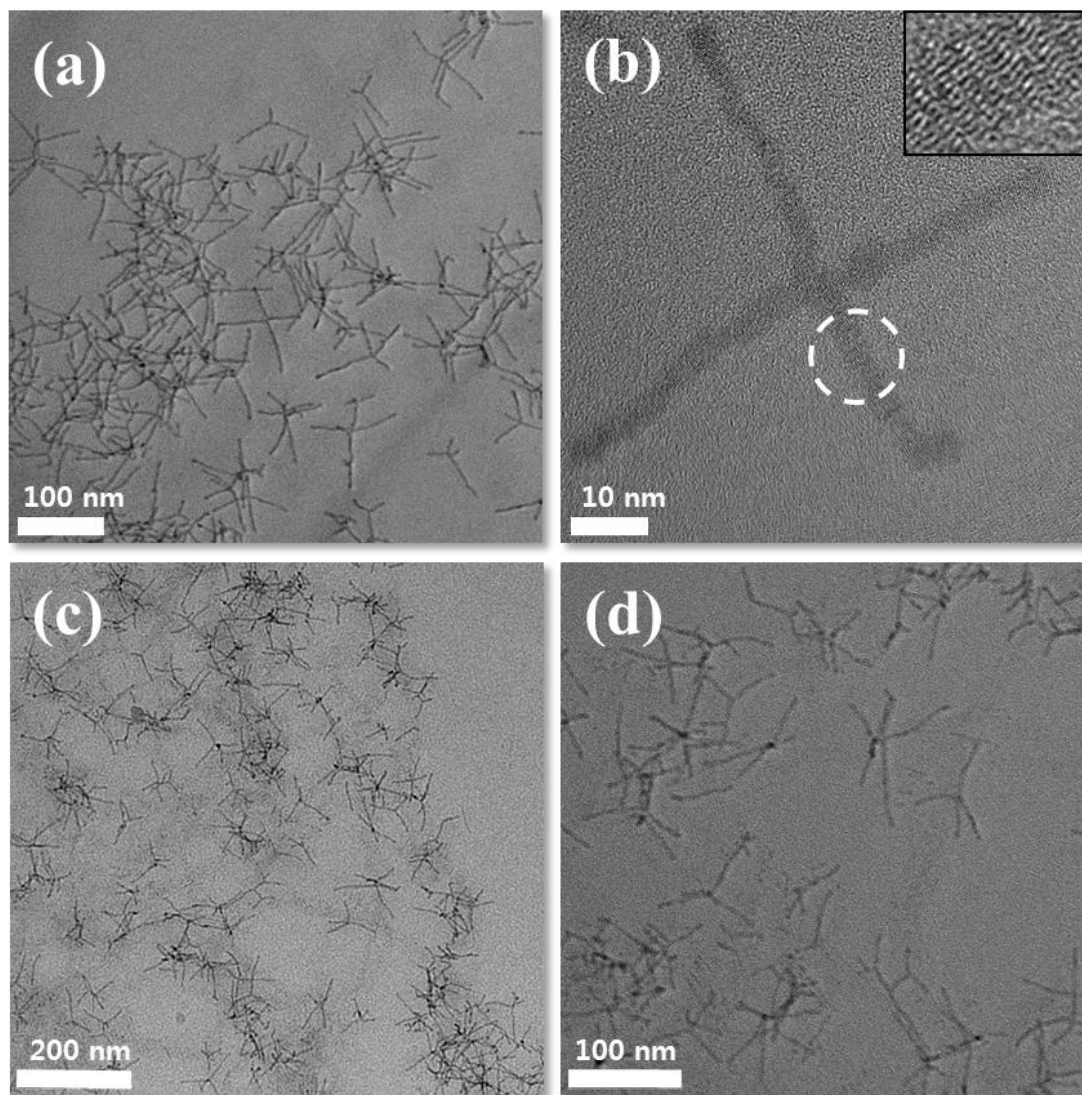
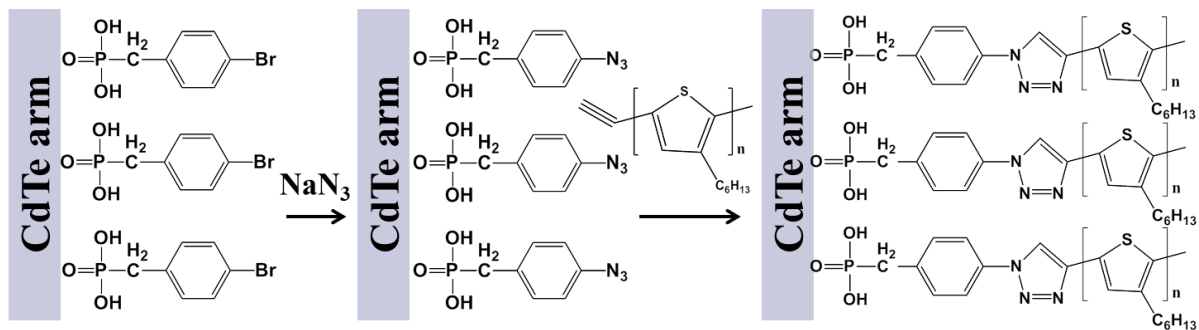


**Figure 4.2.** TEM images of (a) BBPA-functionalized CdTe tetrapods; (b) close-up of individual BBPA-functionalized CdTe tetrapod, the close-up of arm marked with a dashed circle is shown as inset; and (c & d) P3HT–CdTe tetrapod nanocomposites.

octahedral twinned wurtzite core, thus the number of arms depend on the types of twins in the core, which yield a distribution of the number of arms. The coexistence of rods, dipods, tripods, and tetrapods in **Figure 4.1 and 4.2** suggested that tetrapods were grown from twinned wurtzite core. After CdO was decomposed by phosphonic acid, Cd-

phosphonic acid complex (i.e., Cd-BBPA and Cd-ODPA was formed as  $\text{Cd}^{2+}$  readily reacted with phosphonates. Cd-BBPA complex was much more mobile than the bulkier Cd-ODPA. As a result, the probability of yielding planar defects (i.e., twins) was increased in the presence of BBPA; this led to the formation of twinned core, and was responsible for the emergence of rods, dipods, tripods, and tetrapods.

The P3HT–CdTe tetrapod nanocomposites were subsequently synthesized via click reaction between ethynyl-terminated P3HT (i.e., P3HT–≡) and azide-functionalized CdTe (i.e., CdTe– $\text{N}_3$ ) tetrapods after converting aryl bromine groups in BBPA-functionalized CdTe tetrapods into azide groups as illustrated in **Scheme 4.1**. **Figures 4.2c & 4.2d** showed the TEM images of P3HT–CdTe tetrapod nanocomposites, where CdTe tetrapods were well dispersed in the nanocomposites. The success of grafting P3HT–≡ chains onto CdTe– $\text{N}_3$  tetrapods was confirmed by the Fourier transform infrared (FT-IR) spectroscopy measurements as shown in **Figure 4.3**. Strong absorption of P3HT at  $2954\text{ cm}^{-1}$ ,  $2915\text{ cm}^{-1}$ , and  $2850\text{ cm}^{-1}$  were assigned to the asymmetric C-H stretching vibrations in  $-\text{CH}_3$ ,  $-\text{CH}_2$ , and the symmetric C-H stretching vibration in  $-\text{CH}_2$ , respectively,<sup>87</sup> from the alkyl side chains in P3HT and ligands. Notably, the characteristic  $-\text{N}_3$  vibration was appeared at  $2040\text{ cm}^{-1}$  after the aryl bromine groups of BBPA-functionalized CdTe tetrapods were converted into azide groups, forming CdTe– $\text{N}_3$  tetrapods. This peak was then disappeared after the CdTe– $\text{N}_3$  tetrapods coupled with P3HT–≡, suggesting the successful grafting of P3HT chains onto the CdTe tetrapods (i.e., producing P3HT–CdTe tetrapod nanocomposites; **Figure 4.3**) via 1,3-dipolar cycloaddition between ethynyl group in P3HT–≡ and azide group in CdTe– $\text{N}_3$  tetrapods.



**Scheme 4.1.** Grafting ethynyl-terminated P3HT (i.e., P3HT≡) onto azide-functionalized CdTe (i.e., CdTe-N<sub>3</sub>) tetrapods by catalyst-free click chemistry, yielding P3HT-CdTe tetrapod nanocomposites.

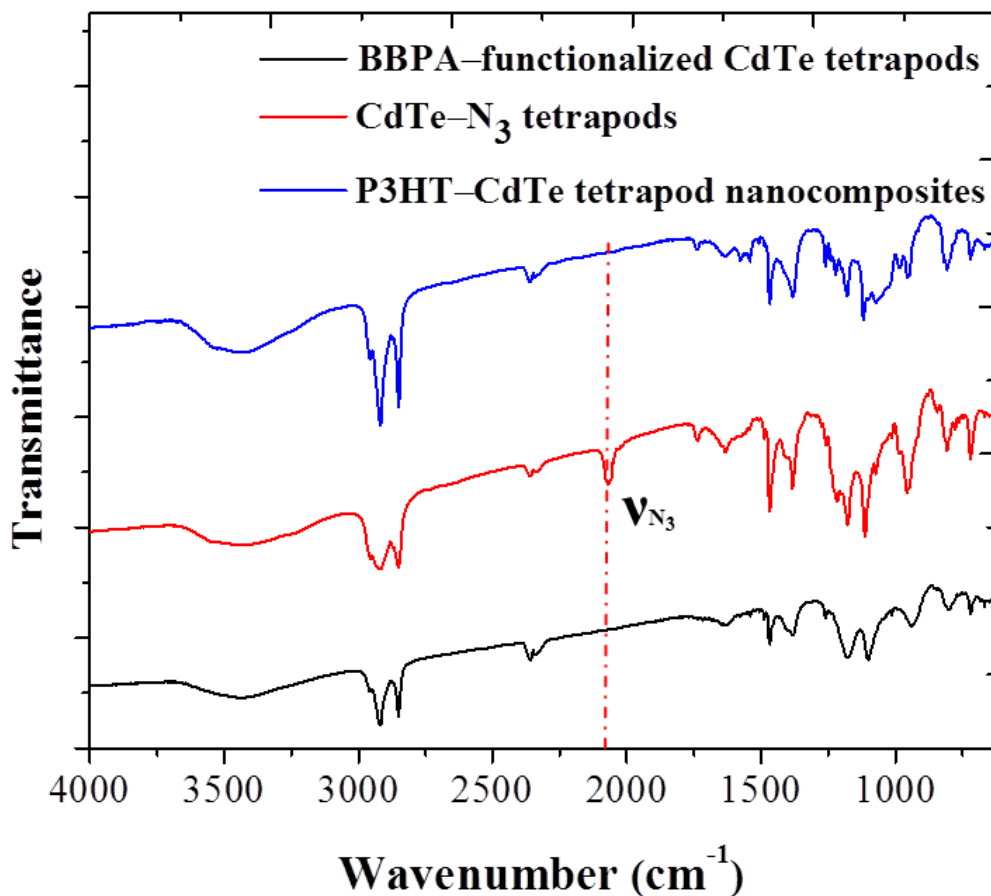


**Figure 4.3.** FTIR spectra of BBPA-functionalized CdTe tetrapods (black), azide-functionalized CdTe tetrapods (i.e., CdTe-N<sub>3</sub> tetrapods; red), and P3HT-CdTe tetrapod nanocomposites (blue).

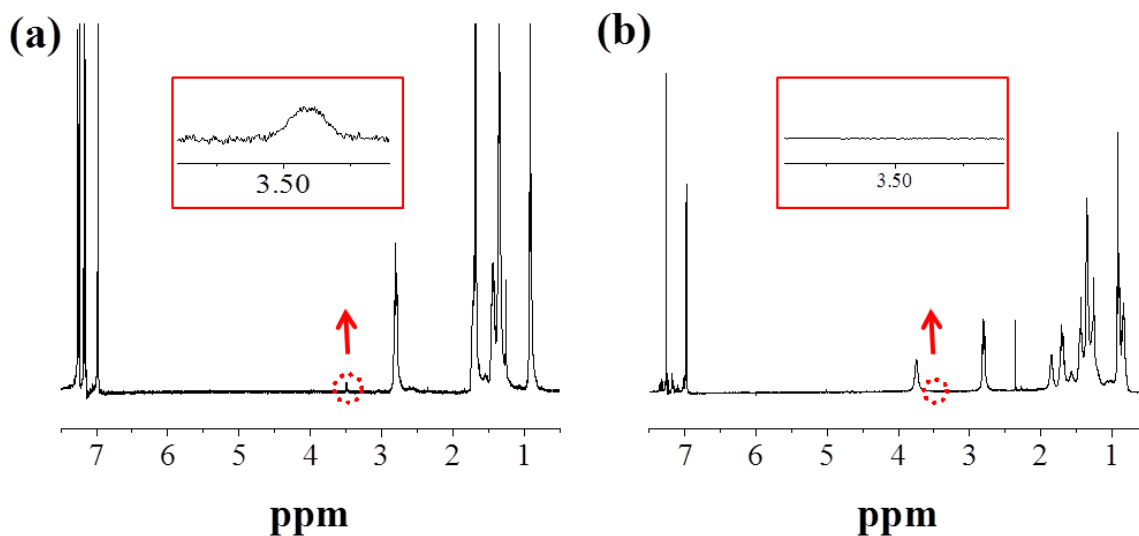


**Figure 4.4.**  $^1\text{H}$  NMR spectra of (a) ethynyl-terminated P3HT (i.e., P3HT $\equiv$ ), and (b) P3HT-CdTe tetrapod nanocomposites. The peak between 3.5 and 4 ppm in (b) was assigned to the proton of  $-\text{CH}_2-$  from CdTe-BPA- $\text{N}_3$  tetrapods after grafting of CdTe-BPA- $\text{N}_3$  tetrapods (i.e., CdTe- $\text{N}_3$  tetrapods) onto P3HT $\equiv$ .

It is worth noting that such coupling reaction was conducted in the absence of catalysts, thus circumventing the introduction of any metallic impurities, which may influence the performance of the P3HT-CdTe-tetrapod-based photovoltaic devices. The  $^1\text{H}$  NMR data shown in **Figure 4.4** also strongly supported the occurrence of grafting P3HT $\equiv$  onto CdTe- $\text{N}_3$  tetrapods. A proton signal at 3.5 ppm from the ethynyl group on the P3HT chain (**Figure 4.4a**) was disappeared in P3HT-CdTe tetrapod nanocomposites (**Figure 4.4b**) after P3HT $\equiv$  chain was coupled with CdTe- $\text{N}_3$  tetrapod.

To determine the coverage of P3HT chains on the CdTe tetrapod surface, thermogravimetric analysis (TGA) was performed (**Figure 4.5**). BBPA-functionalized CdTe tetrapods showed a significant mass loss from 300°C to 450°C due to the

degradation of surface capping ligands (i.e., BBPA and ODPa), which was about 26% of BBPA-functionalized CdTe tetrapods (**Figure 4.5a**). TGA curve of ethynyl-terminated P3HT homopolymer (i.e., P3HT-≡) (molecular weight = 50kDa) also revealed the onset of degradation in the temperature range of 400-450°C, leaving behind a char-like yield of 28% (**Figure 4.5b**). The mass reduction in P3HT-CdTe tetrapod nanocomposites (i.e., the sum of grafted P3HT and ligands) in this temperature range was roughly 60% (**Figure 4.5c**). Taken together, the weight ratio of P3HT to CdTe tetrapods was about 3.82:1. Based on the TEM images in **Figure 4.2**, the molecular weight of CdTe tetrapods was estimated to be  $1.11 \times 10^7$  g/mol. Thus, the molar ratio of P3HT chains to CdTe tetrapods was estimated to be approximately 800:1.

The photophysical properties of P3HT-CdTe tetrapod nanocomposites were explored by UV-vis absorbance and photoluminescence (PL) studies. The absorption spectra of ethynyl-terminated P3HT (i.e., P3HT-≡), BBPA-functionalized CdTe tetrapods, and P3HT-CdTe tetrapod nanocomposites in THF are shown in **Figure 4.6a**. The

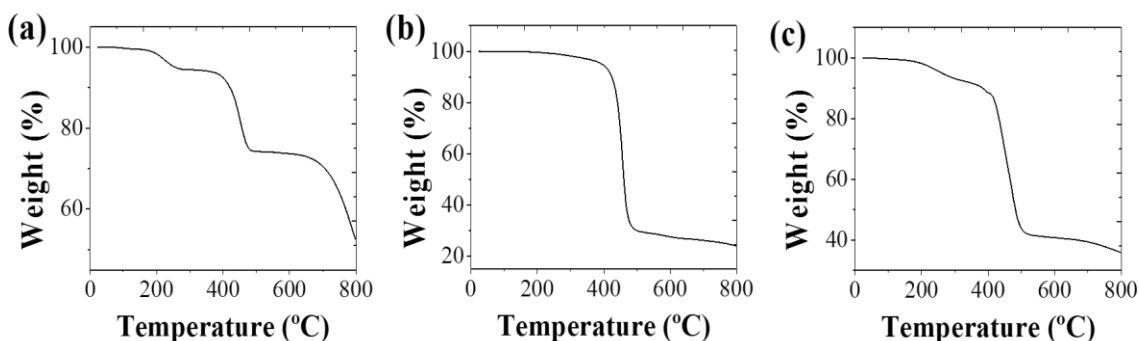


**Figure 4.5.** Thermogravimetry analysis (TGA) of (a) BBPA-functionalized CdTe tetrapods, (b) ethynyl-terminated P3HT homopolymer, and (c) P3HT-CdTe tetrapod nanocomposites prepared by click reaction.

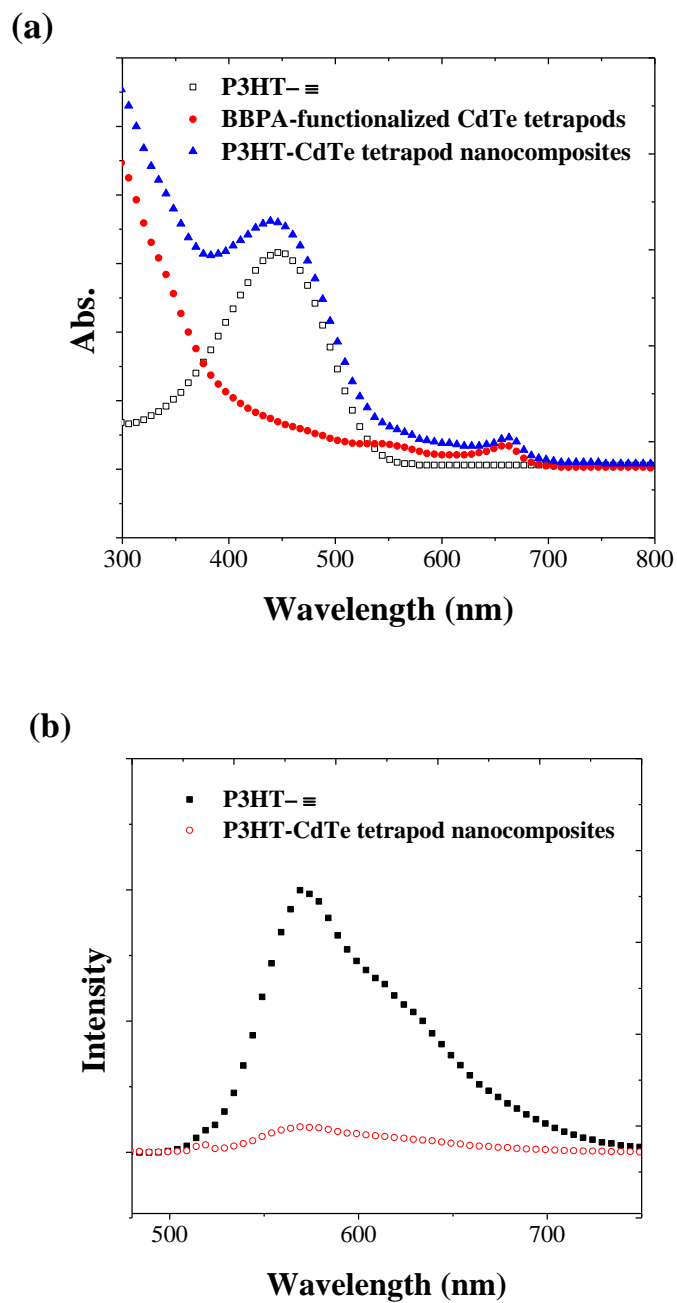


**Figure 4.6.** (a) Absorption spectra of ethynyl-terminated P3HT (black square), BBPA-functionalized CdTe tetrapods (red circle), and P3HT-CdTe tetrapod nanocomposites (blue triangle) prepared by click chemistry. (b) Emission spectra of ethynyl-terminated P3HT (black square) and P3HT-CdTe tetrapod nanocomposites (red circle).

absorption maxima for P3HT and CdTe tetrapods were at 445 nm and 657 nm, respectively. Clearly, the absorption spectrum of nanocomposites was simply a sum of their constituents (i.e., two maxima in nanocomposites at 445 nm and 657 nm can be ascribed to P3HT and CdTe tetrapod, respectively), suggesting the successful coupling of end-functionalized P3HT and CdTe tetrapods. **Figure 4.6b** shows the PL spectra of P3HT-≡ and P3HT-CdTe tetrapod nanocomposites in THF. Obviously, the nearly complete quenching of the emission of nanocomposites relative to the pristine P3HT homopolymer indicated the efficient charge transfer from electron-donating P3HT onto electron-accepting CdTe tetrapods. This observation further confirmed the intimate chemical contact between P3HT and CdTe tetrapods.

#### 4.4. Conclusions

In summary, CdTe tetrapods were synthesized by multiple injections of the Te precursor. A simple strategy for semiconducting P3HT-CdTe tetrapod nanocomposites was then explored by anchoring ethynyl-terminated P3HT onto azide-functionalized CdTe tetrapods via a catalyst-free click chemistry. The direct contact between P3HT and CdTe tetrapod enabled the good dispersion of CdTe tetrapods in nanocomposites. The success of click reaction was confirmed by FTIR and <sup>1</sup>H NMR measurements. The molar ratio of P3HT chains to CdTe tetrapods was approximately 460:1. The absorption spectrum of P3HT-CdTe tetrapod nanocomposites was the sum of the absorption spectra of P3HT and CdTe tetrapods. The nearly complete quenching in the emission of nanocomposites was indicative of efficient charge transfer at the P3HT/CdTe tetrapod

interface. These intimate semiconducting organic-inorganic nanocomposites may serve as promising materials, by improving optical absorption and electron transport owing to the incorporation of intriguing three-dimensional structures of CdTe tetrapods, for a wide range of applications, including hybrid solar cells, LEDs, FETs, and sensors.

## 5. Semiconducting conjugated polymer grafted CdSe tetrapod nanocomposites

Jaehan Jung, Ah-young Song, Young jun Yoon, Xinchang Pang, and Zhiqun Lin, “*Semiconducting Conjugated Polymer-inorganic Tetrapods Nanocomposites for solar cells*” (manuscript in preparation).

### 5.1. Introduction

In the previous two chapters, we have crafted P3HT-CdSe NR and P3HT-CdTe tetrapod nanocomposites, respectively, with no need for ligands exchange processes. However, this approach has several issues: 1) the existence of residue insulating ligands (i.e., TDPA) which was necessary to control the shape of NCs (e.g., the ratio between TDPA and Br-BPA (BrCH<sub>2</sub>BA) was 4:1) may hinder the charge transport in the active layer, and 2) achieving high-quality CdSe tetrapods was difficult. Indeed, their use in photovoltaics was not satisfactory due probably to the presence of residue insulating fatty ligands regardless of the much facilitated electronic interaction between P3HT and CdSe NRs. Moreover, it was not feasible to achieve high-quality CdSe tetrapods even at the high monomer concentration or high ratio of short mobile ligands. As tetrapods enable more efficient charge transport due to their intrinsic three-dimensional architecture, we explore the synthesis of P3HT-CdSe tetrapod nanocomposites in order to address issues mentioned above.

In this chapter, we utilized P3HT-grafted CdSe tetrapod nanocomposites prepared

via catalyst-free click chemistry as an active layer to produce hybrid bulkheterojunction solar cells. First, CdSe tetrapods with high selectivity were prepared by inducing elongated arms from CdSe zincblende seeds through the combination of the use of halide ligands, continuous precursor injection, and seed mediated growth. Subsequently, oleic acid (OA) capped CdSe tetrapods underwent inorganic acid treatment to completely remove insulating fatty ligands (i.e., oleic acid), followed by introducing 4-azidobenzoic acid or 5-bromovaleric acid a bifunctional ligand. Finally, ethynyl-terminated P3HT synthesized by a quasi-living Grignard metathesis (GRIM) method was grafted onto azide functionalized CdSe tetrapods via a catalyst-free alkyne-azide cycloaddition, yielding P3HT-CdSe tetrapod nanocomposites without employing any metallic impurities, which may possibly be detrimental to the device performance. The success of grafting was confirmed using Fourier transform infrared spectroscopy (FTIR) and nuclear magnetic resonance spectroscopy (NMR). The absorption and photoluminescence studies indicated the intimate contact between P3HT and CdSe tetrapods. Finally, P3HT-CdSe tetrapod hybrid devices were fabricated and optimized.

## 5.2. Experimental

All chemicals, including cadmium oxide, tri-n-octylphosphine (TOP, 90%), selenium powder, sodium azide, 2,5-dibromo-3-hexylthiophene, Ni(dppp)Cl<sub>2</sub>, tert-butylmagnesium chloride (2mol/L in diethyl ether), and ethynylmagnesium bromide (0.5 mol/L in THF) from Sigma Aldrich, Fluoroboric acid (HBF<sub>4</sub>), *N*-Methylformamide (NMF), hexane from Alfa Aesar, and 4-azidobenzoic acid, 5-bromovaleric acid, 1-

octadecene (ODE, 90%), oleic acid (OA, 97%), Cetyl trimethylammonium bromide (CTAB) from TCI were used as received. THF (VWR, 99%) was refluxed over sodium wire and distilled from sodium naphthalenide solution.

***Preparation of injection solution:*** Cadmium oleate ( $\text{Cd}(\text{OA})_2$ ) precursor solution was prepared by modifying previously reported work. 10 mmol of CdO, 7.8 ml of OA, 6.2 ml of ODE, and 1 ml of TOP were mixed and heated to 280 °C under Ar for 30 min. Once the solution became colorless and clear, the reaction was cooled down to 50 °C, followed by addition of CTAB (0.14 mmol). Separately, the mixture of Se and TOP was heated at 200 °C to yield transparent solution and then cooled down. 5 ml of TOPSe solution was added to the cadmium oleate precursor solution and stirred for 10 min.

***Synthesis of CdSe seeds with zinc blende structure:*** Zincblende CdSe QDs were synthesized by utilizing oleic acid as surfactants as reported elsewhere. First, the injection solution (i.e., 0.5M  $\text{Cd}(\text{OA})_2$  solution was prepared as follows. CdO (5mmol), OA (5ml), and ODE (5ml) were placed in three neck flask and then heated to 120 °C. Then Se powder and ODE were placed in three neck flask and heated up to 300°C under Ar. After the solution became clear and transparent, 4 ml of 0.5M  $\text{Cd}(\text{OA})_2$  precursor solution was injected to initiate the nucleation and growth. CdSe QDs were allowed to grow at 270°C for 15 min. The heating mantle was then removed to stop reaction. 6 ml of ODE was added to the solution once the temperature became 70°C. The resulting CdSe zinc blende solution was used without further purification.

***Synthesis of CdSe tetrapods:*** 0.15  $\mu\text{mol}$  of CdSe zincblende seeds were mixed

with 1.25 ml of OA, 0.75 ml of TOP, 10.5 ml of ODE, and 0.21 mmol of CTAB. The mixture was then heated to 260 °C, where precursor solution was injected with the rate of 0.4 ml/min for 50 min. The heating mantle was removed to stop the reaction and 5 ml of hexane was added at 70°C. The excess amount of acetone were added and centrifuged to purify the resulting solution.

*Surface modification of CdSe tetrapods with HBF<sub>4</sub> and bifunctional ligands:*

50 mg/ml of oleic acid capped-CdSe tetrapods were dissolved in 5 ml of hexane. 0.5 ml of HBF<sub>4</sub> (48wt% in H<sub>2</sub>O) and 5 ml of NMF were added to the CdSe tetrapods solution in hexane. The mixture was then shaken with vortex-mixing about 1 min. CdSe tetrapods were collected in the polar NMF phase, and oleic acid remained in the nonpolar hexane phase. The hexane phase containing oleic acid was discarded and 5 ml of hexane was added. Residue oleic acid in the NMF phase was washed out via vortex mixing. After three repeated washing procedures, the mixture was precipitated with an excess amount of acetone. The HBF<sub>4</sub> treatment step was conducted for three times to completely remove oleate ligands.

To modify bare CdSe tetrapods with bifunctional ligands, HBF<sub>4</sub>-treated CdSe tetrapods were precipitated with the excess amount of acetone and redispersed in a chloroform/5-bromovaleric acid or a THF/4-azidobenzoic acid to yield 5-bromovaleric acid-capped CdSe tetrapods or 4-azidobenzoic acid-functionalized CdSe tetrapods, respectively. The resulting bifunctional ligands-capped CdSe tetrapods solution was purified with chloroform/acetone or THF/acetone three times to remove remaining HBF<sub>4</sub>. Finally, 5-bromovaleric acid capped CdSe tetrapods (or 4-azidobenzoic acid-capped

CdSe tetrapods) were dispersed in chloroform (or THF).

***Synthesis of ethynyl-terminated P3HT:*** Ethynyl-terminated P3HT (i.e., P3HT–≡) was synthesized by a quasi-living Grignard metathesis (GRIM) method.<sup>85</sup> Briefly, 2,5-dibromo-3-hexylthiophene (0.815g, 2.5 mmol) was dissolved in THF (5ml) in a three-neck flask and stirred under Ar. Tert-butyilmagnesium chloride (1.25ml, 2.5mmol) was added. The mixture was stirred for 2 h at room temperature. Subsequently, it was diluted to 25mL with THF, followed by the addition of Ni(dppp)Cl<sub>2</sub> (56 mg, 0.1 mmol). The resulting solution was stirred for 30 min at room temperature, producing intermediate P3HT; it was then reacted with ethynylmagnesium bromide (2ml, 1mmol) in THF for 30 min. The product, P3HT–≡, was obtained by precipitating the reaction mixture in methanol, filtering in an extraction thimble, and washing by Soxhlet extraction with methanol, hexane, and chloroform sequentially. It was recovered after chloroform evaporated.

***Synthesis of P3HT–CdSe tetrapod nanocomposites by click reaction:*** Sodium azide (NaN<sub>3</sub>) was added to 5-bromovuleric acid-functionalized CdSe tetrapod THF solution, and then stirred at room temperature for three days, resulting in 5-azidovaleric acid-capped CdSe tetrapods. The excess amount of NaN<sub>3</sub> was removed by centrifugation. The resulting 5-azidovaleric acid-capped CdSe tetrapods were then precipitated with methanol. Subsequently, 50 mg of P3HT–≡ and 50 mg of 5-azidovaleric acid-capped CdSe tetrapod were mixed in 10 ml THF and kept at 65°C under Ar for two days. For 4-azidobenzoic acid-functionalized CdSe tetrapods, they were directly grafted with ethynyl-terminated P3HT in chloroform. The final product (i.e., P3HT–CdSe tetrapod

nanocomposites) was cooled to room temperature and diluted 10 times with THF. The resulting solution was precipitated with methanol twice to remove free P3HT which was not coupled with CdSe tetrapods.

***Fabrication of P3HT-CdSe tetrapods hybrid solar cells:*** Solar cells were fabricated as follows. ITO glasses were washed with acetone, methanol, and isopropanol sequentially, followed by oxygen plasma cleaning. Next, PEDOT:PSS (Poly(3,4-ethylenedioxythiophene):poly(styrenesulfonate)) layer of 40 nm thickness were spin-casted and annealed at 140 °C for 40 min in air. P3HT-CdSe tetrapod nanocomposites dissolved in chloroform (or chloroform and chlorobenzene mixture) with a concentration of 30 mg/ml were spin-coated, yielding approximately 100~200-nm thick photoactive layer. All samples were annealed at 130 °C for 15 min and 100 nm of aluminum electrode were deposited with a thermal evaporator at  $10^{-6}$  torr. All fabrications were done in an inert atmosphere. Devices were characterized at 25 °C under AM1.5 conditions.

***Characterization:*** The morphology of CdSe NCs and P3HT–CdSe tetrapod nanocomposites were studied by low-resolution and high-resolution transmission electron microscope (JEOL 100cx and Tecnai F30). The photophysical properties of CdSe tetrapods and P3HT-CdSe tetrapod nanocomposites were explored by a UV-Vis spectrometer (UV-2600, Shimadzu) and a spectrofluorophotometer (RF-5301PC, Shimadzu). All samples were excited at  $\lambda_{\text{ex}} = 445$  nm and the emission were collected at  $\lambda_{\text{em}} > 500$  nm. The  $^1\text{H}$  NMR and Fourier transform infrared (FTIR) spectra were taken by using a Varian VXR-400 spectrometer.

### 5.3. Results and Discussion

P3HT-grafted CdSe tetrapod nanocomposites were synthesized via catalyst-free click chemistry. The ability to chemically tether P3HT on the CdSe tetrapod surface can promote electronic interaction between these two semiconductors as well as a uniform dispersion of CdSe tetrapods in P3HT matrix. In this study, CdSe tetrapods were utilized as electron acceptor due to their excellent inherent carrier mobility and advantageous size and shape for the use in hybrid solar cells. Considering the typical thickness of hybrid cells (i.e., from 70 to 200 nm), the intrinsic three-dimensional structure of CdSe tetrapods is beneficial for efficient charge transport in photoactive layer compared to the corresponding QDs or NRs, where electron hopping among them is required.

However, achieving high-quality CdSe or CdTe tetrapods is challenging as can be seen in Chapter 2 and 3. Especially for CdSe NCs, large fraction of nanorods or tripods were coexisted with tetrapods. Moreover, their shape was not well-controlled, possessing hyperbranched architecture at high concentration. Alivisatos and co-workers theorized that the formation of tetrapods is the result of nucleation of zinc blende particles, followed by surface-initiated growth of wurtzite arms.<sup>88</sup> Hence, high tetrapod selectivity depends on the fraction of zinc blende nanoparticles and the selective growth of wurtzite-only arms from zinc blende seeds. In case of CdTe, the cohesive energy difference between the two polymorphs (i.e., zinc blende and wurtzite) is sufficiently large (i.e., approximately  $10 \text{ meV}$ )<sup>4</sup> to selectively initiate zinc blende seeds without appearance of wurtzite seeds, and small enough to allow the wurtzite phase to grow off the zinc blende nanoparticle surface. In contrast, the inherent small energy difference between its two polymorphs of CdSe NCs (less than 1 meV) compared to CdTe NCs leads to low

selectivity of tetrapods. Indeed, in Chapter 3, while relatively high-quality CdTe tetrapods were achieved by simply increasing monomer concentration via utilizing short mobile ligands (i.e., Cd-BBPA), but attempts to produce high quality CdSe tetrapods was not successful through the simple tuning of the monomer concentration or the utilization of short mobile and reactive ligands as can be seen in Chapter 2. In this context, provoking elongated arms from zincblende CdSe QDs is an elegant mean of achieving high quality CdSe tetrapod architecture if several conditions are satisfied as follows: 1) obtaining pure or high fraction of zinc blended CdSe QD seeds, 2) enabling growth of arms from seeds in wurtzite phase, and 3) maintaining the monomer concentration in kinetic growth regime for the anisotropic growth.

Taken together, in order to synthesize good quality of CdSe tetrapods with high selectivity, zincblende CdSe QDs were first prepared and then wurtzite arms were grown from the surface of zincblende seeds via a continuous precursor injection method in the wurtzite phase favorable condition. For preparation of zincblende CdSe QD seeds, oleic acids were employed as surfactants due to their stabilizing effect for zincblende structure. This enabled the formation of zincblende crystal structure even above 100 °C despite CdSe wurtzite phase is dominant over zincblende above 100 °C. However, it is worth noting that the later hindered the formation of wurtzite phase arms during injection regime, causing the poor selectivity of CdSe tetrapods. This can be addressed by the use of halide ligands as they selectively bind to cadmium atoms much stronger than oleic acid, thereby removing oleic acid effectively and allowing wurtzite phase formation.

Herein, in this study, high-quality CdSe tetrapods were prepared from zincblende

CdSe QD seeds via a continuous precursor injection method (CPI), where the precursors were injected successively into the seed solution (i.e., CdSe ZB QDs) in order to maintain the reaction condition in the kinetic growth regime for anisotropic growth of arms. In addition, the utilization of halide ligands triggered the formation of four wurtzite arms elongated from {111} facets of the zincblende seeds. Specifically, precursor solution containing halide ligands was continuously provided to zincblende CdSe seeds solution to maintain the high enough concentration to trigger anisotropic growth but below the nucleation limit to prohibit the additional formation of QDs. As noted above, halide ligands selectively binds to the  $(11\bar{2}0)$  and  $(10\bar{1}0)$  facets effectively than oleic acid, thus effectively replacing oleic acid. This in turn favored the wurtzite phase compared to the zincblende structure (i.e., WZ phase is favorable than ZB without OA), resulting in elongated arms in wurtzite phase from zincblende QDs as CPI method ensures high enough precursor concentration for anisotropic growth. The high-resolution TEM images (**Figure 5.1**) revealed that wurtzite four arms with a diameter of  $7.56\pm 0.23$  nm and a length of  $41\pm 2$  nm from zincblende CdSe seeds of a diameter of  $5.12\pm 0.16$  nm grew successfully under these conditions. The advantage of the combination of continuous injection and the use of halide ligands lies in not only its high selectivity but also in its ease of tuning the arm length or diameter. For example, different size of CdSe tetrapods can be synthesized from same zincblende CdSe seeds (**Figure 5.1a and 5.1b**) simply by controlling the amount of injection volume. We controlled the injection time to be 10 min, 50 min, and 90 min with fixed injection rate of 0.4 ml/min. The arm length was determined to be 10 nm (16 nm in total), 40 nm (65 nm in total), and 65 nm (94 nm in total) for the injection time of 10 min, 50 min, and 90 min, respectively, according to

TEM studies. However, CdSe QDs was also existed with CdSe tetrapods, indicating that some CdSe QD seeds were not grown into tetrapods due possibly to the following reasons: 1) the rate and concentration of injection volume, 2) the amount of employed CdSe zincblende seeds, and 3) the reaction temperature. Although these conditions are interconnected, the number of CdSe zincblende QDs introduced as seeds was critical as it

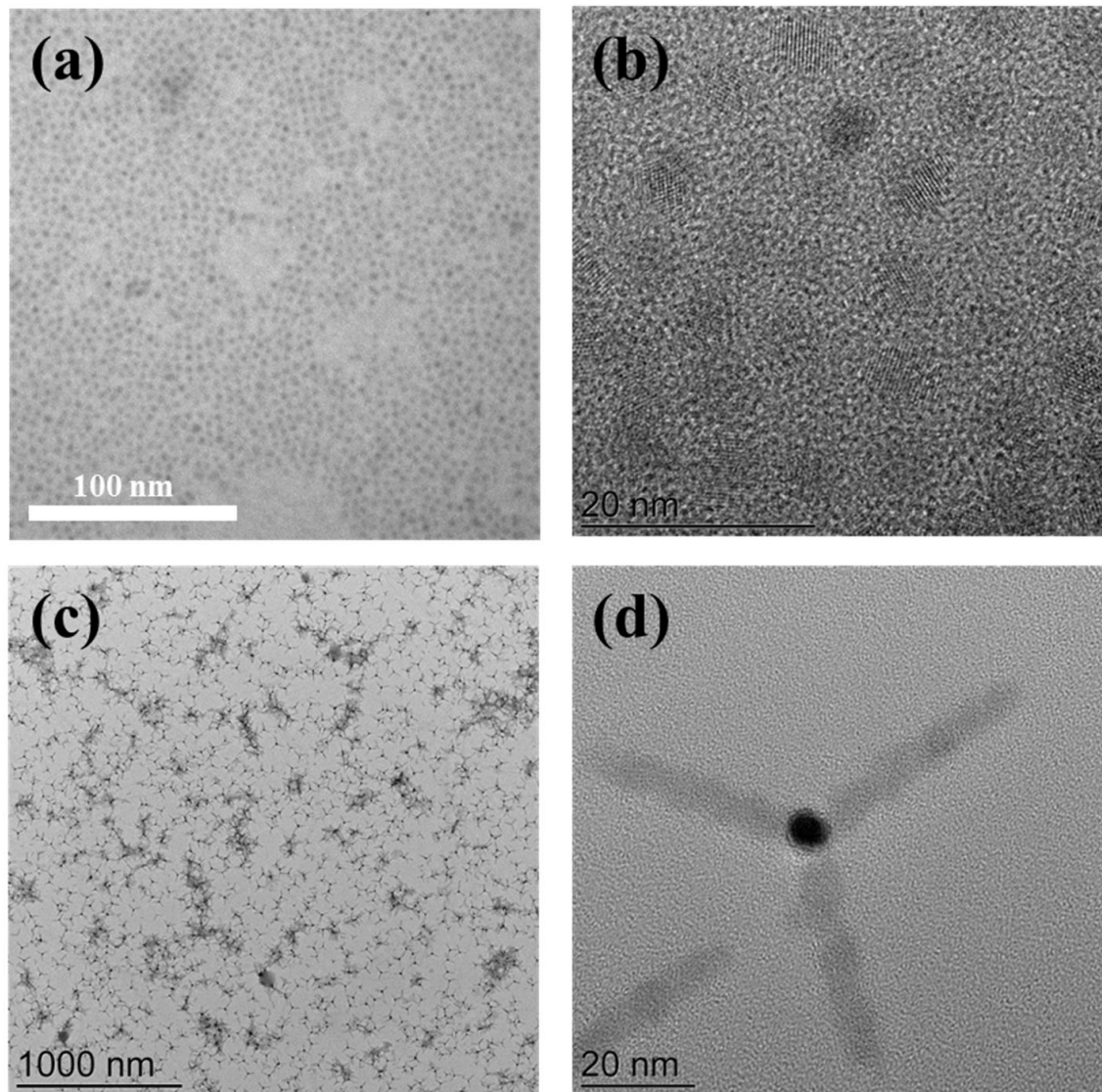


**Figure 5.1.** TEM images of (a) oleic acid-capped zinc blende CdSe QD seeds, (b) close-up of zincblende CdSe QDs, (c, d) CdSe tetrapods grown from CdSe zincblende seeds.

significantly affected not only the number of halide ligands per CdSe seed surfaces but also the precursor concentration per QD surfaces. In this context, the impact of the number of seeds on the tetrapods selectivity was explored. Specifically, CdSe zincblende QD seeds with the concentration of  $50\mu\text{mol/L}$ ,  $25\mu\text{mol/L}$ , and  $5\mu\text{mol/L}$  were introduced, followed by the injection of  $0.5\text{ M Cd(OA)}_2$  precursor solution at the rate of  $0.4\text{ml/min}$  at

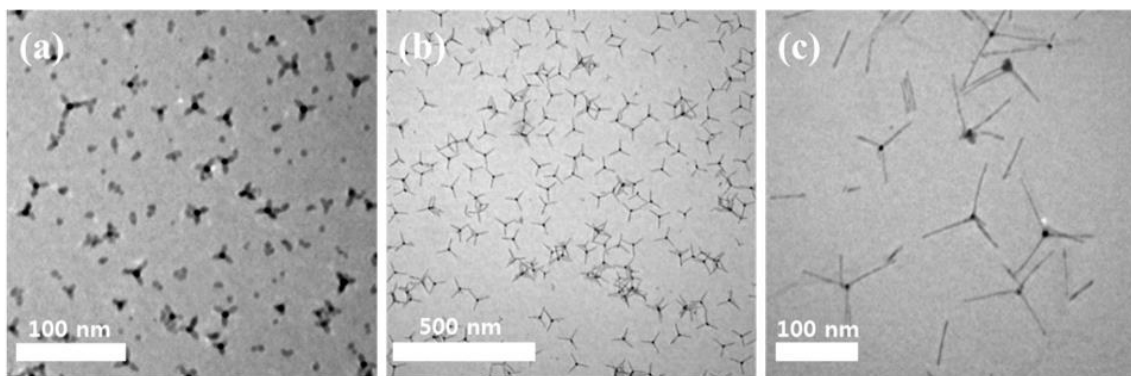


**Figure 5.2.** TEM images of (a) oleic acid-capped zinc blende CdSe QD seeds, (b) close-up of zinc blende CdSe QDs, (c, d) CdSe tetrapods grown from CdSe zinc blende seeds.

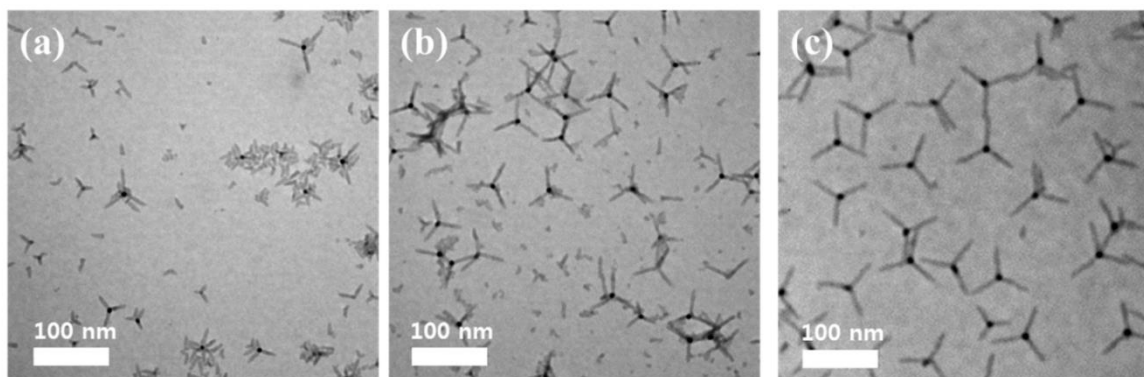
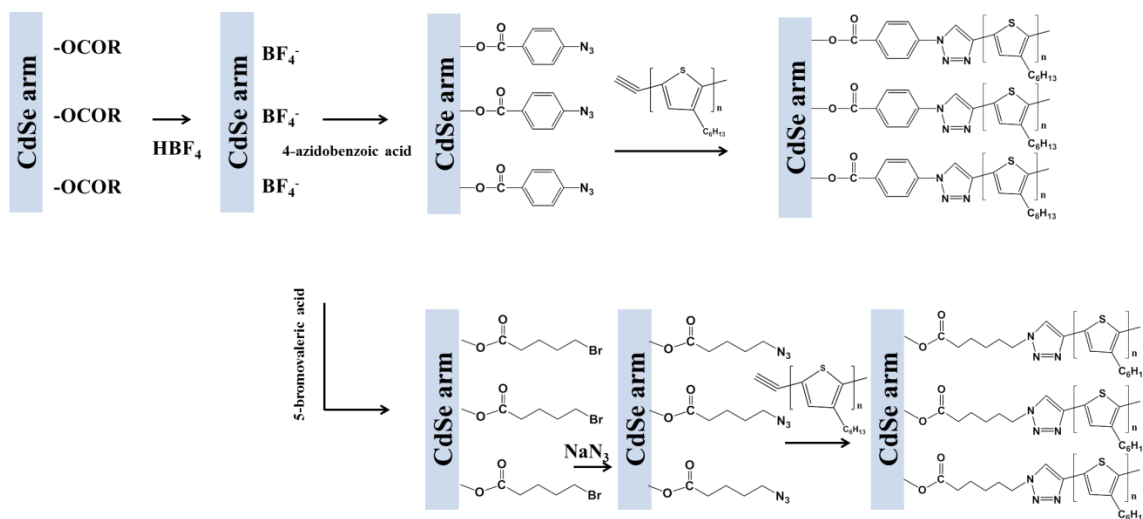


**Figure 5.3.** TEM images of CdSe tetrapods prepared with the seed concentration of (a)  $50\mu\text{mol/L}$ , (b)  $25\mu\text{mol/L}$ , and (c)  $5\mu\text{mol/L}$ .

260°C for 50 min. The resulting tetrapods size was 30 nm, 45 nm, and 70 nm for the concentration of 50 μmol/L, 25 μmol/L, and 5 μmol/L, respectively. Notably, QDs, dipods, and tripods were also coexisted with tetrapods when high seed concentration (i.e., 50 and 25 μmol/L) was employed (**Figure 5.3a and 5.3b**), while the high fraction of CdSe tetrapods was obtained at the low seed concentration of 5 μmol/L (**Figure 5.3 c**). This was because the flux of monomer reaching the QD surface may not be enough to trigger an anisotropic growth when the number of introduced seeds exceeded the certain threshold. Moreover, the high CdSe QD concentration reduced the number of halide ligands exposure to the CdSe surfaces, thereby retarding the elimination of OA ligands from cadmium atoms. This in turn impeded the facilitated phase transform from zincblende into wurtzite, resulting in zincblende seeds formation rather than the growth of wurtzite arms.



**Scheme 5.1.** Grafting ethynyl-terminated P3HT onto azide-functionalized CdSe tetrapods with inorganic treatment via catalyst-free click chemistry, yielding P3HT-CdSe tetrapod nanocomposites.

In spite of the necessity of surfactants for the synthesis of well-controlled NCs, they hinder the electron transport especially when used in opto-electronic devices as we already demonstrated in Chapter 2. Thereby, insulating ligands (i.e., oleic acid) were then removed with inorganic acid treatment as the ligand exchange via inorganic acid treatment was an effective and robust route to completely removing unnecessary insulating molecules. Specifically, to modify the CdSe tetrapod surface with desired bifunctional ligands, a two-phase ligand exchange method using tetrafluoroboric acid ( $\text{HBF}_4$ ) was employed (**Scheme 5.1**). The mixture of  $\text{HBF}_4$  and polar solvent (i.e., NMF) and OA-capped CdSe tetrapods in nonpolar solvent (i.e., hexane) were vigorously shaken with vortex-mixing, resulting in the transfer of CdSe tetrapods from hexane phase to NMF phase. The transfer of CdSe tetrapods occurred because positive Cd atom sites are surrounded by  $\text{BF}_4^-$  counter ions, which indicated the detachment of OA from CdSe surface. Upon the disappearance of the vibrational peaks from alkyl chains ( $2800\sim 3000\text{ cm}^{-1}$ ) in the FTIR spectra, the success of ligands exchange was confirmed (**Figure 5.4**). Strong absorption of OA-capped CdSe tetrapods at  $2955\text{ cm}^{-1}$ ,  $2923\text{ cm}^{-1}$ , and  $2846\text{ cm}^{-1}$  can be assigned to the asymmetric C-H stretching vibrations in  $-\text{CH}_3$ ,  $-\text{CH}_2$ , and the symmetric C-H stretching vibration in  $-\text{CH}_2$ , respectively, from alkyl chain of OA ligands. After the treatment of OA-functionalized CdSe tetrapods with  $\text{HBF}_4$ , these peaks were disappeared, which was indicative of the complete removal of oleate ligands. Subsequently, 4-azidobenzoic acid or 5-bromovaleric acid were employed as bifunctional ligands since carboxyl acids at the one end can act as capping agents with CdSe NCs, and azide or bromine group at the other end can be utilized as the coupling group (**Scheme 5.1**). The  $\text{HBF}_4$  treated CdSe tetrapods were precipitated with centrifugation and

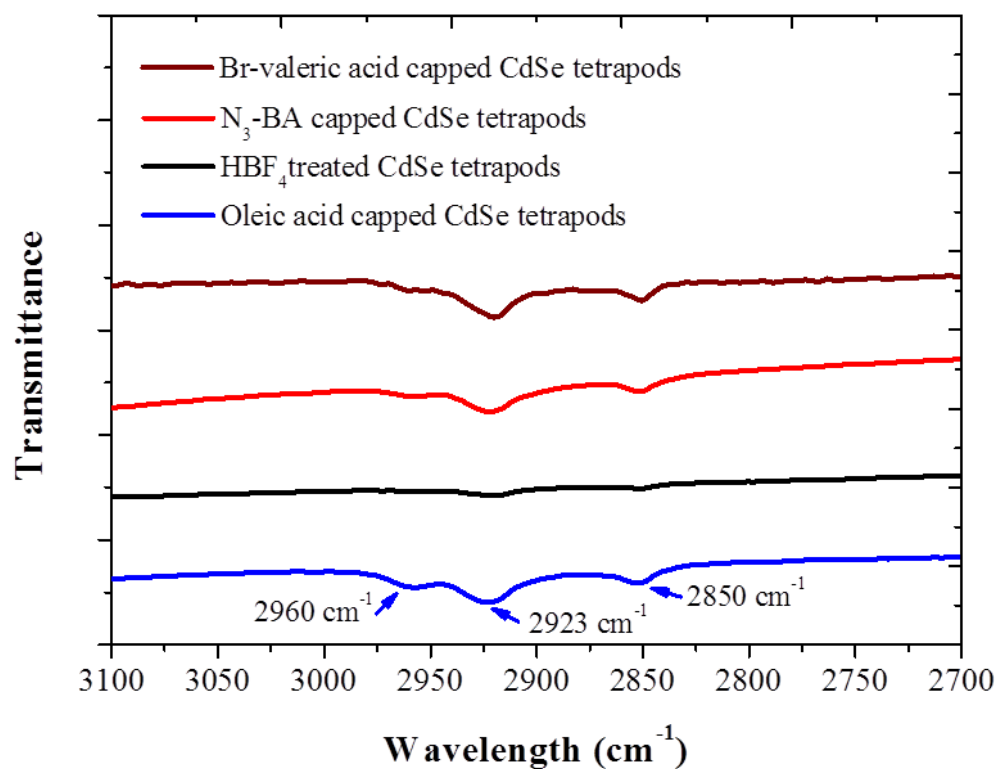


**Figure 5.4.** FTIR spectra of as-prepared OA-capped CdSe tetrapods (blue), CdSe tetrapods treated with HBF<sub>4</sub> (black), and N<sub>3</sub>-BA functionalized CdSe tetrapods after capping with 4-azidobenzoic acid (red), and 5-bromovaleric acid capped CdSe tetrapods (brown).

redispersed in THF containing 4-azidobenzoic acid or 5-bromovaleric acid. The absorption peaks at 2959 cm<sup>-1</sup>, 2923 cm<sup>-1</sup>, and 2853 cm<sup>-1</sup> from 4-azidobenzoic acids and 5-bromovaleric acids then reappeared, which was indirect evidence of capping of 4-azidobenzoic acid (or 5-bromovaleric acid) onto CdSe tetrapod surface.

To further verify the ligand attachment to CdSe tetrapod surface, X-ray photoelectron spectroscopy (XPS) study was performed. The binding energy of O<sub>1s</sub> for 4-

azidobenzoic acid, OA-capped CdSe tetrapods, and N<sub>3</sub>-BA-capped CdSe tetrapods were compared (**Figure 5.5**). Apparently, the peak maxima differed by about 0.6 eV. This shift can be explained by the difference in electron density of oxygen atoms resulted from the binding of 4-azidobenzoic acid ligands to CdSe surface, suggesting the success in capping ligands onto CdSe tetrapods.

The resulting azide-functionalized CdSe tetrapods were then grafted with ethynyl-terminated P3HT via catalyst-free click chemistry, yielding P3HT-CdSe tetrapod nanocomposites (**Scheme 5.1**). Bromine moiety of 5-bromovaleric acid capped CdSe tetrapods were converted into azide group by stirring with sodium azide, forming 5-azidovaleric acids-capped CdSe tetrapods. The success of grafting between two

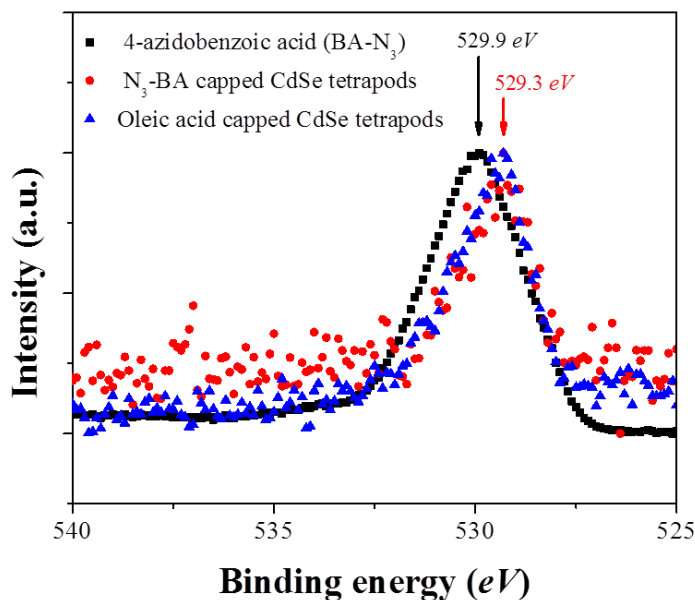


**Figure 5.5.** XPS spectra for O<sub>1s</sub> binding energies for 4-azidobenzoic acid (N<sub>3</sub>-BA, black square), N<sub>3</sub>-BA-capped CdSe tetrapods (red circle), and OA-capped CdSe tetrapods (blue triangle).

semiconductor constituents was confirmed by FTIR and HNMR. **Figure 5.6** compares FTIR spectra of bare CdSe tetrapods (i.e.,  $\text{BF}_4^-$  stabilized CdSe tetrapods),  $\text{N}_3$ -functionalized CdSe tetrapods (i.e.,  $\text{N}_3$ -BA capped CdSe tetrapods or  $\text{N}_3$ -vul capped CdSe tetrapods), and P3HT-CdSe tetrapods nanocomposites. The absorption peaks at  $2955\text{ cm}^{-1}$ ,  $2923\text{ cm}^{-1}$ , and  $2846\text{ cm}^{-1}$  were assigned to the asymmetric C-H stretching vibrations in  $-\text{CH}_3$ ,  $-\text{CH}_2$ , and the symmetric C-H stretching vibration in  $-\text{CH}_2$ , respectively, from the alkyl side chains in P3HT and ligands. Obviously, the characteristic peak assigned to  $-\text{N}_3$  vibration was appeared as well at  $2040\text{ cm}^{-1}$  for both 4-azidobenzoic acids-functionalized CdSe tetrapods and 5-azidovaleric acids-capped CdSe tetrapods ( $\text{N}_3$ -vul-capped CdSe tetrapods). This peak was then disappeared after the  $\text{N}_3$ -BA-capped CdSe tetrapods (or  $\text{N}_3$ -vul-capped CdSe tetrapods) coupled with ethynyl-terminated P3HT, substantiating the successful grafting of P3HT onto the CdSe tetrapods through 1,3-dipolar cycloaddition between ethynyl group in P3HT and azide group in  $\text{N}_3$ -BA-functionalized CdSe tetrapods. The  $^1\text{H}$  NMR measurement (**Figure 5.7**) also strongly suggested the occurrence of grafting between P3HT and  $\text{N}_3$ -BA capped CdSe tetrapods (or  $\text{N}_3$ -vul capped CdSe tetrapods). A proton signal at 3.5 ppm from the ethynyl group on the P3HT chain end (**Figure 5.7a**) was not observed in P3HT-CdSe tetrapod nanocomposites after click coupling of P3HT with  $\text{N}_3$ -BA-CdSe tetrapods or  $\text{N}_3$ -vul-CdSe tetrapods as shown in **Figure 5.7b and 5.7c**, respectively. On the basis of the disappearance of azide peak at  $2040\text{ cm}^{-1}$  after click reaction between  $\text{N}_3$ -BA-CdSe tetrapods (or  $\text{N}_3$ -vul-CdSe tetrapods) and ethynyl-terminate P3HT, it is clear that the amount of ethynyl-terminated P3HT was enough to render the complete coupling with azide functional groups on the CdSe tetrapod.

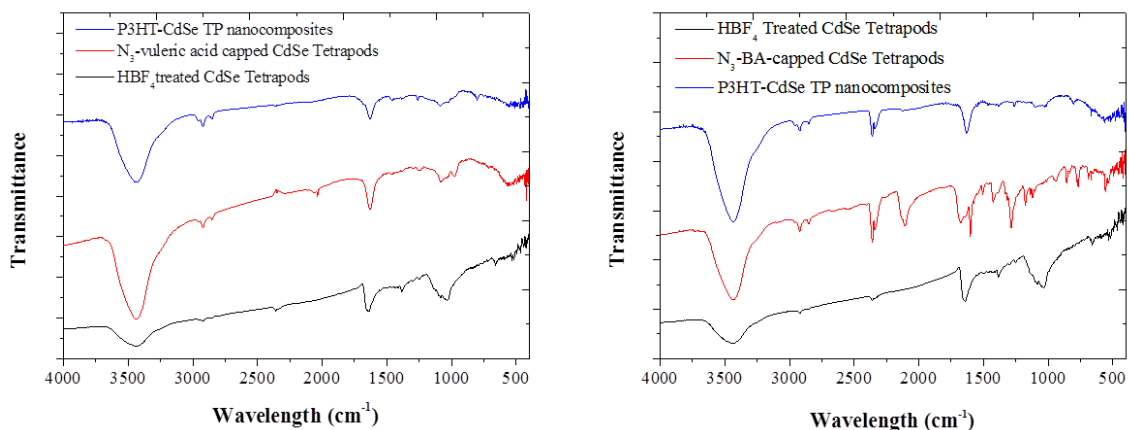


**Figure 5.6.** FTIR spectra of  $\text{HBF}_4$  treated CdSe tetrapods (black),  $\text{N}_3$ -BA functionalized CdSe tetrapods after capping with 4-azidobenzoic acid (red), and P3HT grafted CdSe tetrapods (blue).

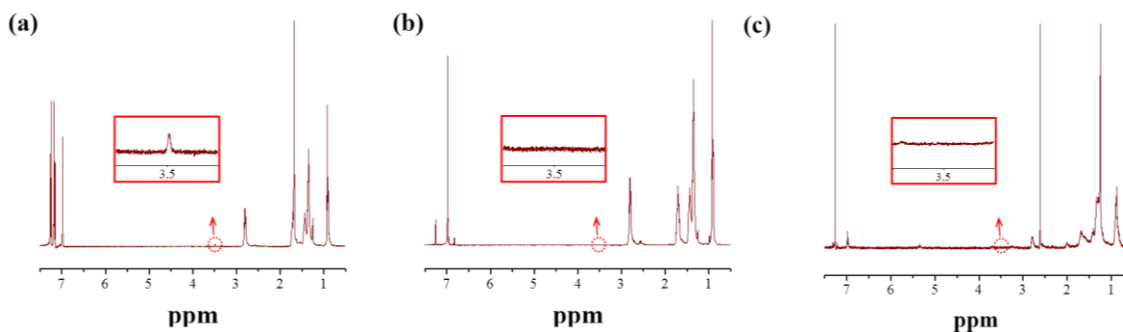


**Figure 5.7.**  $^1\text{H}$  NMR spectra of (a) ethynyl-terminated P3HT and P3HT-CdSe tetrapod nanocomposites prepared by grafting P3HT with (b)  $\text{N}_3$ -BA-CdSe tetrapods, and (c)  $\text{N}_3$ -val-CdSe tetrapods. The inset is the close-up of spectra at around 3.5 ppm.

The optical properties of P3HT, CdSe TPs, and P3HT-CdSe TP nanocomposites were explored by UV-vis absorbance and photoluminescence (PL) spectroscopies. The absorption spectra of ethynyl-terminated P3HT,  $\text{N}_3$ -BA-functionalized CdSe tetrapods, and P3HT-CdSe tetrapods nanocomposites in THF are shown in **Figure 5.8a**. The

absorption maxima of P3HT and CdSe tetrapods were at 450 nm and 652 nm, respectively. Obviously, the absorption spectrum of the resulting P3HT-CdSe tetrapods nanocomposites was a simple superposition of their two constituents. The PL spectra of simple physical mixture composed of ethynyl-terminated P3HT, P3HT/CdSe tetrapods, and P3HT-CdSe tetrapod nanocomposites prepared by click chemistry were measured (**Figure 5.8c**). The physical blending of P3HT/CdSe tetrapods was prepared by simply mixing P3HT and N<sub>3</sub>-BA-functionalized CdSe tetrapods. The weight ratio of CdSe tetrapods and P3HT was set to be the same, and can also be determined from UV-vis spectra (**Figure 5.8b**). The quenching of the emission of both nanocomposites and physical blending relative to the pristine P3HT homopolymer were observed, indicating the efficient charge transfer from electron-donating P3HT onto electron-accepting CdSe tetrapods. Notably, the PL emission quenching of P3HT-CdSe tetrapod nanocomposites

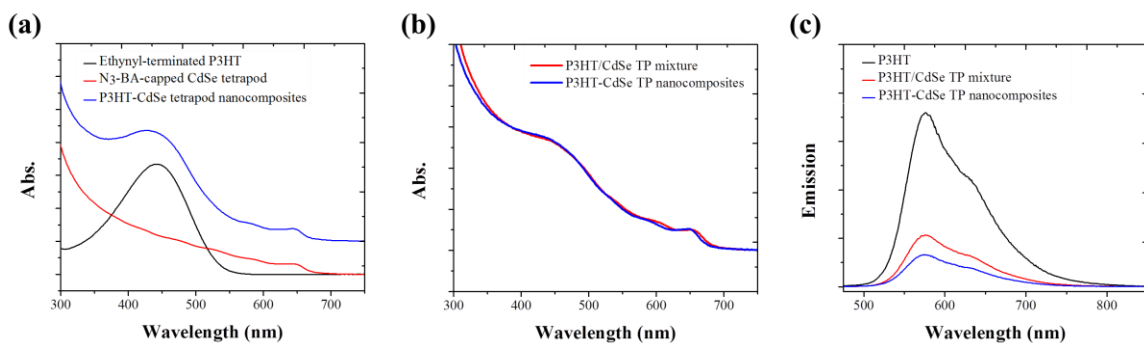


**Figure 5.8.** (a) Absorption spectra of ethynyl-terminated P3HT (black), N<sub>3</sub>-BA-functionalized CdSe tetrapods (red), and P3HT-CdSe tetrapod nanocomposites (blue) prepared via click coupling. (b) UV-vis spectra of P3HT/CdSe tetrapod mixture (red) and P3HT-CdSe tetrapod nanocomposites (blue). (c) Photoluminescence spectra of ethynyl-terminated P3HT (black), physical mixture of P3HT/CdSe tetrapod (red), and P3HT-CdSe tetrapod nanocomposites (blue).

was more obvious than that of P3HT/CdSe tetrapod mixture with same weight ratio, corroborating the success of coupling between P3HT and CdSe tetrapods. This observation further confirmed the intimate contact between P3HT and CdSe tetrapods.

Hybrid photovoltaic devices were fabricated utilizing as-prepared P3HT-CdSe tetrapods nanocomposites in photoactive layers. The influence of solvent, tetrapod size, and type of bifunctional ligands (i.e., 5-bromovaleric acid and 4-azidobenzoic acid) on the performance was examined. It is well-known that the use of high boiling point solvent promotes formation of highly self-ordered microcrystalline structures in P3HT, resulting in significantly improved mobility of P3HT film. This is because the retarded solvent evaporation in polymer matrix increases the available time for crystallization during the spin-coating process. In this context, the mixture of low boiling solvent chloroform (CF) and high boiling solvent chlorobenzene (CB) was employed as co-solvent for P3HT-CdSe tetrapod nanocomposites to control the crystallinity and thickness of film as they are good solvent for P3HT.

To optimize the solvent ratio between CF and CB, P3HT-CdSe tetrapod nanocomposites prepared via click coupling of N<sub>3</sub>-valeric acid capped CdSe tetrapods and ethynyl-terminated P3HT were dissolved in the mixture of chloroform and chlorobenzene. The ratio of these solvents studied in this work was 100% CB, 30% CB, 20% CB, and CF 100%. When only chloroform was used as solvent, the performance was 0.0591% with an open circuit voltage ( $V_{oc}$ ) of 0.659 V, a current density ( $J_{sc}$ ) of 0.278mJ/cm<sup>2</sup>, and a fill factor ( $FF$ ) of 32.3. The increase of high boiling point solvent (i.e., chlorobenzene) fraction to 0.2 resulted in a much improved performance (i.e., a PCE

of 0.174%, a  $J_{sc}$  of 0.987mJ/cm<sup>2</sup>, a  $V_{oc}$  of 0.624V, and a  $FF$  of 28.3). This was due possibly to the improved crystallinity of P3HT via slow evaporation of chlorobenzene. However, the decrease in overall performance was observed even at the chlorobenzene fraction of 0.3 which was owing to the poor solubility of nanocomposites in chlorobenzene. Moreover, further increase in chlorobenzene volume ratio led to the decreased PCE. Interestingly, the lowest PCE of 0.0216% (a  $J_{sc}$  of 0.128mJ/cm<sup>2</sup>, a  $V_{oc}$  of 0.590V, and a  $FF$  of 28.6) was observed when 100% CB was used. These values were even lower than those from

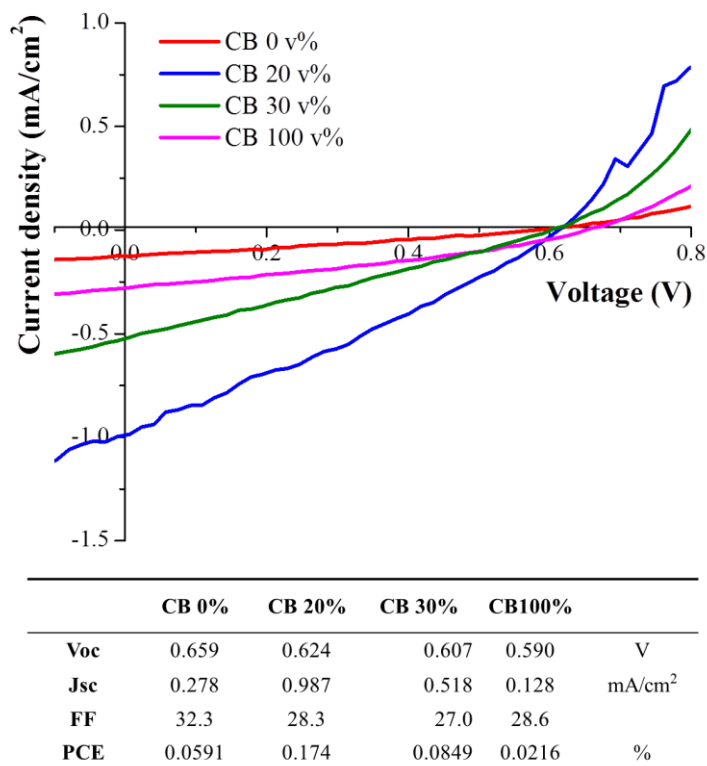


**Figure 5.9.** Current-voltage characteristics of hybrid P3HT-CdSe tetrapod solar cells with different solvent ratio of chlorobenzene and chloroform. P3HT-CdSe tetrapods samples were prepared via a click reaction between P3HT and N<sub>3</sub>-vul functionalized CdSe tetrapods.

the devices fabricated using 100% CF (a PCE of 0.591%, a  $J_{sc}$  of 0.278mJ/cm<sup>2</sup>, a  $V_{oc}$  of 0.659V, and a  $FF$  of 32.3). On the basis of this result, it can be speculated that achieving excellent dispersion of NCs is of key importance as the lowered PCE was observed in spite of the improved crystallinity of P3HT.

The influence of type of bifunctional ligands (i.e., 5-bromovaleric acid and 4-azidobenzoic acid) on the device performance was explored. In this study, the performance of devices fabricated using P3HT-CdSe tetrapod nanocomposites prepared by coupling 5-bromovaleric acid and 4-azidobenzoic acid-functionalized CdSe tetrapods with P3HT were compared. 5-bromovaleric acid and 4-azidobenzoic acid were selected as bifunctional ligands because of the similarity of their length but the difference in their structure. It should be noted that aromatic molecules have better charge transport properties than aliphatic molecules. Notably, the hybrid P3HT-CdSe tetrapod nanocomposites based on 4-azidobenzoic acids exhibited enhanced PCE approximately as much as three times compared with those by 5-bromovaleric acids (**Figure 5.10**). For hybrid photovoltaic devices fabrication, all devices were fabricated using a solvent mixture containing 20 volume% CB in CF and underwent thermal annealing at 130 °C for 15 min to improve crystallinity of P3HT. The highest performance of P3HT-CdSe tetrapods devices based on 5-bromovaleric acid was obtained when 65 nm CdSe tetrapods were utilized as acceptors. The PCE was 0.471% with a  $J_{sc}$  of 2.78mJ/cm<sup>2</sup>, a  $V_{oc}$  of 0.659V, and a  $FF$  of 27.9. However, the use of 4-azidobenzoic acid resulted in a PCE of 1.28% with a  $J_{sc}$  of 7.91mJ/cm<sup>2</sup>, a  $V_{oc}$  of 0.585V, and a  $FF$  of 27.8 at the same fabrication condition. This demonstrated that aryl molecules are better than insulating alkyl ligands in terms of electron transport.

P3HT-CdSe tetrapod nanocomposites prepared with different size of tetrapods either by employing 4-azidobenzoic acid or 5-bromovaleric acid were utilized to fabricate hybrid devices. Clearly, the PCE enhanced from 0.174% to 0.471% for 5-bromovaleric acid system (or from 0.567% to 1.28 % for 4-azidobenzoic acid system) as the size of CdSe tetrapods increased from 16 nm to 65 nm (**Figure 5.10**). This can be attributed to the facilitated charge carrier transport due to the extended arms of CdSe tetrapods, considering that the thickness of a photoactive layer was  $\sim 100$  nm. However, the use of 94-nm CdSe tetrapods decreased the performance of the resulting cells in spite of the advantageous size and shape of CdSe tetrapods. This was due to the

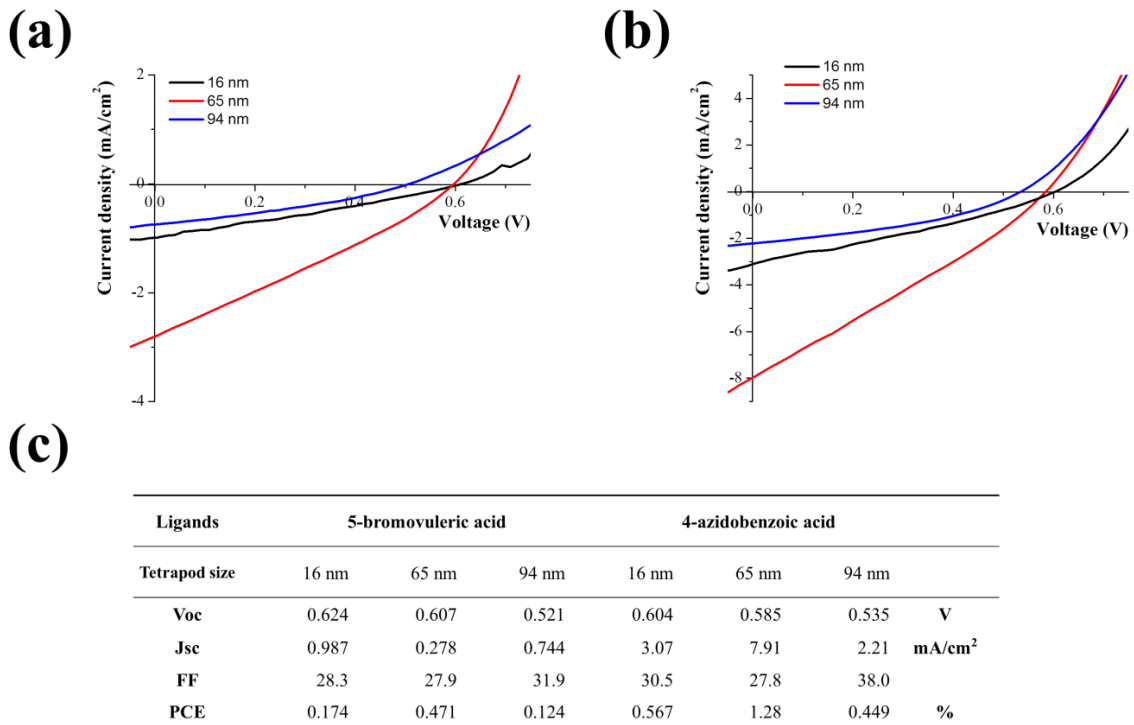


**Figure 5.10.** Current-voltage characteristics of hybrid solar cell devices fabricated with P3HT-CdSe tetrapod nanocomposites by employing (a) 5-bromovaleric acid and (b) 4-azidobenzoic acid. (c) Summary of device performance. The effect of CdSe tetrapod size on the PCE was also investigated.

aggregation of CdSe tetrapods in the P3HT matrix as the solubility of CdSe tetrapods decreased when their size increased. In order to investigate the behavior of P3HT-CdSe tetrapod (i.e., 94 nm in size) in P3HT polymer matrix depending on the weight ratio between P3HT and CdSe tetrapods, P3HT-CdSe tetrapod nanocomposites film of CdSe tetrapod weight fraction of 50% and 80% were prepared. TEM studies revealed that P3HT-CdSe tetrapod nanocomposites with 50 weight % of CdSe tetrapod were dispersed relative well in the P3HT matrix (**Figure 5.11 a and 5.11b**), while the increasing CdSe tetrapod weight fraction to 80% resulted in local agglomeration of CdSe tetrapods (**Figure 5.11 c and 5.11d**). This indicated that the amount of P3HT (20 weight %) was not enough to impart excellent dispersion of CdSe tetrapods in P3HT matrix. Despite excellent dispersion of CdSe tetrapods of 50 weight%, the devices didn't provide reasonable performance, even lower than those by P3HT-CdSe tetrapod nanocomposites of 80 weight%. Thus, it can be speculated that the role of CdSe tetrapods in the device performance was significant. The morphology of P3HT-CdSe tetrapod nanocomposites with the weight ratio of CdSe of 80% but the CdSe tetrapod size of 65 nm were examined by TEM as shown in **Figure 5.11e and 5.11f**. Obviously, the dispersion of small CdSe tetrapods (i.e., 65 nm in a size) in P3HT matrix was better than larger counterparts (i.e., 94 nm in a size). This can be the possible explanation of improved PCE for P3HT-CdSe tetrapod nanocomposites with a tetrapod size of 65 nm compared to those with 94 nm CdSe tetrapods. **Figure 5.12** shows AFM height and phase images of P3HT-CdSe tetrapod (94nm in a size and 80% of CdSe by weight) nanocomposites film. Notably, phase segregation (**Figure 5.12a and 5.12d**) appeared as also observed in the TEM studies. From the close-up images, the local agglomeration of CdSe tetrapods (**Figure**

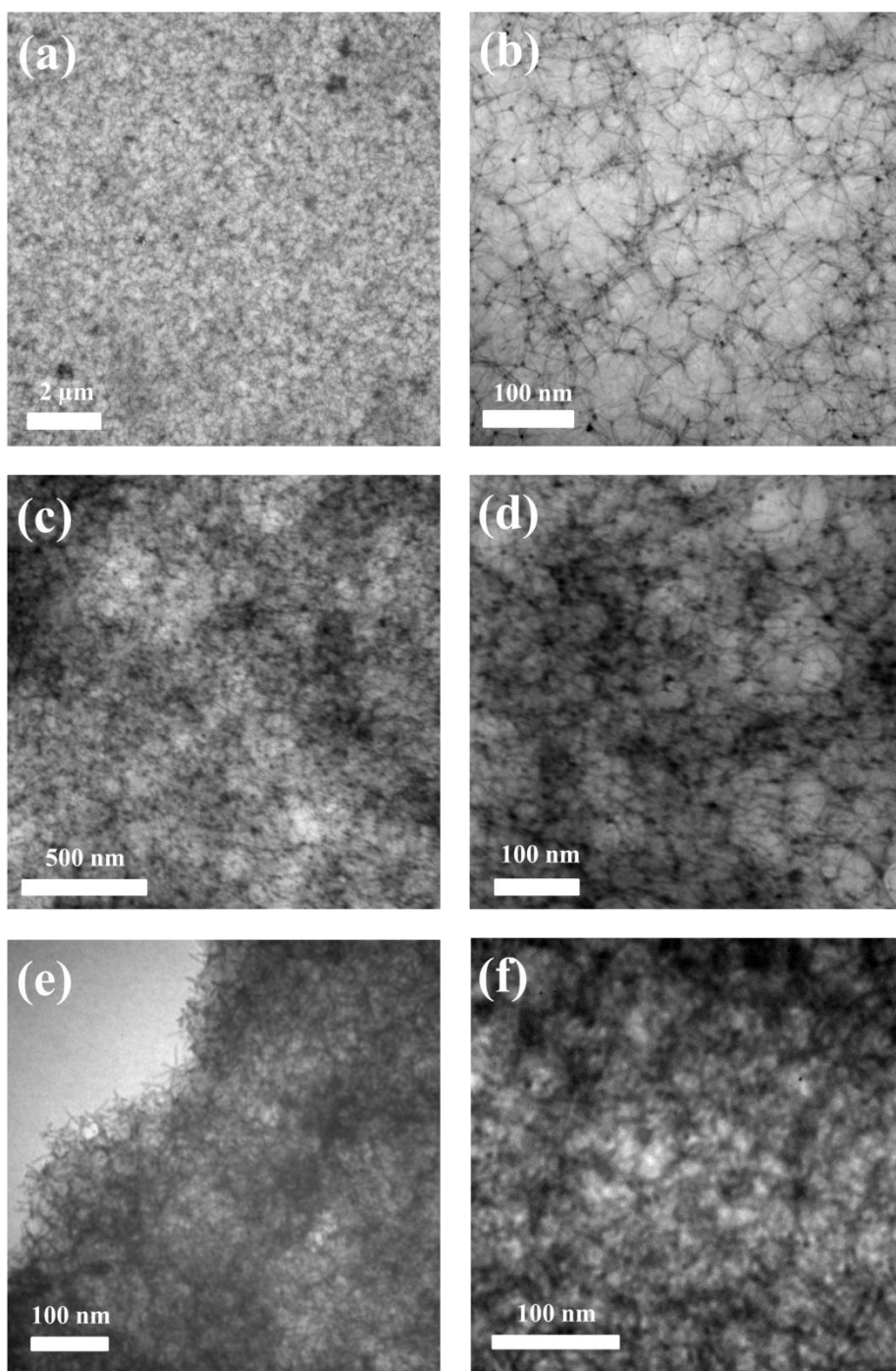


**Figure 5.11.** TEM images of films prepared by (a,b) P3HT-CdSe tetrapod nanocomposites with the size of CdSe tetrapod of 94 nm and its weight fraction of 50%, (c,d) P3HT-CdSe tetrapod nanocomposites with the size of CdSe tetrapod of 94 nm and its weight fraction of 80%, and (e,f) P3HT-CdSe tetrapod nanocomposites the size of CdSe tetrapod of 65 nm and its weight fraction of 50%.

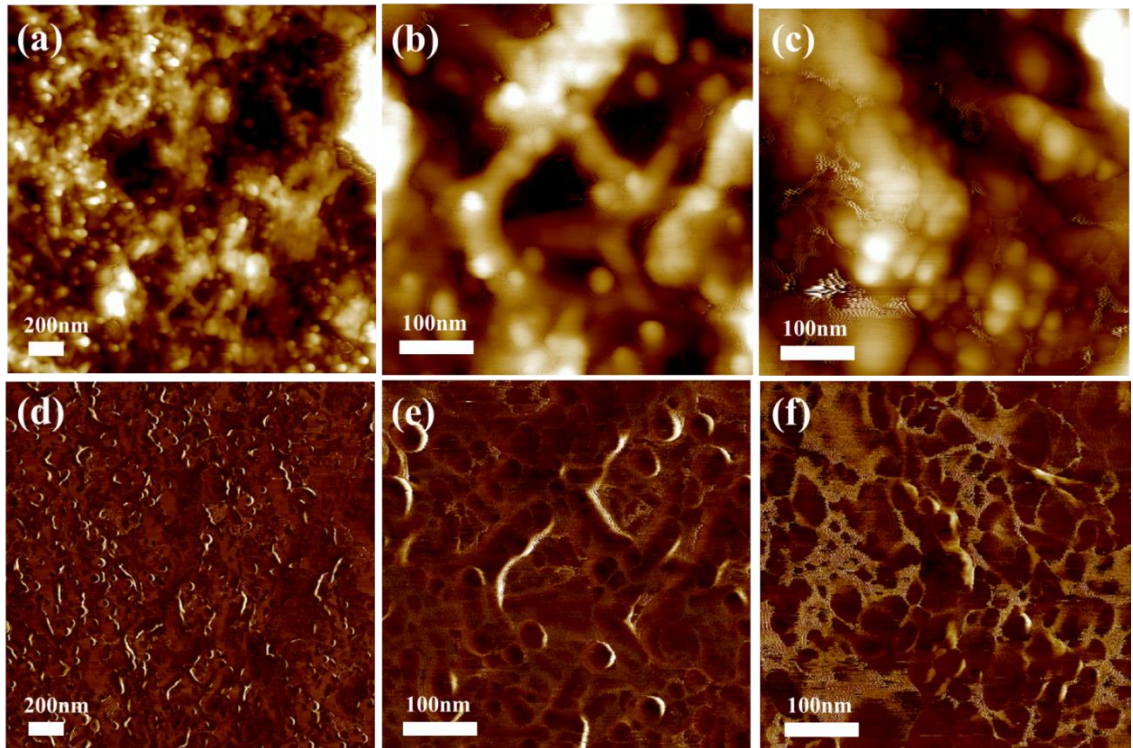


**Figure 5.12.** Morphologies of P3HT-CdSe tetrapod nanocomposites film. (a,d) Tapping mode AFM topographies and their corresponding phase images, (b,e) Close-up of CdSe tetrapods showing aggregated region, and (c,f) Close-up showing large domain area. Z-scale is 100 nm and 50 nm for (a) and (b,c), respectively.

**5.12b and 5.12d** as well as the large domains with size of around 200 nm (**Figure 5.12c and 5.12f**) were observed, indicating the phase separation between P3HT and CdSe tetrapods. We note that the observation of bare CdSe tetrapod implied the detachment of P3HT probably because of the depletion force. A further investigation will be required to fully understand this behavior, which will be the subject of future work.

#### 5.4. Conclusion

In summary, CdSe tetrapods were synthesized by CPI method through employing CdSe zincblende seeds, followed by surface modification with inorganic acid to effectively remove insulating ligands. A simple strategy for semiconducting P3HT–CdSe tetrapod nanocomposites was then explored by coupling ethynyl-terminated P3HT with azide-functionalized CdSe tetrapods via a catalyst-free click chemistry. The success of click reaction was confirmed by FTIR and  $^1\text{H}$  NMR measurements and photoluminescence spectroscopy. The nearly complete quenching in the emission of nanocomposites than the simple physical mixture suggested the efficient charge transfer at the P3HT/CdSe tetrapod interface. Solar cells based on these P3HT-CdSe tetrapod nanocomposites were fabricated to investigate the effect of the types of bifunctional ligands and the size of tetrapods on the device performance. It was found that the use of aryl bifunctional ligands was more effective than aliphatic ligands in terms of improving the device performance.

## 6. Stokes' shift engineered CdSe/ZnS core/shell QDs for solar concentrators

Jaehan Jung, Young jun Yoon, Sidney Malak, Chun Hao Lin, Ah-young Song, Vladimir Tsukruk, and Zhiqun Lin, "*Stokes' shift engineered CdSe/ZnS core/shell QDs*" (manuscript in preparation)

### 6.1. Introduction

Although we have focused on the crafting of CP-NC nanocomposites, it is also of key importance to explore the synthetic route to NCs and characterize their intriguing properties. In this Chapter, the alternative route to CdSe/ZnS core/shell nanostructures for solar concentrators and LED applications was discussed. Semiconductor quantum dots (QDs) in the strong confinement regime possess size dependent optical and electronic properties that open up new avenues for optoelectronic applications in solar cells<sup>23b</sup>, lasers<sup>89</sup>, solar concentrators<sup>90</sup>, LEDs<sup>5a, 91</sup>, optical amplifiers<sup>92</sup>, and bio-imaging<sup>93</sup>. Their solution processability owing to the presence of organic surfactants enables the easy incorporation of colloidal QDs into polymer or glass matrices, and thus paves a way for low-cost fabrication by serving as an ideal building block for optical devices. CdSe is an appealing inorganic semiconductor for optical application due to its optimum band gap (i.e., 1.74 eV) energy which enables the controlling of CdSe QD emission across all visible range.<sup>94</sup>

However, the utilization of CdSe QDs in opto-electronic devices is hindered by the

instability of optical properties resulted from the surface dangling bonds which act as nonradiative recombination sites. In order to address this problem, surface dangling bonds of CdSe QDs can be reduced by employing organic passivation. Surface modification of CdSe QDs with organic surfactants results in enhance luminescence efficiency as well as improves the photo- and colloidal stability.<sup>95</sup> However, the difficulty in covering all surfaces (i.e., anionic and cationic sites) with organic surfactant still leads to chemical degradation or photo-oxidation. In this context, inorganic surface passivation was introduced to cover all the surface of core QD efficiently, yielding core/shell architecture. For CdSe QDs, their surfaces were passivated either with ZnS or CdS to establish type I energy alignment system, where the band gap of CdSe lies within the band gap of shell material.

Although the surface trapping can be easily suppressed through passivation (e.g., inorganic shells or ligands passivation)<sup>96</sup>, Auger recombination rate depends significantly on the size of CdSe nanocrystals.<sup>8</sup> Hence, the utilization of bigger CdSe QDs or CdSe QDs with graded shell architecture can suppress Auger recombination rate which is non-radiative recombination process.<sup>97</sup> In this context, giant CdSe/CdS core/shell QDs (CdSe/CdS g-QDs) were prepared via a successive ion layer adsorption and reaction of monolayers (SILAR) method and were extensively studied as such structure can reduce the surface trapping effect as well as suppress Auger recombination.<sup>94, 97</sup> Moreover, they exhibit extensive “red shift” of emission peak which is indicative of extension of core wave function into the shell region (i.e., increasing the effective size of core).<sup>97</sup> The first absorption peak of CdSe/CdS g-QDs is also suppressed due to the primary absorption from CdS thick shell. However, achieving the re-absorption suppressed and Stokes’ shift

engineered CdSe/CdS g-QDs with emission position across the entire visible range is limited as the band gap of CdS (i.e., 2.42 eV or 512 nm) exceeds the wavelength of blue light. Moreover, a commonly used SILAR method to prepare g-QDs requires several time-consuming successive steps to epitaxially deposit the desired shell materials, thus demanding an alternative facile and robust synthesis route.

Herein, we report on a facile strategy to prepare highly luminescent CdSe/Cd<sub>1-x</sub>Zn<sub>x</sub>Se<sub>1-y</sub>S<sub>y</sub>/ZnS core/shell QDs with graded shell architecture. The passivation of chemical composition gradient Cd<sub>1-x</sub>Zn<sub>x</sub>Se<sub>1-y</sub>S<sub>y</sub> shell on as-prepared plain CdSe QDs ensures the stability of the resulting CdSe/Cd<sub>1-x</sub>Zn<sub>x</sub>Se<sub>1-y</sub>S<sub>y</sub>/ZnS QDs due to the alleviated lattice strain between CdSe and ZnS. Moreover, Stokes' shift can be engineered by simply controlling the thickness of ZnS shell (i.e., red-shifted), which was not observed in conventional CdSe/ZnS QDs owing to their larger energy level mismatch.<sup>98</sup> Notably, CdSe/Cd<sub>1-x</sub>Zn<sub>x</sub>Se<sub>1-y</sub>S<sub>y</sub>/ZnS QDs are advantageous over CdSe/CdS giant QDs since larger bandgap of ZnS than CdS provides more tunability for emission position in the visible region. Specifically, plain CdSe QDs with desired emission peak were synthesized and then passivated with Cd<sub>1-x</sub>Zn<sub>x</sub>Se<sub>1-y</sub>S<sub>y</sub> shell which has chemical composition gradient toward radial direction. This can be achieved by employing chemical reactivity difference in Zn and Cd precursors.<sup>99</sup> Further increase of ZnS shell thickness via secondary injection of sulfur precursors resulted in larger Stokes' shift as in giant CdSe/CdS QDs. The absorption and photoluminescence studies of CdSe/Cd<sub>1-x</sub>Zn<sub>x</sub>Se<sub>1-y</sub>S<sub>y</sub>/ZnS core/shell QDs revealed the dependence of emission peak position on the ZnS shell thickness. The size and shape of resulting QDs was examined using high resolution TEM.

## 6.2. Experimental

All chemical, including cadmium oxide, selenium, sulfur, and zinc acetylacetonate from Sigma Aldrich, Octadecene, tetradecyl phosphonic acid (TDPA, 97%), diethylzinc ( $\text{ZnEt}_2$ ), hexamethyldisilathiane ( $(\text{TMS})_2\text{S}$ ), oleic acid (OA), and trioctyl phosphine (TOP, 90%) from Alfa Aesar, and trioctyl phosphine oxide (TOPO, 90%) from Strem chemicals were used as received. All other organic solvents were purchased from VWR and used as received without further purification.

***Preparation of green emitting TDPA capped CdSe QDs:*** TDPA-capped CdSe QDs were synthesized according to literature.<sup>100</sup> A mixture of CdO (51 mg), TDPA (223 mg), and TOPO (3.777g) was degassed in a three neck flask for 1 hr at 120 °C. The temperature was then increased to 320 °C under Ar. Subsequently, 1M Se/TOP injection solution was prepared in a glovebox. After the solution turned clear and colorless, the temperature was set to 300 °C and then 1ml of injection solution was introduced to initiate the nucleation and growth. The heating mantle was removed to stop reaction after CdSe QDs were allowed to grow at 300 °C for 10 sec. 5 ml of hexane was added when the solution was cooled to 60 °C. The resulting TDPA-capped CdSe QDs were precipitated with methanol twice and then re-dispersed in chloroform.

***Preparation of red emitting CdSe QDs:*** High quality OA-capped red emitting CdSe QDs were prepared by slightly modifying the reported method.<sup>5a</sup> A mixture of CdO (1 mmol), OA (4 mmol), ODE (15 ml) were degassed in a three-neck flask for 1 hr at 120°C. After that temperature increased under Ar to 280 °C, where solution turned transparent. 0.5 ml of 1 M Se/TOP solution prepared in a glovebox was injected to

initiate the nucleation and growth. The heating mantle was removed to stop reaction after 5 min. Once temperature becomes 60 °C, 5 ml of hexane was added. The resulting OA-capped CdSe QDs were precipitated with methanol twice and then re-dispersed in desired solvent.

***Preparation of conventional CdSe/ZnS core/shell:*** CdSe/ZnS core/shell QDs were synthesized according to literature.<sup>96b</sup> Diethylzinc (ZnEt<sub>2</sub>) and hexamethyldisilathiane ((TMS)<sub>2</sub>S) were used as Zn and S sources respectively. First, 0.2 μ mol of TDPA-capped CdSe QDs were introduced as seed in 2g of HDA and 1g of TOPO and degassed at 120 °C for 1 hr. After that, temperature was elevated to 220 °C and 0.05 ml ZnEt<sub>2</sub> and 0.15 ml of (TMS)<sub>2</sub>S dissolved in 1ml of TOP were injected dropwisely. The heating mantle was removed to stop reaction after 60 min.

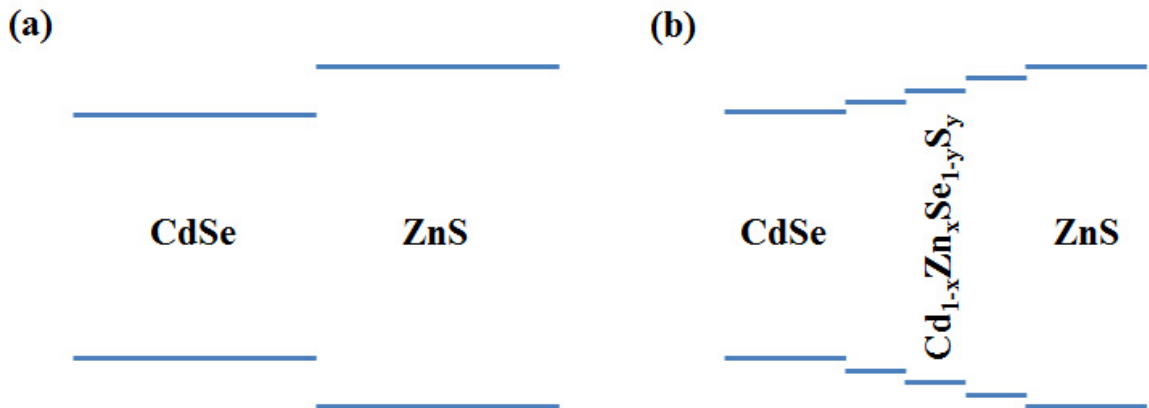
***Preparation of CdSe/ZnS core/shell with chemical composition gradient:*** 0.1 mmol of CdO, 4 mmol of Zn(acac)<sub>2</sub>, 5 ml of OA, and 15 ml of ODE were placed in a 150 ml three neck flask. The mixture was degassed at 120°C for 1hr. The temperature was then increased to 300°C under Ar. Subsequently, injection solution (0.1 mmol of Se and 4 mmol of S in 2 ml of TOP) was prepared in a glove box. After the solution turned transparent, the temperature was set to 250°C for emission red-shift or 300°C for emission blue-shift and 0.2 μmol CdSe core QDs were introduced. The prepared injection solution was added dropwisely. In order to change the shell thickness, 0.5 M S/TOP solution was added. The heating mantle was removed to stop reaction after 90 min.

***Characterization:*** The morphology of prepared CdSe QDs, CdSe/ZnS QDs, and CdSe/Cd<sub>1-x</sub>Zn<sub>x</sub>Se<sub>1-y</sub>S<sub>y</sub> QDs was imaged by high-resolution transmission electron

microscope (Tecnai F30). The absorption and emission spectra were recorded using a UV-vis spectrometer (UV-2600, Shimadzu) and a spectrofluorophotometer (RF-5301PC, Shimadzu), respectively.

### 6.3. Results and discussion

CdSe/Cd<sub>1-x</sub>Zn<sub>x</sub>Se<sub>1-y</sub>S<sub>y</sub>/ZnS core/shell QDs were synthesized by passivating ZnS shell with chemical composition gradient on the as-prepared CdSe QD core. The radial gradient shell was easily achieved by using the difference in chemical reactivity of cadmium and zinc precursors (i.e., Cd-oleate and Zn-oleate). Specifically, the weaker binding energy of Cd<sup>2+</sup> with oleic acid than Zn<sup>2+</sup> results in higher reactivity of Cd-oleate than Zn-oleate.<sup>99, 101</sup> Hence, formation of CdSe or CdS is more favorable than ZnSe or ZnS, thus resulting in Cd<sub>1-x</sub>Zn<sub>x</sub>Se<sub>1-y</sub>S<sub>y</sub> shell with gradual increase of Zn ratio over Cd. After Cd<sub>1-x</sub>Zn<sub>x</sub>Se<sub>1-y</sub>S<sub>y</sub> QDs were prepared, ZnS shell was further passivated on



**Scheme 6.1.** Energy alignment of (a) CdSe/ZnS QDs, and (b) CdSe/Cd<sub>1-x</sub>Zn<sub>x</sub>Se<sub>1-y</sub>S<sub>y</sub>/ZnS QDs.

$\text{Cd}_{1-x}\text{Zn}_x\text{Se}_{1-y}\text{S}_y$  QDs via secondary injection of sulfur precursors (i.e., Se/TOP), yielding CdSe/ $\text{Cd}_{1-x}\text{Zn}_x\text{Se}_{1-y}\text{S}_y$ /ZnS QDs. The energy level of resulting CdSe/ $\text{Cd}_{1-x}\text{Zn}_x\text{Se}_{1-y}\text{S}_y$ /ZnS QDs with chemical composition variation can be expected as the graded smooth alignment rather than sharp interface as in CdSe/ZnS QDs as depicted in **Scheme 6.1**. Especially, graded shell architecture can also reduce the lattice strain between CdSe and ZnS (i.e., 12%), otherwise, the interface strain which may occur and the trapping sites may accumulate dramatically with increasing shell thickness.<sup>94</sup>

Optical properties of as-prepared CdSe/ $\text{Cd}_{1-x}\text{Zn}_x\text{Se}_{1-y}\text{S}_y$ /ZnS QDs with chemical composition gradient shell and their comparison with conventional CdSe/ZnS QDs were explored by the absorption and photoluminescence measurements. In order to study the change in optical properties (i.e., the first absorption peak, emission peak, and QY), TDPA-capped plain CdSe QDs with the first absorption peak at 488 nm, emission peak at 500 nm, emission FWHM of 29 nm, and QY of 2.2% were selected and passivated with the graded shell (i.e.,  $\text{Cd}_{1-x}\text{Zn}_x\text{Se}_{1-y}\text{S}_y$ /ZnS) or ZnS shell, respectively. After the passivation of CdSe QDs core with  $\text{Cd}_{1-x}\text{Zn}_x\text{Se}_{1-y}\text{S}_y$  shell or ZnS shell, quantum yield enhanced (i.e., from 2.2% to 40% for CdSe/ $\text{Cd}_{1-x}\text{Zn}_x\text{Se}_{1-y}\text{S}_y$  QDs, and from 2.2% to 36.7% for CdSe/ZnS QDs, respectively) due to the reduction in surface dangling bonds as reported elsewhere.<sup>96</sup> The emission FWHM was maintained for both cases (i.e., around 30nm) as highly monodispersed TDPA-capped CdSe QDs core were employed as seeds. The emission peak position for both CdSe/ $\text{Cd}_{1-x}\text{Zn}_x\text{Se}_{1-y}\text{S}_y$  QDs and CdSe/ZnS QDs was shifted from 499 nm to 515 nm. This can be attributed to the increase in CdSe core size during the reaction due to the residue cadmium and selenium precursors.<sup>96b</sup> The change in the size of the resulting CdSe/ $\text{Cd}_{1-x}\text{Zn}_x\text{Se}_{1-y}\text{S}_y$  QDs was recorded using TEM, and the

diameter indeed increased from  $2.31 \pm 0.06$  nm to  $4.43 \pm 0.16$  nm (**Figure 6.2a and 6.2b**), clearly indicating the successful  $\text{Cd}_{1-x}\text{Zn}_x\text{Se}_{1-y}\text{S}_y$  shell passivation.

The thickness of ZnS shell was further increased to examine the evolution in emission and absorption properties of  $\text{CdSe}/\text{Cd}_{1-x}\text{Zn}_x\text{Se}_{1-y}\text{S}_y/\text{ZnS}$  QDs compared to those of traditional  $\text{CdSe}/\text{ZnS}$  QDs. Notably, the emission peak was further red-shifted (i.e., up to 550 nm) and first absorption peak was greatly suppressed, which was in sharp contrast to conventional  $\text{CdSe}/\text{ZnS}$  QDs without gradient shell (**Figure 6.1 and Table 6.1**). Specifically, when  $\text{CdSe}/\text{Cd}_{1-x}\text{Zn}_x\text{Se}_{1-y}\text{S}_y$  QDs were passivated with ZnS shell, yielding  $\text{CdSe}/\text{Cd}_{1-x}\text{Zn}_x\text{Se}_{1-y}\text{S}_y/\text{ZnS}$  QDs, the emission peak shifted from 515 nm to 543 nm. Increased ZnS shell thickness resulted in a further shift of emission position up to 550 nm. This was due possibly to the extended electron wave function into whole  $\text{CdSe}/\text{Cd}_{1-x}\text{Zn}_x\text{Se}_{1-y}\text{S}_y/\text{ZnS}$  QDs owing to the graded energy level alignment (**Scheme 6.1**), which is usually observed in  $\text{CdSe}/\text{CdS}$  QDs system since the energy level offset between CdSe and CdS is shallow.<sup>90,97</sup> Meanwhile, the principal absorption onset of  $\text{CdSe}/\text{Cd}_{1-x}\text{Zn}_x\text{Se}_{1-y}\text{S}_y/\text{ZnS}$  QDs was at around 400 nm, which was indicative of the ZnS bulk band gap. In contrast, the emission peak of  $\text{CdSe}/\text{ZnS}$  QDs remained at the same position (i.e., around 517 nm) regardless of the increased ZnS shell thickness. Traditional  $\text{CdSe}/\text{ZnS}$  QDs with different shell thickness as a control group were also prepared by simply changing the reaction time from 10 min to 90 min and the size of  $\text{CdSe}/\text{ZnS}$  QDs after a 90-min reaction was around 6.5 nm. Even  $\text{CdSe}/\text{ZnS}$  QDs with a diameter of 6.5 nm which corresponds to 7 monolayers of ZnS shell didn't exhibit the red-shift of emission peak. We note that a monolayer of ZnS is assumed to be the distance (i.e.,  $3.1 \text{ \AA}$ ) between consecutive planes along the [002] axis in bulk wurtzite ZnS.

**Table 6.1.** Optical properties of CdSe/ZnS QDs and CdSe/Cd<sub>1-x</sub>Zn<sub>x</sub>Se<sub>1-y</sub>S<sub>y</sub>/ZnS QDs

	Sample	Quantum yield	FWHM	Emission peak
Core	CdSe QDs (D=2.31 ± 0.06 nm)	2.2 %	29 nm	499 nm
Conventional	CdSe/ZnS QDs (10 min)	36.7 %	32 nm	515 nm
	CdSe/ZnS QDs (30 min)	32.2 %	33 nm	519 nm
	CdSe/ZnS QDs (90 min)	27.4 %	36 nm	517 nm
Graded shell	CdSe/Cd <sub>1-x</sub> Zn <sub>x</sub> Se <sub>1-y</sub> S <sub>y</sub> QDs (D=4.43 ± 0.16 nm)	40 %	32 nm	515 nm
	CdSe/Cd <sub>1-x</sub> Zn <sub>x</sub> Se <sub>1-y</sub> S <sub>y</sub> /ZnS QDs (D=5.96 ± 0.24 nm)	36.4 %	29 nm	543 nm
	CdSe/Cd <sub>1-x</sub> Zn <sub>x</sub> Se <sub>1-y</sub> S <sub>y</sub> /ZnS QDs (D=8.35 ± 0.35 nm)	34.2 %	29 nm	550 nm

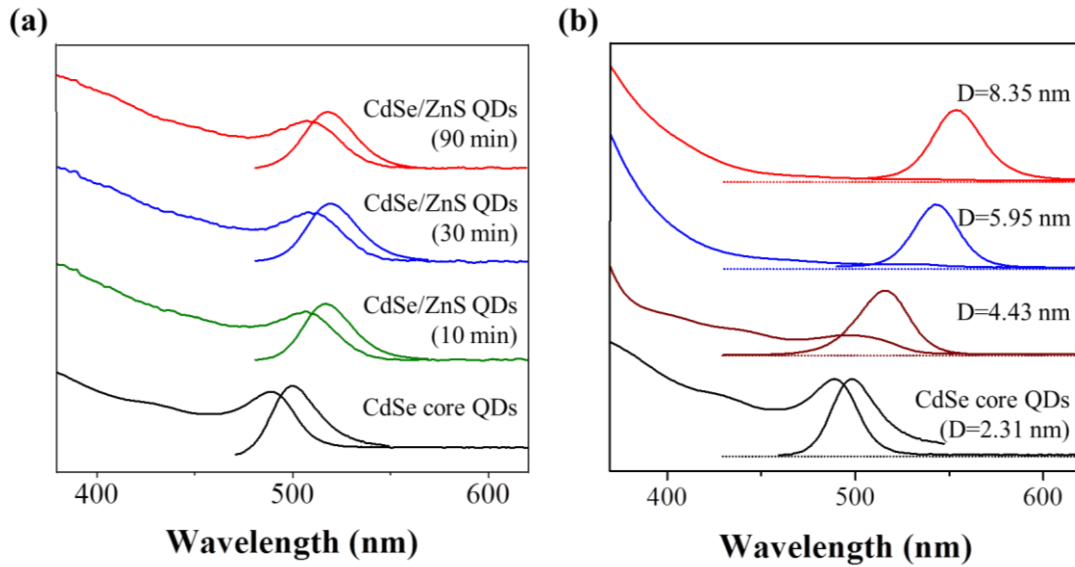


**Figure 6.1.** The absorption and emission spectra of (a) CdSe/ZnS QDs and (b) CdSe/Cd<sub>1-x</sub>Zn<sub>x</sub>Se<sub>1-y</sub>S<sub>y</sub>/ZnS QDs.

The sizes of CdSe QD core and the graded shell-covered CdSe/Cd<sub>1-x</sub>Zn<sub>x</sub>Se<sub>1-y</sub>S<sub>y</sub>/ZnS QDs were observed by TEM. CdSe core with 2.31±0.06 nm in diameter grew into CdSe/Cd<sub>1-x</sub>Zn<sub>x</sub>Se<sub>1-y</sub>S<sub>y</sub> QDs with 4.43±0.16 nm in diameter after passivation with Cd<sub>1-x</sub>Zn<sub>x</sub>Se<sub>1-y</sub>S<sub>y</sub> shell, indicating the successful surface passivation. The secondary injection of sulfur precursors led to the increase of the ZnS shell thickness, resulting in

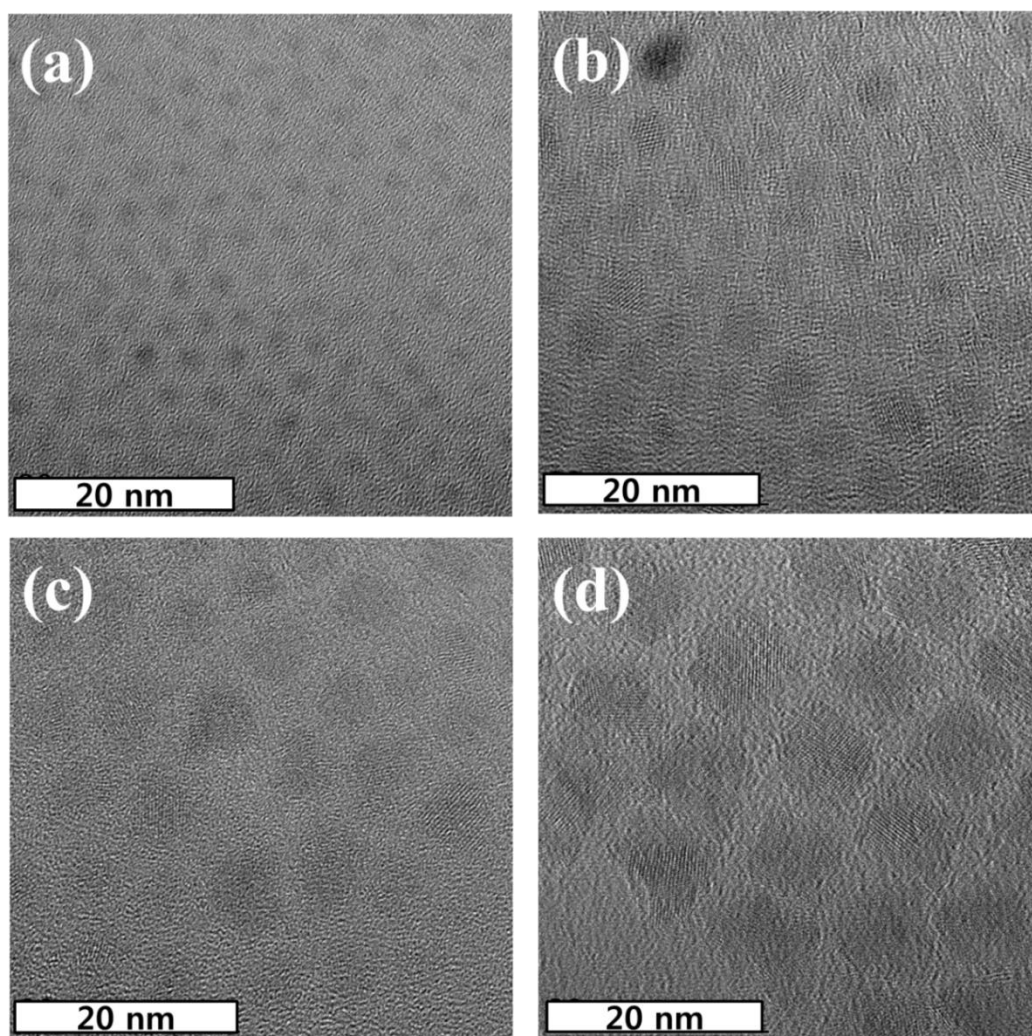


**Figure 6.2.** TEM images of (a) CdSe core QDs, (b) CdSe/Cd<sub>1-x</sub>Zn<sub>x</sub>Se<sub>1-y</sub>S<sub>y</sub> QDs, (c) CdSe/Cd<sub>1-x</sub>Zn<sub>x</sub>Se<sub>1-y</sub>S<sub>y</sub>/ZnS QDs (reacted for 30 min), and (d) CdSe/Cd<sub>1-x</sub>Zn<sub>x</sub>Se<sub>1-y</sub>S<sub>y</sub>/ZnS QDs (reacted for 90 min)

CdSe/Cd<sub>1-x</sub>Zn<sub>x</sub>Se<sub>1-y</sub>S<sub>y</sub>/ZnS QDs with a diameter of 5.96±0.24 nm, and eventually reached up to 8.35±0.35 nm as can be seen in **Figure 6.2**. The as-prepared CdSe/Cd<sub>1-x</sub>Zn<sub>x</sub>Se<sub>1-y</sub>S<sub>y</sub>/ZnS QDs also possessed high crystallinity. The increased diameter of QDs suggested the successful passivation of ZnS shell as well as possibly supported the delocalization of electron wave function in the whole CdSe/Cd<sub>1-x</sub>Zn<sub>x</sub>Se<sub>1-y</sub>S<sub>y</sub>/ZnS QDs, considering their emission red-shift, which was not observed in conventional CdSe/ZnS QDs without the compositional gradient due to the large energy mismatch between CdSe and ZnS. Therefore, larger Stokes' shift in CdSe/Cd<sub>1-x</sub>Zn<sub>x</sub>Se<sub>1-y</sub>S<sub>y</sub>/ZnS QDs compared to CdSe/ZnS QDs can be attributed to the increased effective core size through careful energy level engineering which enabling electron wave function extension into whole core/shell QDs while it was confined in CdSe QD core in the case of traditional CdSe/ZnS QDs.

Notably, CdSe/Cd<sub>1-x</sub>Zn<sub>x</sub>Se<sub>1-y</sub>S<sub>y</sub>/ZnS QDs exhibited improved photoluminescence stability under UV exposure as shown in **Figure 6.3**. After 60 min exposure to UV irradiation under air, the PL decayed only about 5% for chemical compositional CdSe/Cd<sub>1-x</sub>Zn<sub>x</sub>Se<sub>1-y</sub>S<sub>y</sub>/ZnS QDs, while the PL of conventional CdSe/ZnS QDs prepared with air-sensitive diethylzinc decreased up to 80%. It should also be noted that CdSe/Cd<sub>1-x</sub>Zn<sub>x</sub>Se<sub>1-y</sub>S<sub>y</sub>/ZnS QDs with gradient chemical composition were prepared using stable chemicals (i.e., Zinc acetate and sulfur powder). This is in contrast to conventional CdSe/ZnS QDs where reactive air-sensitive chemical is used (i.e., diethyl zinc and hexamethyldisilathiane). In this context, we have prepared CdSe/ZnS QDs without chemical composition gradient but using zinc acetate and sulfur powder in order to study if the improvement was resulted solely from chemical composition gradient. Intriguingly, the PL intensity dropped by 15 % after 60min of UV exposure. It is worth noting that the

red-emitting CdSe/ZnS QDs were used in this study to minimize the impact from the surface area/volume ratio as CdSe/Cd<sub>1-x</sub>Zn<sub>x</sub>Se<sub>1-y</sub>S<sub>y</sub>/ZnS QDs had relatively bigger size than conventional CdSe/ZnS QDs (**Figure 6.3**). The improved photo-stability of CdSe/Cd<sub>1-x</sub>Zn<sub>x</sub>Se<sub>1-y</sub>S<sub>y</sub>/ZnS QDs was due possibly to the relieved strain between CdSe and ZnS through the gradient structure, which enabled the enhanced surface capping of CdSe QD core. Otherwise, the intrinsic large lattice mismatch (~12%) would generate uncapped region of CdSe QD core.

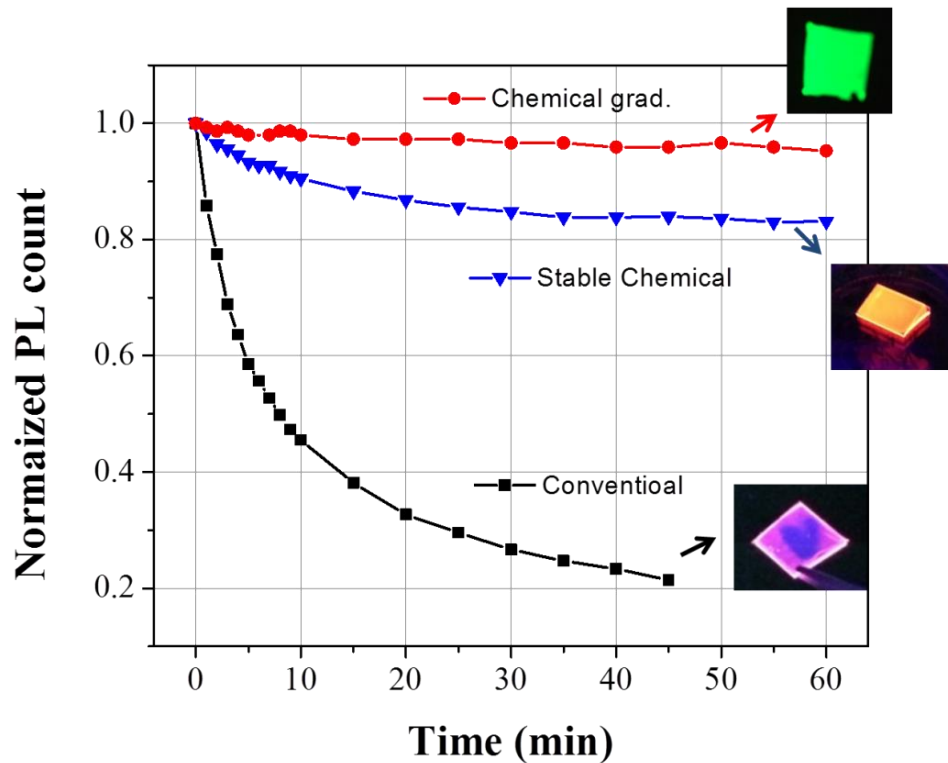


**Figure 6.3.** Normalized photoluminescence of conventional CdSe/ZnS QDs prepared by air-sensitive chemical (black) and stable chemicals (blue), and CdSe/Cd<sub>1-x</sub>Zn<sub>x</sub>Se<sub>1-y</sub>S<sub>y</sub>/ZnS QDs with chemical composition gradient prepared with stable chemicals (red), upon exposure to UV irradiation in air.

It is worth noting that CdSe/Cd<sub>1-x</sub>Zn<sub>x</sub>Se<sub>1-y</sub>S<sub>y</sub>/ZnS QDs prepared at higher temperature (i.e., at 300°C) showed a blue-shift in emission peak ( $\lambda_{em}$ ) (**Figure 6.4a**). When green-emitting CdSe QD core ( $\lambda_{em}$ =521 nm) was reacted with Cd, Zn, Se, and S precursors at 300°C for 10 min, the emission peak was blue-shifted from 521 nm to 518 nm. After reaction for another 90 min at 300°C with a secondary injection of sulfur, the emission position further shifted up to 513 nm regardless of the increase in diameter of the resulting CdSe/Cd<sub>1-x</sub>Zn<sub>x</sub>Se<sub>1-y</sub>S<sub>y</sub>/ZnS QDs (i.e.,  $9.46 \pm 0.25$  nm, **Figure 6.4b**). The resulting QDs exhibited pyramid-like shape which is commonly occurred when the fast reaction condition was utilized either by high precursor concentration or high temperature.<sup>23b, 88b</sup> This emission peak blue-shift regardless of increased QD size indicated that the electron wave function cannot be extended into whole

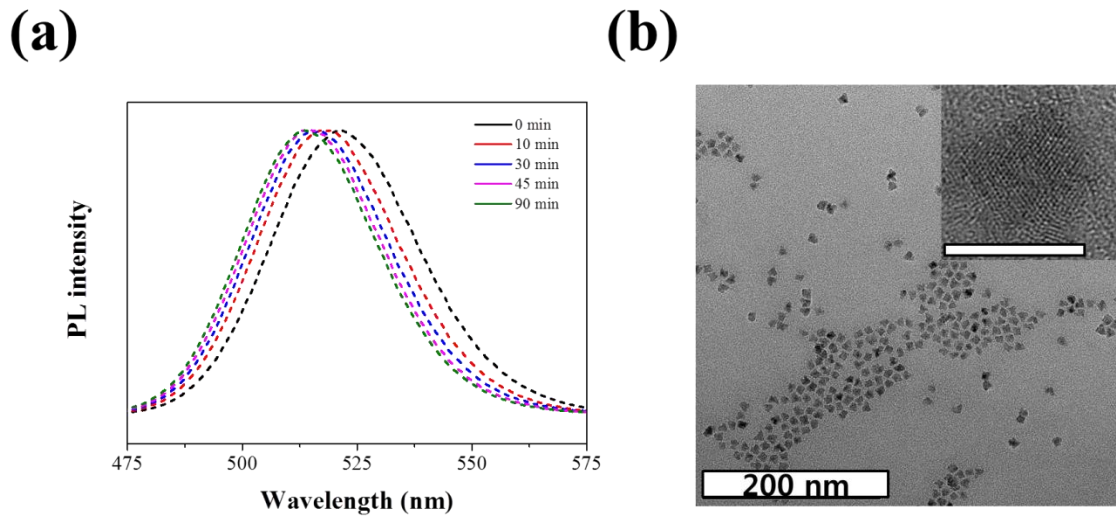


**Figure 6.4.** (a) Photoluminescence spectra of CdSe/Cd<sub>1-x</sub>Zn<sub>x</sub>Se<sub>1-y</sub>S<sub>y</sub>/ZnS QDs prepared at 300°C. (b) TEM image of CdSe/Cd<sub>1-x</sub>Zn<sub>x</sub>Se<sub>1-y</sub>S<sub>y</sub>/ZnS QDs after reaction at 300 °C for 90 min (Inset is HR TEM image, scale bar is 10 nm).

CdSe/Cd<sub>1-x</sub>Zn<sub>x</sub>Se<sub>1-y</sub>S<sub>y</sub>/ZnS QDs, unlike those prepared at 250 °C due possibly to the sharp energy level interface between CdSe and ZnS. It is also likely that the intradiffusion of Zn, Cd, Se, and S elements in QDs was facilitated at elevated temperature, and thus resulting in the alloying of CdSe QD core and increasing their band gap.<sup>102</sup>

The advantage of CdSe/Cd<sub>1-x</sub>Zn<sub>x</sub>Se<sub>1-y</sub>S<sub>y</sub>/ZnS QDs over CdSe/CdS QDs lies in the fact that core/shell QDs with emission across the entire visible range can be prepared due to the larger bulk band gap of ZnS (i.e., 3.54eV or 350 nm) compared to that of CdS (i.e., 2.42eV or 512 nm). However, this is limited in case of CdSe/CdS QDs system as the wavelength below 512 nm will be absorbed by CdS shell. Hence, careful control over the thickness and composition in graded shell may lead to blue- or green-emitting core/shell QDs with the suppressed reabsorption via larger Stokes' shift as the principal absorption onset for ZnS shell was below blue wavelength (i.e., 350 nm). Indeed, CdSe/Cd<sub>1-x</sub>Zn<sub>x</sub>Se<sub>1-y</sub>S<sub>y</sub>/ZnS QDs having different emission range with suppressed reabsorption can be prepared by simply utilizing CdSe core with different size (**Figure 6.5**). Specifically, plain green-emitting CdSe QDs of 2.31±0.06 and 2.5 nm (calculated from the first absorption peak ( $\lambda_{1st\ abs} = 520\text{ nm}$ ) of CdSe QDs<sup>95</sup>) were utilized as seeds to synthesize green- and yellow-emitting CdSe/Cd<sub>1-x</sub>Zn<sub>x</sub>Se<sub>1-y</sub>S<sub>y</sub>/ZnS QDs, respectively. CdSe QDs with diameter of 4.1 nm (calculated from  $\lambda_{1st\ abs} = 588\text{ nm}$ ) were used to prepare red-emitting CdSe/Cd<sub>1-x</sub>Zn<sub>x</sub>Se<sub>1-y</sub>S<sub>y</sub>/ZnS QDs. The diameter of the resulting green, yellow, and red QDs obtained from TEM analysis (**Figure 6.6**) were 8.35±0.25, 8.54±0.28, and 8.07±0.33 nm respectively.

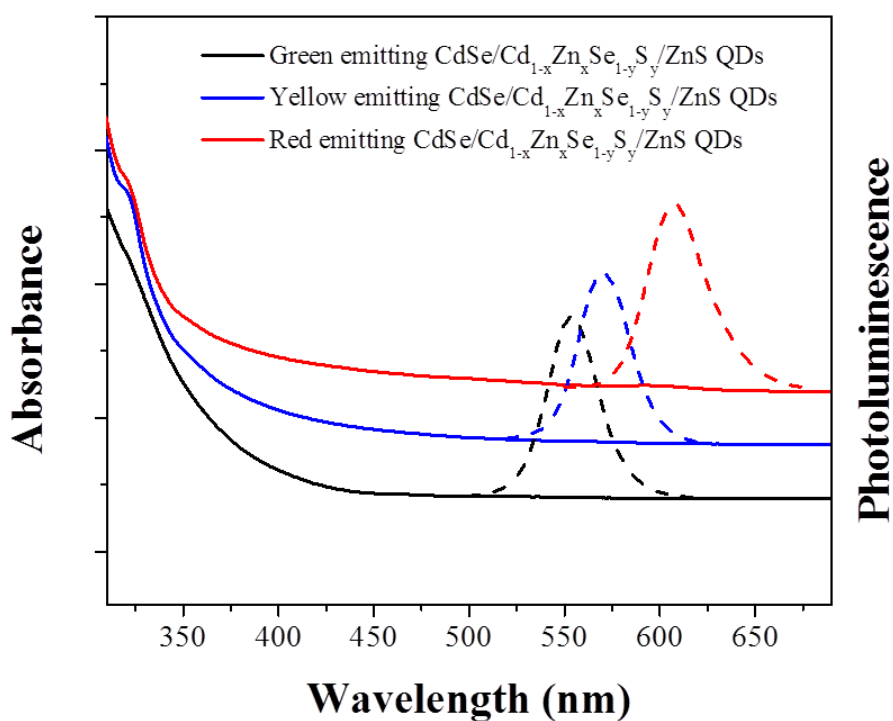


**Figure 6.5.** Absorption and photoluminescence spectra of as-prepared green-, yellow-, and red- emitting CdSe/Cd<sub>1-x</sub>Zn<sub>x</sub>Se<sub>1-y</sub>S<sub>y</sub>/ZnS QDs.

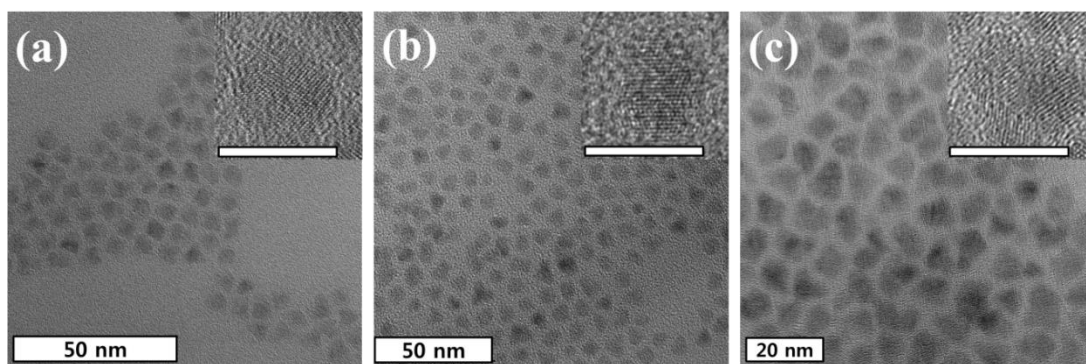


**Figure 6.6.** High-resolution TEM images of (a) green-, (b) yellow-, and (c) red-emitting CdSe/Cd<sub>1-x</sub>Zn<sub>x</sub>Se<sub>1-y</sub>S<sub>y</sub>/ZnS QDs. Inset are the magnified images; Scale bar = 10 nm.

#### 6.4. Conclusion

In summary,  $\text{Cd}_{1-x}\text{Zn}_x\text{Se}_{1-y}\text{S}_y/\text{ZnS}$  shell was passivated on CdSe QD surface in a one-pot process. The resulting QDs have tunable Stokes' shift as well as suppressed resorption through the control over the shell thickness. QDs with the emission in visible range and suppressed the first absorption can be achieved owing to the larger band gap of ZnS shell (the principal absorption onset of 400 nm). The dependence of the change in Stokes' shift and suppressed first absorption on the shell thickness in  $\text{CdSe}/\text{Cd}_{1-x}\text{Zn}_x\text{Se}_{1-y}\text{S}_y/\text{ZnS}$  QDs architecture was studied by UV-vis and PL spectroscopies and compared with conventional CdSe/ZnS QDs system. Unlike CdSe/ZnS QDs due to the continuous energy level change from CdSe to ZnS, the large red-shift of emission peak in  $\text{CdSe}/\text{Cd}_{1-x}\text{Zn}_x\text{Se}_{1-y}\text{S}_y/\text{ZnS}$  QDs was indicative of electron wavefunction delocalization in whole QDs. These Stokes' shift engineered  $\text{CdSe}/\text{Cd}_{1-x}\text{Zn}_x\text{Se}_{1-y}\text{S}_y/\text{ZnS}$  QDs may serve as promising materials for a wide range of applications, including LEDs, Lasers, and solar concentrator.

## 7. Conclusions and future work.

### 7.1. Conclusions

In this thesis, we developed robust synthetic routes to crafting CP-NC nanocomposites with the intimate contact between these two semiconducting constituents. These CP-NC nanocomposites were then employed as a photoactive layer in hybrid solar cells.

We have successfully prepared P3HT-CdSe NR nanocomposites via click chemistry between alkyne-terminated P3HT and azide-functionalized CdSe NRs, with no need for ligands exchange. Bifunctional ligands (i.e., BBPA or BrCH<sub>2</sub>-BA)-capped CdSe NRs were synthesized by precisely controlling the ratio between alkyl phosphonic acid ligands and short mobile bifunctional ligands to trigger the anisotropic growth. The ratio of these two ligands played significant role in controlling the shape of CdSe NCs due to the higher reactivity and mobility of Cd-BBPA (or Cd-BA-CH<sub>2</sub>Br) complexes compared to Cd-ODPA complexes. Similarly, cadmium telluride (CdTe) tetrapods were synthesized via multiple injections of the Te precursor by utilizing bifunctional ligands. Subsequently, tetrapod-shaped semiconducting inorganic-organic nanocomposites (i.e., P3HT-CdTe tetrapod nanocomposites) were produced by directly grafting conjugated polymer ethynyl-terminated poly(3-hexylthiophene) (i.e., P3HT-≡) onto azide-functionalized CdTe tetrapods (i.e., CdTe-N<sub>3</sub>) via a catalyst-free click chemistry. The intimate contact between P3HT and CdTe tetrapod rendered the effective dispersion of CdTe tetrapods in

nanocomposites, and facilitated their efficient electronic interaction. The success of coupling reaction was confirmed by Fourier transform infrared spectroscopy and nuclear magnetic resonance spectroscopy. The grafting density of P3HT chains on the CdTe tetrapods was estimated by thermogravimetric analysis. The photophysical properties of P3HT–CdTe tetrapod nanocomposites were studied using UV-Vis and photoluminescence spectroscopies. These intimate semiconducting conjugated polymer-tetrapod nanocomposites may offer a maximized interface between conjugated polymers and tetrapods for efficient charge separation, and enhanced charge transport regardless of their orientation for potential application in hybrid solar cells with improved power conversion efficiency. However, photovoltaic devices based on P3HT-CdSe NR nanocomposites exhibited rather low performance compared with other studies. We speculated that it was due possibly to the presence of residual insulating fatty ligands. This observation led to the exploration of inorganic acid treatments of NCs as follows.

P3HT-grafted CdSe tetrapods were successfully crafted by catalyst-free click coupling between azide-functionalized CdSe tetrapods and ethynyl-terminated P3HT after the surface modification of CdSe tetrapods through inorganic acid treatment. These intimate semiconductor P3HT-CdSe tetrapod nanocomposites was found to efficiently transfer electron from electron donating P3HT to electron accepting CdSe tetrapods as evidenced by photoluminescence measurement. Intriguingly, P3HT-CdSe tetrapod hybrid devices exhibited an improved performance compared to those devices fabricated without inorganic acid treatment, signifying the importance of the removal of residual insulating ligands which hindered charge carrier transport. The effects of the size of CdSe tetrapods and the types of bifunctional ligands (i.e., aryl or alkyl bifunctional ligands) on the device

performance were examined. Comparing 4-azidobenzoic acid with 5-bromovaleric acid bifunctional ligands, solar cells based on 4-azidobenzoic acid showed noticeably better performance, suggesting the effective charge transfer from molecules containing p-conjugated unit than aliphatic ligands. Moreover, it was found that the optimal size of CdSe tetrapods was required to balance the solubility and the electron transport.

In addition to the crafting of nanocomposites, we have also developed facile route to CdSe/Cd<sub>1-x</sub>Zn<sub>x</sub>Se<sub>1-y</sub>S<sub>y</sub>/ZnS QDs with enhanced optical properties. A graded Cd<sub>1-x</sub>Zn<sub>x</sub>Se<sub>1-y</sub>S<sub>y</sub> shell was passivated on plain CdSe QDs by simply utilizing chemical reactivity difference between cadmium oleate and zinc oleate (i.e., highly reactive cadmium-oleate reacts faster than zinc-oleate). Subsequently, zinc sulfide (ZnS) shell was further epitaxially grown through additional injection of precursors (i.e., S and Zn) to achieve unique optical properties. The surface passivation of plain CdSe QDs with a graded Cd<sub>1-x</sub>Zn<sub>x</sub>Se<sub>1-y</sub>S<sub>y</sub>/ZnS shell led to the enhanced optical properties (i.e., quantum yield). Moreover, the thicker ZnS shell resulted in red-shifted emission peak as well as the suppressed first peak absorption from the CdSe core, thereby reducing re-absorption, which have not been observed in conventional CdSe/ZnS QDs due to the larger energy level mismatch between CdSe and ZnS. Particularly, CdSe/Cd<sub>1-x</sub>Zn<sub>x</sub>Se<sub>1-y</sub>S<sub>y</sub>/ZnS QDs are advantageous over giant CdSe/CdS QDs as the larger bandgap of ZnS than CdS provides more tunability for the emission range. While giant CdSe/CdS QDs with suppressed reabsorption can only be achieved with the emission peak over 510 nm, it is feasible to produce reabsorption-suppressed CdSe/Cd<sub>1-x</sub>Zn<sub>x</sub>Se<sub>1-y</sub>S<sub>y</sub>/ZnS QDs with the emission even below 500 nm (i.e., up to 400 nm). The unique optical properties of CdSe/Cd<sub>1-x</sub>Zn<sub>x</sub>Se<sub>1-y</sub>S<sub>y</sub>/ZnS QDs were compared with conventional CdSe/ZnS QDs using UV-vis and

photoluminescence spectroscopy. These Stokes' shift engineered CdSe/Cd<sub>1-x</sub>Zn<sub>x</sub>Se<sub>1-y</sub>S<sub>y</sub>/ZnS QDs with suppressed re-absorption may serve as promising building blocks for optoelectronic applications, including lasers, LED, and solar concentrators.

In summary, we have rationally designed and crafted semiconductor CP-NC nanocomposites with intimate contacts between CP and NC via catalyst-free click chemistry and exploited them for photovoltaics. This facile methodology may assist in designing organic-inorganic nanocomposites with the direct contact for various applications, including solar cells.

## 7.2. Future work

Our P3HT-CdSe NR nanocomposites possess an intimate contact between the two semiconducting components, thus enabling efficient charge transfer from P3HT to CdSe NRs as confirmed by a transient absorption measurement conducted by our group from previous studies. Nonetheless, their use in photovoltaics was not satisfactory as shown in Chapter 3 due to the residue ligands. Moreover, spin-casting of P3HT-CdSe NR nanocomposites on the substrate did not take advantage of anisotropic nature of CdSe NRs that facilitate the direct pathway for charge transport along the long axis of CdSe NRs. Therefore, electron hopping process is still dominated among these CdSe NRs, as they laid parallel to the substrate, to reach electrodes. As the hopping process occurs, the current density drops dramatically, leading to the reduction of PCE. In this context, one may further explore the means of their assembly to form vertically aligned CdSe NRs. The vertically aligned geometry would allow for the full exploitation of the maximum

potential of NRs for use in solar cells.

Although P3HT-CdTe tetrapod nanocomposites have been successfully produced, their use in photovoltaics has not yet been investigated. As P3HT-CdTe tetrapod nanocomposites possess direct electron transfer from P3HT to CdTe tetrapods owing to their intimate contact, improved exciton dissociation resulted from maximized interfacial area between electron donating P3HT and electron accepting CdTe tetrapods, and enhanced electron transport to electrode due to their three dimensional elongated intrinsic structure, it will be interesting to employ them as photoactive layer for use in solar cells.

It was found that P3HT-CdSe tetrapod nanocomposites prepared with the surface modification of CdSe tetrapods using inorganic acid treatment can markedly improve the performance of the resulting organic-inorganic hybrid solar cells. However, the optimal condition for the best performance of solar cells is still lacking and merits a detailed study. The effect of P3HT molecular weight, the grafting density of P3HT, and the concentration of bifunctional ligands on the device performance may lead to some interesting and promising results. Finally, tuning the open circuit voltage by introducing bifunctional ligands with different dipole moment may also offer some feasibility to improve the performance.

We note that the synthetic strategy we developed for CP-NC nanocomposites is general and can be readily extend to graft different CPs onto a large variety of inorganic semiconducting NCs, creating a set of intriguing multifunctional nanomaterials for optoelectronic applications.

## References

1. Milliron, D. J.; Gur, I.; Alivisatos, A. P., Hybrid organic-nanocrystal solar cells *MRS Bull.* **2005**, *30*, 41-44.
2. Thompson, B. C.; Frechet, J. M. J., Organic photovoltaics - Polymer-fullerene composite solar cells. *Angew. Chem. Int. Ed.* **2008**, *47* (1), 58-77.
3. Xu, J.; Wang, J.; Mitchell, M.; Mukherjee, P.; Jeffries-EL, M.; Petrich, J. W.; Lin, Z. Q., Organic-inorganic nanocomposites via directly grafting conjugated polymers onto quantum dots. *J. Am. Chem. Soc.* **2007**, *129*, 12828.
4. Kang, Y. M.; Park, N. G.; Kim, D. W., Hybrid solar cells with vertically aligned CdTe nanorods and a conjugated polymer. *Appl. Phys. Lett.* **2005**, *86*, 113101-1-113101-3.
5. (a) Sun, Q.; Wang, Y. A.; Li, L. S.; Wang, D.; Zhu, T.; Xu, J.; Yang, C.; Li, Y., Bright, multicoloured light-emitting diodes based on quantum dots. *Nat Photon* **2007**, *1* (12), 717-722; (b) Lin, Z. Q., Organic-inorganic nanohybrids via direct tailoring semiconductor nanocrystals with conjugated polymers. *Chem. --Eur. J.* **2008**, *14*, 6294-6301; (c) Coakley, K. M.; McGehee, M. D., Conjugated Polymer Photovoltaic Cells. *Chem. Mater.* **2004**, *16* (23), 4533-4542; (d) He, M.; Qiu, F.; Lin, Z., Conjugated rod-coil and rod-rod block copolymers for photovoltaic applications. *J. Mater. Chem.* **2011**, *21* 170239-17048; (e) He, M.; Han, W.; Ge, J.; Yu, W.; Yang, Y. L.; Qiu, F.; Lin, Z., Annealing effects on the photovoltaic performance of all-conjugated poly(3-alkylthiophene) diblock copolymer-based bulk heterojunction solar cells. *Nanoscale* **2011**, *3*, 3159-3163.
6. (a) Kim, Y.; Cook, S.; Tuladhar, S. M.; Choulis, S. A.; Nelson, J.; Durrant, J. R.; Bradley, D. D. C.; Giles, M.; McCulloch, I.; Ha, C.-S.; Ree, M., A strong regioregularity effect in self-organizing conjugated polymer films and high-efficiency polythiophene:fullerene solar cells. *Nat. Mater.* **2006**, *5* (3), 197-203; (b) Sirringhaus, H.; Tessler, N.; Friend, R. H., Integrated Optoelectronic Devices Based on Conjugated Polymers. *Science* **1998**, *280* (5370), 1741-1744.
7. (a) Huynh, W. U.; Dittmer, J. J.; Alivisatos, A. P., Hybrid Nanorod-Polymer Solar Cells. *Science* **2002**, *295* (5564), 2425-2427; (b) Zhou, Y.; Riehle, F. S.; Yuan, Y.; Schleiermacher, H.-F.; Niggemann, M.; Urban, G. A.; Kruger, M., Improved efficiency of hybrid solar cells based on non-ligand-exchanged CdSe quantum dots and poly(3-hexylthiophene). *Appl. Phys. Lett.* **2010**, *96* (1), 013304-1-013304-3; (c) Dayal, S.; Kopidakis, N.; Olson, D. C.; Ginley, D. S.; Rumbles, G., Photovoltaic Devices with a Low Band Gap Polymer and CdSe Nanostructures Exceeding 3% Efficiency. *Nano Lett.* **2009**, *10* (1), 239-242; (d) Sun, B.; Snaith, H. J.; Dhoot, A. S.; Westenhoff, S.; Greenham, N. C., Vertically segregated hybrid blends for photovoltaic devices with improved efficiency. *J. Appl. Phys.* **2005**, *97* (1), 014914-1-014914-6.
8. Greenham, N. C.; Peng, X.; Alivisatos, A. P., Charge separation and transport in conjugated-polymer/semiconductor-nanocrystal composites studied by photoluminescence quenching and photoconductivity. *Phys. Rev. B* **1996**, *54* (24), 17628-17637.
9. (a) Zhao, L.; Lin, Z., Crafting semiconductor organic-inorganic nanocomposites via placing conjugated polymers in intimate contact with nanocrystals for hybrid solar cells. *Adv. Mater.* **2012**, *24*, 4353-4368; (b) Zhao, L.; Pang, X.; Adhikary, R.; J. Petrich; Jeffries-EL, M.; Lin, Z., Organic-inorganic nanocomposites by placing conjugated polymers in intimate contact with quantum rods. *Adv. Mater.* **2011**, *23*, 2844-2849; (c) Zhao, L.; Pang, X.; Adhikary, R.; J. Petrich; Lin, Z., Semiconductor anisotropic nanocomposites obtained by directly coupling conjugated polymers with quantum rods. *Angew. Chem., Int.*

*Ed.* **2011**, *50*, 3958-3962.

10. Ji, X.; Copenhaver, D.; Sichmeller, C.; Peng, X., Ligand Bonding and Dynamics on Colloidal Nanocrystals at Room Temperature: The Case of Alkylamines on CdSe Nanocrystals. *J. Am. Chem. Soc.* **2008**, *130* (17), 5726-5735.

11. (a) Kim, J. Y.; Lee, K.; Coates, N. E.; Moses, D.; Nguyen, T.-Q.; Dante, M.; Heeger, A. J., Efficient Tandem Polymer Solar Cells Fabricated by All-Solution Processing. *Science* **2007**, *317* (5835), 222-225; (b) Ma, W.; Yang, C.; Gong, X.; Lee, K.; Heeger, A. J., Thermally Stable, Efficient Polymer Solar Cells with Nanoscale Control of the Interpenetrating Network Morphology. *Adv. Funct. Mater.* **2005**, *15* (10), 1617-1622.

12. Zhao, L.; Lin, Z., Crafting Semiconductor Organic-Inorganic Nanocomposites via Placing Conjugated Polymers in Intimate Contact with Nanocrystals for Hybrid Solar Cells. *Adv. Mater.* **2012**, *24* (32), 4353-4368.

13. Li, G.; Shrotriya, V.; Huang, J. S.; Yao, Y.; Moriarty, T.; Emery, K.; Yang, Y., High-efficiency solution processable polymer photovoltaic cells by self-organization of polymer blends. *Nat. Mater.* **2005**, *4* (11), 864-868.

14. Scharber, M. C.; Wuhlbacher, D.; Koppe, M.; Denk, P.; Waldauf, C.; Heeger, A. J.; Brabec, C. L., Design rules for donors in bulk-heterojunction solar cells - Towards 10 % energy-conversion efficiency. *Adv. Mater.* **2006**, *18* (6), 789-+.

15. (a) Hoppe, H.; Sariciftci, N. S., Morphology of polymer/fullerene bulk heterojunction solar cells. *J. Mater. Chem.* **2006**, *16* (1), 45-61; (b) Blom, P. W. M.; Mihailetchi, V. D.; Koster, L. J. A.; Markov, D. E., Device physics of polymer : fullerene bulk heterojunction solar cells. *Adv. Mater.* **2007**, *19* (12), 1551-1566; (c) Campoy-Quiles, M.; Ferenczi, T.; Agostinelli, T.; Etchegoin, P. G.; Kim, Y.; Anthopoulos, T. D.; Stavrinou, P. N.; Bradley, D. D. C.; Nelson, J., Morphology evolution via self-organization and lateral and vertical diffusion in polymer: fullerene solar cell blends. *Nat. Mater.* **2008**, *7* (2), 158-164.

16. (a) Park, S. H.; Roy, A.; Beaupre, S.; Cho, S.; Coates, N.; Moon, J. S.; Moses, D.; Leclerc, M.; Lee, K.; Heeger, A. J., Bulk heterojunction solar cells with internal quantum efficiency approaching 100%. *Nat. Photon.* **2009**, *3* (5), 297-302; (b) Liang, Y.; Xu, Z.; Xia, J.; Tsai, S.-T.; Wu, Y.; Li, G.; Ray, C.; Yu, L., For the Bright Future—Bulk Heterojunction Polymer Solar Cells with Power Conversion Efficiency of 7.4%. *Adv. Mater.* **2010**, *22* (20), E135-E138.

17. (a) Gur, I.; Fromer, N. A.; Geier, M. L.; Alivisatos, A. P., Air-stable all-inorganic nanocrystal solar cells processed from solution. *Science* **2005**, *310*, 462; (b) Goodman, M. D.; Xu, J.; Wang, J.; Lin, Z. Q., Semiconductor conjugated polymer-quantum dot nanocomposites at the air/water interface and their photovoltaic performance. *Chem. Mater.* **2009**, *21*, 934

; (c) Xu, J.; Xia, J.; Lin, Z. Q., Evaporation-induced self-assembly of nanoparticles from a sphere-on-flat geometry. *Angew. Chem. Int. Ed.* **2007**, *46*, 1860-1863.

18. Colvin, V. L.; Schlamp, M. C.; Alivisatos, A. P., Light-emitting diodes made from cadmium selenide nanocrystals and a semiconducting polymer. *Nature* **1994**, *370*, 354.

19. Klimov, V. I.; Mikhailovsky, A. A.; Xu, S.; Malko, A.; Hollingsworth, J. A.; Leatherdale, C. A.; Eisler, H. J.; Bawendi, M. G., Optical gain and stimulated emission in nanocrystal quantum dots. *Science* **2000**, *290*, 314.

20. (a) Chan, W. C. W.; Nie, S., Quantum dot bioconjugates for ultrasensitive nonisotopic detection. *Science* **1998**, *281*, 2016; (b) Medintz, I. L.; Uyeda, H. T.; Goldman, E. R.; Mattoussi, H., Quantum dot bioconjugates for imaging, labelling and sensing. *Nat. Mater.* **2005**, *4*, 435-446.
21. Alivisatos, A. P., The use of nanocrystals in biological detection. *Nat. Biotechnol.* **2004**, *22*, 47-52.
22. (a) Yu, D.; Wang, C.; Guyot-Sionnest, P., n-Type Conducting CdSe Nanocrystal Solids. *Science* **2003**, *300* (5623), 1277-1280; (b) Talgorn, E.; Abellon, R. D.; Kooyman, P. J.; Piris, J.; Savenije, T. J.; Goossens, A.; Houtepen, A. J.; Siebbeles, L. D. A., Supercrystals of CdSe Quantum Dots with High Charge Mobility and Efficient Electron Transfer to TiO<sub>2</sub>. *ACS Nano* **2010**, *4* (3), 1723-1731; (c) Rode, D. L., Electron Mobility in II-VI Semiconductors. *Phys. Rev. B* **1970**, *2* (10), 4036-4044; (d) Skompska, M., Hybrid conjugated polymer/semiconductor photovoltaic cells. *Synth. Met.* **2010**, *160* (1-2), 1-15; (e) Wright, M.; Uddin, A., Organic-inorganic hybrid solar cells: A comparative review. *Sol Energ Mat Sol C* **2012**, *107*, 87-111; (f) Wang, X. F.; Song, W. F.; Liu, B.; Chen, G.; Chen, D.; Zhou, C. W.; Shen, G. Z., High-Performance Organic-Inorganic Hybrid Photodetectors Based on P3HT:CdSe Nanowire Heterojunctions on Rigid and Flexible Substrates. *Adv. Funct. Mater.* **2013**, *23* (9), 1202-1209; (g) Seo, J. H.; Kim, D. H.; Kwon, S. H.; Song, M.; Choi, M. S.; Ryu, S. Y.; Lee, H. W.; Park, Y. C.; Kwon, J. D.; Nam, K. S.; Jeong, Y.; Kang, J. W.; Kim, C. S., High Efficiency Inorganic/Organic Hybrid Tandem Solar Cells. *Adv. Mater.* **2012**, *24* (33), 4523-4527; (h) Peng, X. G.; Manna, L.; Yang, W. D.; Wickham, J.; Scher, E.; Kadavanich, A.; Alivisatos, A. P., Shape control of CdSe nanocrystals. *Nature* **2000**, *404* (6773), 59-61; (i) Yin, Y.; Alivisatos, A. P., Colloidal nanocrystal synthesis and the organic-inorganic interface. *Nature* **2005**, *437* (7059), 664-670.
23. (a) Zhao, L.; Pang, X.; Adhikary, R.; Petrich, J. W.; Jeffries-El, M.; Lin, Z., Organic-Inorganic Nanocomposites by Placing Conjugated Polymers in Intimate Contact with Quantum Rods. *Adv. Mater.* **2011**, *23* (25), 2844-2849; (b) Jung, J.; Pang, X.; Feng, C.; Lin, Z., Semiconducting Conjugated Polymer-Inorganic Tetrapod Nanocomposites. *Langmuir* **2013**, *29* (25), 8086-8092; (c) Liao, H.-C.; Chen, S.-Y.; Liu, D.-M., In-Situ Growing CdS Single-Crystal Nanorods via P3HT Polymer as a Soft Template for Enhancing Photovoltaic Performance. *Macromolecules* **2009**, *42* (17), 6558-6563; (d) Dayal, S.; Kopidakis, N.; Olson, D. C.; Ginley, D. S.; Rumbles, G., Direct Synthesis of CdSe Nanoparticles in Poly(3-hexylthiophene). *J. Am. Chem. Soc.* **2009**, *131* (49), 17726-17727; (e) Zhao, L.; Lin, Z. Q., Crafting Semiconductor Organic-Inorganic Nanocomposites by Placing Conjugated Polymers in Intimate Contact with Nanocrystals for Hybrid Solar Cells. *Adv. Mater.* **2012**, *24* (32), 4353-4368; (f) Zhao, L.; Pang, X. C.; Adhikary, R.; Petrich, J. W.; Jeffries-EL, M.; Lin, Z. Q., Organic-Inorganic Nanocomposites by Placing Conjugated Polymers in Intimate Contact with Quantum Rods. *Adv. Mater.* **2011**, *23* (25), 2844-2849.
24. (a) Wu, J.-L.; Chen, F.-C.; Hsiao, Y.-S.; Chien, F.-C.; Chen, P.; Kuo, C.-H.; Huang, M. H.; Hsu, C.-S., Surface Plasmonic Effects of Metallic Nanoparticles on the Performance of Polymer Bulk Heterojunction Solar Cells. *ACS Nano* **2011**, *5* (2), 959-967; (b) Baek, S.-W.; Park, G.; Noh, J.; Cho, C.; Lee, C.-H.; Seo, M.-K.; Song, H.; Lee, J.-Y., Au@Ag Core-Shell Nanocubes for Efficient Plasmonic Light Scattering Effect in Low Bandgap Organic Solar Cells. *ACS Nano* **2014**, *8*, 3302-3312.
25. (a) Agranovich, V.; Benisty, H.; Weisbuch, C., Organic and inorganic quantum wells in a microcavity: Frenkel-Wannier-Mott excitons hybridization and energy transformation. *Solid State Commun.* **1997**, *102* (8), 631-636; (b) Malyshev, V.; Moreno, P., Hidden structure of the low-energy spectrum of a one-dimensional localized Frenkel exciton. *Phys. Rev. B* **1995**, *51* (20), 14587-14593.
26. (a) Lunt, R. R.; Giebink, N. C.; Belak, A. A.; Benziger, J. B.; Forrest, S. R., Exciton diffusion lengths of organic semiconductor thin films measured by spectrally resolved photoluminescence quenching. *J. Appl. Phys.* **2009**, *105* (5), 053711; (b) Mikhnenko, O. V.; Cordella, F.; Sieval, A. B.; Hummelen, J. C.; Blom, P. W. M.; Loi, M. A., Temperature Dependence of Exciton Diffusion in Conjugated Polymers. *J. Phys. Chem. B* **2008**, *112* (37), 11601-11604; (c) Yun-Yue, L.; Chun-Wei, C.; Chang, J.; Lin, T. Y.; Liu, I. S.; Wei-Fang, S., Exciton dissociation and migration in enhanced order conjugated polymer/nanoparticle

hybrid materials. *Nanotechnology* **2006**, *17* (5), 1260.

27. (a) Li, Y. F., Molecular Design of Photovoltaic Materials for Polymer Solar Cells: Toward Suitable Electronic Energy Levels and Broad Absorption. *Accounts Chem Res* **2012**, *45* (5), 723-733; (b) Zhou, H. X.; Yang, L. Q.; You, W., Rational Design of High Performance Conjugated Polymers for Organic Solar Cells. *Macromolecules* **2012**, *45* (2), 607-632; (c) Janssen, R. A. J.; Nelson, J., Factors Limiting Device Efficiency in Organic Photovoltaics. *Adv. Mater.* **2013**, *25* (13), 1847-1858.

28. Sariciftci, N. S.; Smilowitz, L.; Heeger, A. J.; Wudl, F., Photoinduced Electron-Transfer from a Conducting Polymer to Buckminsterfullerene. *Science* **1992**, *258* (5087), 1474-1476.

29. Shrotriya, V.; Wu, E. H. E.; Li, G.; Yao, Y.; Yang, Y., Efficient light harvesting in multiple-device stacked structure for polymer solar cells. *Appl. Phys. Lett.* **2006**, *88* (6), 064104.

30. He, M.; Han, W.; Ge, J.; Yang, Y. L.; Qiu, F.; Lin, Z. Q., All-conjugated poly(3-alkylthiophene) diblock copolymer-based bulk heterojunction solar cells with controlled molecular organization and nanoscale morphology. *Energy Environ. Sci.* **2011**, *4* (8), 2894-2902.

31. Kim, Y.; Cook, S.; Tuladhar, S. M.; Choulis, S. A.; Nelson, J.; Durrant, J. R.; Bradley, D. D. C.; Giles, M.; McCulloch, I.; Ha, C. S.; Ree, M., A strong regioregularity effect in self-organizing conjugated polymer films and high-efficiency polythiophene: fullerene solar cells. *Nat. Mater.* **2006**, *5* (3), 197-203.

32. Narayan, M. R.; Singh, J., Study of the mechanism and rate of exciton dissociation at the donor-acceptor interface in bulk-heterojunction organic solar cells. *J. Appl. Phys.* **2013**, *114* (7), 073510.

33. (a) Zou, Y. P.; Najari, A.; Berrouard, P.; Beaupre, S.; Aich, B. R.; Tao, Y.; Leclerc, M., A Thieno[3,4-c]pyrrole-4,6-dione-Based Copolymer for Efficient Solar Cells. *J. Am. Chem. Soc.* **2010**, *132* (15), 5330-+; (b) Liang, Y. Y.; Yu, L. P., A New Class of Semiconducting Polymers for Bulk Heterojunction Solar Cells with Exceptionally High Performance. *Accounts Chem Res* **2010**, *43* (9), 1227-1236; (c) Koizumi, Y.; Ide, M.; Saeki, A.; Vijayakumar, C.; Balan, B.; Kawamoto, M.; Seki, S., Thienoisindigo-based low-band gap polymers for organic electronic devices. *Polym Chem-Uk* **2013**, *4* (3), 484-494; (d) Zhong, H. L.; Li, Z.; Deledalle, F.; Fregoso, E. C.; Shahid, M.; Fei, Z. P.; Nielsen, C. B.; Yaacobi-Gross, N.; Rossbauer, S.; Anthopoulos, T. D.; Durrant, J. R.; Heeney, M., Fused Dithienogermolodithiophene Low Band Gap Polymers for High-Performance Organic Solar Cells without Processing Additives. *J. Am. Chem. Soc.* **2013**, *135* (6), 2040-2043.

34. Zhou, R. J.; Stalder, R.; Xie, D. P.; Cao, W. R.; Zheng, Y.; Yang, Y. X.; Plaisant, M.; Holloway, P. H.; Schanze, K. S.; Reynolds, J. R.; Xue, J. G., Enhancing the Efficiency of Solution-Processed Polymer:Colloidal Nanocrystal Hybrid Photovoltaic Cells Using Ethanedithiol Treatment. *ACS Nano* **2013**, *7* (6), 4846-4854.

35. Zhou, E.; Cong, J.; Wei, Q.; Tajima, K.; Yang, C.; Hashimoto, K., All-Polymer Solar Cells from Perylene Diimide Based Copolymers: Material Design and Phase Separation Control. *Angew. Chem. Int. Ed.* **2011**, *50* (12), 2799-2803.

36. Yan, H.; Chen, Z.; Zheng, Y.; Newman, C.; Quinn, J. R.; Dotz, F.; Kastler, M.; Facchetti, A., A high-mobility electron-transporting polymer for printed transistors. *Nature* **2009**, *457* (7230), 679-686.

37. Moore, J. R.; Albert-Seifried, S.; Rao, A.; Massip, S.; Watts, B.; Morgan, D. J.; Friend, R. H.; McNeill, C. R.; Sirringhaus, H., Polymer Blend Solar Cells Based on a High-Mobility Naphthalenediimide-Based Polymer Acceptor: Device Physics, Photophysics and Morphology. *Adv. Eng. Mater.* **2011**, *1* (2), 230-240.

38. Earmme, T.; Hwang, Y.-J.; Murari, N. M.; Subramaniyan, S.; Jenekhe, S. A., All-Polymer Solar Cells with 3.3% Efficiency Based on Naphthalene Diimide-Selenophene Copolymer Acceptor. *J. Am. Chem. Soc.* **2013**, *135* (40), 14960-14963.
39. Stalder, R.; Mei, J.; Subbiah, J.; Grand, C.; Estrada, L. A.; So, F.; Reynolds, J. R., n-Type Conjugated Polyisoindigos. *Macromolecules* **2011**, *44* (16), 6303-6310.
40. Walker, B.; Tamayo, A. B.; Dang, X.-D.; Zalar, P.; Seo, J. H.; Garcia, A.; Tantiwivat, M.; Nguyen, T.-Q., Nanoscale Phase Separation and High Photovoltaic Efficiency in Solution-Processed, Small-Molecule Bulk Heterojunction Solar Cells. *Adv. Funct. Mater.* **2009**, *19* (19), 3063-3069.
41. Sun, Y.; Welch, G. C.; Leong, W. L.; Takacs, C. J.; Bazan, G. C.; Heeger, A. J., Solution-processed small-molecule solar cells with 6.7% efficiency. *Nat. Mater.* **2012**, *11* (1), 44-48.
42. Bagnis, D.; Beverina, L.; Huang, H.; Silvestri, F.; Yao, Y.; Yan, H.; Pagani, G. A.; Marks, T. J.; Facchetti, A., Marked Alkyl- vs Alkenyl-Substituent Effects on Squaraine Dye Solid-State Structure, Carrier Mobility, and Bulk-Heterojunction Solar Cell Efficiency. *J. Am. Chem. Soc.* **2010**, *132* (12), 4074-4075.
43. (a) Wang, L.; Liu, Y.; Jiang, X.; Qin, D.; Cao, Y., Enhancement of Photovoltaic Characteristics Using a Suitable Solvent in Hybrid Polymer/Multiarmed CdS Nanorods Solar Cells. *J. Phys. Chem. C* **2007**, *111* (26), 9538-9542; (b) Dowland, S.; Lutz, T.; Ward, A.; King, S. P.; Sudlow, A.; Hill, M. S.; Molloy, K. C.; Haque, S. A., Direct Growth of Metal Sulfide Nanoparticle Networks in Solid-State Polymer Films for Hybrid Inorganic–Organic Solar Cells. *Adv. Mater.* **2011**, *23* (24), 2739-2744.
44. (a) Xu, J.; Xia, J. F.; Wang, J.; Shinar, J.; Lin, Z. Q., Quantum dots confined in nanoporous alumina membranes. *Appl. Phys. Lett.* **2006**, *89*, 133110; (b) Wang, J.; Xu, J.; Goodman, M. D.; Chen, Y.; Cai, M.; Shinar, J.; Lin, Z. Q., A simple biphasic route to water soluble dithiocarbamate functionalized quantum dots. *J. Mater. Chem.* **2008**, *18*, 3270
45. Yu, W. W.; Wang, Y. A.; Peng, X., Formation and Stability of Size-, Shape-, and Structure-Controlled CdTe Nanocrystals: Ligand Effects on Monomers and Nanocrystals. *Chem. Mater.* **2003**, *15* (22), 4300-4308.
46. (a) Schaller, R. D.; Klimov, V. I., High Efficiency Carrier Multiplication in PbSe Nanocrystals: Implications for Solar Energy Conversion. *Phys. Rev. Lett.* **2004**, *92* (18), 186601; (b) Ellingson, R. J.; Beard, M. C.; Johnson, J. C.; Yu, P.; Micic, O. I.; Nozik, A. J.; Shabaev, A.; Efros, A. L., Highly Efficient Multiple Exciton Generation in Colloidal PbSe and PbS Quantum Dots. *Nano Lett.* **2005**, *5* (5), 865-871.
47. (a) Vayssieres, L., Growth of Arrayed Nanorods and Nanowires of ZnO from Aqueous Solutions. *Adv. Mater.* **2003**, *15* (5), 464-466; (b) Özgür, Ü.; Alivov, Y. I.; Liu, C.; Teke, A.; Reshchikov, M. A.; Doğan, S.; Avrutin, V.; Cho, S.-J.; Morkoç, H., A comprehensive review of ZnO materials and devices. *J. Appl. Phys.* **2005**, *98* (4), 041301; (c) Beek, W. J. E.; Wienk, M. M.; Janssen, R. A. J., Hybrid Solar Cells from Regioregular Polythiophene and ZnO Nanoparticles. *Adv. Funct. Mater.* **2006**, *16* (8), 1112-1116.
48. (a) Ahn, T.-S.; Wright, N.; Bardeen, C. J., The effects of orientational and energetic disorder on Forster energy migration along a one-dimensional lattice. *Chem. Phys. Lett.* **2007**, *446* (1–3), 43-48; (b) Brandenburg, J. E.; Jin, X.; Kruszynska, M.; Ohland, J.; Kolny-Olesiak, J.; Riedel, I.; Borchert, H.; Parisi, J., Influence of particle size in hybrid solar cells composed of CdSe nanocrystals and poly(3-hexylthiophene). *J. Appl. Phys.* **2011**, *110* (6), 064509.
49. (a) Britt, J.; Ferekides, C., Thin-film CdS/CdTe solar cell with 15.8% efficiency. *Appl. Phys. Lett.*

**1993**, 62 (22), 2851-2852; (b) Huynh, W. U.; Dittmer, J. J.; Teclamarium, N.; Milliron, D. J.; Alivisatos, A. P.; Barnham, K. W. J., Charge transport in hybrid nanorod-polymer composite photovoltaic cells. *Phys. Rev. B* **2003**, 67 (11), 115326; (c) Li, Z.; Gao, F.; Greenham, N. C.; McNeill, C. R., Comparison of the Operation of Polymer/Fullerene, Polymer/Polymer, and Polymer/Nanocrystal Solar Cells: A Transient Photocurrent and Photovoltage Study. *Adv. Funct. Mater.* **2011**, 21 (8), 1419-1431.

50. (a) Kalyuzhny, G.; Murray, R. W., Ligand Effects on Optical Properties of CdSe Nanocrystals. *J. Phys. Chem. B* **2005**, 109 (15), 7012-7021; (b) Puzder, A.; Williamson, A. J.; Zaitseva, N.; Galli, G.; Manna, L.; Alivisatos, A. P., The Effect of Organic Ligand Binding on the Growth of CdSe Nanoparticles Probed by Ab Initio Calculations. *Nano Lett.* **2004**, 4 (12), 2361-2365; (c) Munro, A. M.; Jen-La Plante, I.; Ng, M. S.; Ginger, D. S., Quantitative Study of the Effects of Surface Ligand Concentration on CdSe Nanocrystal Photoluminescence. *J. Phys. Chem. C* **2007**, 111 (17), 6220-6227; (d) Janssen, R. A. J.; Nelson, J., Factors Limiting Device Efficiency in Organic Photovoltaics. *Advanced Materials* **2013**, 25 (13), 1847-1858; (e) Reiss, P.; Couderc, E.; De Girolamo, J.; Pron, A., Conjugated polymers/semiconductor nanocrystals hybrid materials-preparation, electrical transport properties and applications. *Nanoscale* **2011**, 3 (2), 446-489; (f) Glatthaar, M.; Riede, M.; Keegan, N.; Sylvester-Hvid, K.; Zimmermann, B.; Niggemann, M.; Hinsch, A.; Gombert, A., Efficiency limiting factors of organic bulk heterojunction solar cells identified by electrical impedance spectroscopy. *Sol Energ Mat Sol C* **2007**, 91 (5), 390-393; (g) Heinemann, M. D.; von Maydell, K.; Zutz, F.; Kolny-Olesiak, J.; Borchert, H.; Riedel, I.; Parisi, J., Photo-induced Charge Transfer and Relaxation of Persistent Charge Carriers in Polymer/Nanocrystal Composites for Applications in Hybrid Solar Cells. *Adv. Funct. Mater.* **2009**, 19 (23), 3788-3795.

51. Zhang, Q.; Russell, T. P.; Emrick, T., Synthesis and Characterization of CdSe Nanorods Functionalized with Regioregular Poly(3-hexylthiophene). *Chem. Mater.* **2007**, 19 (15), 3712-3716.

52. Querner, C.; Benedetto, A.; Demadrille, R.; Rannou, P.; Reiss, P., Carbodithioate-Containing Oligo- and Polythiophenes for Nanocrystals' Surface Functionalization. *Chem. Mater.* **2006**, 18 (20), 4817-4826.

53. Milliron, D. J.; Alivisatos, A. P.; Pitois, C.; Edder, C.; Fréchet, J. M. J., Electroactive Surfactant Designed to Mediate Electron Transfer Between CdSe Nanocrystals and Organic Semiconductors. *Adv. Mater.* **2003**, 15 (1), 58-61.

54. Yang, J.; Tang, A.; Zhou, R.; Xue, J., Effects of nanocrystal size and device aging on performance of hybrid poly(3-hexylthiophene):CdSe nanocrystal solar cells. *Sol Energ Mat Sol C* **2011**, 95 (2), 476-482.

55. (a) Oosterhout, S. D.; Wienk, M. M.; van Bavel, S. S.; Thiedmann, R.; Jan Anton Koster, L.; Gilot, J.; Loos, J.; Schmidt, V.; Janssen, R. A. J., The effect of three-dimensional morphology on the efficiency of hybrid polymer solar cells. *Nat. Mater.* **2009**, 8 (10), 818-824; (b) Beek, W. J. E.; Slooff, L. H.; Wienk, M. M.; Kroon, J. M.; Janssen, R. A. J., Hybrid Solar Cells Using a Zinc Oxide Precursor and a Conjugated Polymer. *Adv. Funct. Mater.* **2005**, 15 (10), 1703-1707; (c) van Hal, P. A.; Wienk, M. M.; Kroon, J. M.; Verhees, W. J. H.; Slooff, L. H.; van Gennip, W. J. H.; Jonkheijm, P.; Janssen, R. A. J., Photoinduced Electron Transfer and Photovoltaic Response of a MDMO-PPV:TiO<sub>2</sub> Bulk-Heterojunction. *Adv. Mater.* **2003**, 15 (2), 118-121.

56. (a) Atwater, H. A.; Polman, A., Plasmonics for improved photovoltaic devices. *Nat. Mater.* **2010**, 9 (3), 205-213; (b) Ferry, V. E.; Sweatlock, L. A.; Pacifici, D.; Atwater, H. A., Plasmonic Nanostructure Design for Efficient Light Coupling into Solar Cells. *Nano Lett.* **2008**, 8 (12), 4391-4397.

57. (a) Chan, G. H.; Zhao, J.; Schatz, G. C.; Duyne, R. P. V., Localized Surface Plasmon Resonance Spectroscopy of Triangular Aluminum Nanoparticles. *J. Phys. Chem. C* **2008**, 112 (36), 13958-13963; (b) Ekinci, Y.; Solak, H. H.; Löffler, J. F., Plasmon resonances of aluminum nanoparticles and nanorods. *J. Appl. Phys.* **2008**, 104 (8), 083107.

58. (a) Duche, D.; Torchio, P.; Escoubas, L.; Monestier, F.; Simon, J.-J.; Flory, F.; Mathian, G., Improving light absorption in organic solar cells by plasmonic contribution. *Sol Energ Mat Sol C* **2009**, *93* (8), 1377-1382; (b) Rand, B. P.; Peumans, P.; Forrest, S. R., Long-range absorption enhancement in organic tandem thin-film solar cells containing silver nanoclusters. *J. Appl. Phys.* **2004**, *96* (12), 7519-7526.
59. (a) Khanna, P. K.; Gaikwad, S.; Adhyapak, P. V.; Singh, N.; Marimuthu, R., Synthesis and characterization of copper nanoparticles. *Mater. Lett.* **2007**, *61* (25), 4711-4714; (b) Notarianni, M.; Vernon, K.; Chou, A.; Aljada, M.; Liu, J.; Motta, N., Plasmonic effect of gold nanoparticles in organic solar cells. *Sol. Energy* **2014**, *106* (0), 23-37; (c) Chan, G. H.; Zhao, J.; Hicks, E. M.; Schatz, G. C.; Van Duyne, R. P., Plasmonic Properties of Copper Nanoparticles Fabricated by Nanosphere Lithography. *Nano Lett.* **2007**, *7* (7), 1947-1952.
60. Shen, H.; Bienstman, P.; Maes, B., Plasmonic absorption enhancement in organic solar cells with thin active layers. *J. Appl. Phys.* **2009**, *106* (7), 073109.
61. Kim, K.; Carroll, D. L., Roles of Au and Ag nanoparticles in efficiency enhancement of poly(3-octylthiophene)/C60 bulk heterojunction photovoltaic devices. *Appl. Phys. Lett.* **2005**, *87* (20), 203113.
62. Wang, C. C. D.; Choy, W. C. H.; Duan, C.; Fung, D. D. S.; Sha, W. E. I.; Xie, F.-X.; Huang, F.; Cao, Y., Optical and electrical effects of gold nanoparticles in the active layer of polymer solar cells. *J. Mater. Chem.* **2012**, *22* (3), 1206-1211.
63. Topp, K.; Borchert, H.; Johnen, F.; Tunc, A. V.; Knipper, M.; von Hauff, E.; Parisi, J.; Al-Shamery, K., Impact of the Incorporation of Au Nanoparticles into Polymer/Fullerene Solar Cells†. *J. Phys. Chem. A* **2009**, *114* (11), 3981-3989.
64. Nicholson, P. G.; Ruiz, V.; Macpherson, J. V.; Unwin, P. R., Enhanced visible photoluminescence in ultrathin poly(3-hexylthiophene) films by incorporation of Au nanoparticles. *Chem. Commun.* **2005**, (8), 1052-1054.
65. (a) Nam, M.; Park, J.; Kim, S.-W.; Lee, K., Broadband-absorbing hybrid solar cells with efficiency greater than 3% based on a bulk heterojunction of PbS quantum dots and a low-bandgap polymer. *J. Mater. Chem. A* **2014**, *2* (11), 3978-3985; (b) Noone, K. M.; Strein, E.; Anderson, N. C.; Wu, P.-T.; Jenekhe, S. A.; Ginger, D. S., Broadband Absorbing Bulk Heterojunction Photovoltaics Using Low-Bandgap Solution-Processed Quantum Dots. *Nano Lett.* **2010**, *10* (7), 2635-2639; (c) Guchhait, A.; Rath, A. K.; Pal, A. J., Near-IR activity of hybrid solar cells: Enhancement of efficiency by dissociating excitons generated in PbS nanoparticles. *Appl. Phys. Lett.* **2010**, *96* (7), 073505; (d) Jangwon, S.; Sung Jin, K.; Won Jin, K.; Rohit, S.; Marek, S.; Alexander, N. C.; Paras, N. P., Enhancement of the photovoltaic performance in PbS nanocrystal:P3HT hybrid composite devices by post-treatment-driven ligand exchange. *Nanotechnology* **2009**, *20* (9), 095202.
66. Nam, M.; Park, J.; Kim, S.-W.; Lee, K., Broadband-absorbing hybrid solar cells with efficiency greater than 3% based on a bulk heterojunction of PbS quantum dots and a low-bandgap polymer. *Journal of Materials Chemistry A* **2014**, *2* (11), 3978-3985.
67. (a) Lee, J.; Jadhav, P.; Reusswig, P. D.; Yost, S. R.; Thompson, N. J.; Congreve, D. N.; Hontz, E.; Van Voorhis, T.; Baldo, M. A., Singlet Exciton Fission Photovoltaics. *Accounts Chem Res* **2013**, *46* (6), 1300-1311; (b) Chan, W.-L.; Ligges, M.; Jailaubekov, A.; Kaake, L.; Miaja-Avila, L.; Zhu, X.-Y., Observing the Multiexciton State in Singlet Fission and Ensuing Ultrafast Multielectron Transfer. *Science* **2011**, *334* (6062), 1541-1545.
68. Shockley, W.; Queisser, H. J., Detailed Balance Limit of Efficiency of p-n Junction Solar Cells. *J.*

*Appl. Phys.* **1961**, 32 (3), 510-519.

69. Wilson, M. W. B.; Rao, A.; Clark, J.; Kumar, R. S. S.; Brida, D.; Cerullo, G.; Friend, R. H., Ultrafast Dynamics of Exciton Fission in Polycrystalline Pentacene. *J. Am. Chem. Soc.* **2011**, 133 (31), 11830-11833.

70. (a) Ehrler, B.; Wilson, M. W. B.; Rao, A.; Friend, R. H.; Greenham, N. C., Singlet Exciton Fission-Sensitized Infrared Quantum Dot Solar Cells. *Nano Lett.* **2012**, 12 (2), 1053-1057; (b) Ehrler, B.; Walker, B. J.; Böhm, M. L.; Wilson, M. W. B.; Vaynzof, Y.; Friend, R. H.; Greenham, N. C., In situ measurement of exciton energy in hybrid singlet-fission solar cells. *Nat. Commun.* **2012**, 3, 1019.

71. Sun, B.; Marx, E.; Greenham, N. C., Photovoltaic Devices Using Blends of Branched CdSe Nanoparticles and Conjugated Polymers. *Nano Lett.* **2003**, 3 (7), 961-963.

72. (a) Takanezawa, K.; Hirota, K.; Wei, Q.-S.; Tajima, K.; Hashimoto, K., Efficient Charge Collection with ZnO Nanorod Array in Hybrid Photovoltaic Devices. *J. Phys. Chem. C* **2007**, 111 (19), 7218-7223; (b) Coakley, K. M.; Liu, Y.; McGehee, M. D.; Frindell, K. L.; Stucky, G. D., Infiltrating Semiconducting Polymers into Self-Assembled Mesoporous Titania Films for Photovoltaic Applications. *Adv. Funct. Mater.* **2003**, 13 (4), 301-306.

73. Yi, Z.; Yunchao, L.; Haizheng, Z.; Jianhui, H.; Yuqin, D.; Chunhe, Y.; Yongfang, L., Hybrid nanocrystal/polymer solar cells based on tetrapod-shaped CdSe x Te 1- x nanocrystals. *Nanotechnology* **2006**, 17 (16), 4041.

74. Ravirajan, P.; Peiró, A. M.; Nazeeruddin, M. K.; Graetzel, M.; Bradley, D. D. C.; Durrant, J. R.; Nelson, J., Hybrid Polymer/Zinc Oxide Photovoltaic Devices with Vertically Oriented ZnO Nanorods and an Amphiphilic Molecular Interface Layer. *J. Phys. Chem. B* **2006**, 110 (15), 7635-7639.

75. (a) Baranov, D.; Fiore, A.; van Huis, M.; Giannini, C.; Falqui, A.; Lafont, U.; Zandbergen, H.; Zanella, M.; Cingolani, R.; Manna, L., Assembly of Colloidal Semiconductor Nanorods in Solution by Depletion Attraction. *Nano Lett.* **2010**, 10 (2), 743-749; (b) Baker, J. L.; Widmer-Cooper, A.; Toney, M. F.; Geissler, P. L.; Alivisatos, A. P., Device-Scale Perpendicular Alignment of Colloidal Nanorods. *Nano Lett.* **2009**, 10 (1), 195-201; (c) Singh, A.; Gunning, R. D.; Ahmed, S.; Barrett, C. A.; English, N. J.; Garate, J.-A.; Ryan, K. M., Controlled semiconductor nanorod assembly from solution: influence of concentration, charge and solvent nature. *J. Mater. Chem.* **2012**, 22 (4), 1562-1569; (d) Modestino, M. A.; Chan, E. R.; Hexemer, A.; Urban, J. J.; Segalman, R. A., Controlling Nanorod Self-Assembly in Polymer Thin Films. *Macromolecules* **2011**, 44 (18), 7364-7371.

76. (a) Hu, Z.; Fischbein, M. D.; Querner, C.; Drndić, M., Electric-Field-Driven Accumulation and Alignment of CdSe and CdTe Nanorods in Nanoscale Devices. *Nano Lett.* **2006**, 6 (11), 2585-2591; (b) Artemyev, M.; Möller, B.; Woggon, U., Unidirectional Alignment of CdSe Nanorods. *Nano Lett.* **2003**, 3 (4), 509-512; (c) WangWang; Summers, C. J.; Wang, Z. L., Large-Scale Hexagonal-Patterned Growth of Aligned ZnO Nanorods for Nano-optoelectronics and Nanosensor Arrays. *Nano Lett.* **2004**, 4 (3), 423-426; (d) Ahmed, W.; Kooij, E. S.; van Silfhout, A.; Poelsema, B., Quantitative Analysis of Gold Nanorod Alignment after Electric Field-Assisted Deposition. *Nano Lett.* **2009**, 9 (11), 3786-3794.

77. (a) Ahmed, S.; Ryan, K. M., Centimetre scale assembly of vertically aligned and close packed semiconductor nanorods from solution. *Chem. Commun.* **2009**, (42), 6421-6423; (b) Ryan, K. M.; Mastroianni, A.; Stancil, K. A.; Liu, H.; Alivisatos, A. P., Electric-Field-Assisted Assembly of Perpendicularly Oriented Nanorod Superlattices. *Nano Lett.* **2006**, 6 (7), 1479-1482.

78. Gupta, S.; Zhang, Q.; Emrick, T.; Russell, T. P., "Self-Corralling" Nanorods under an Applied

Electric Field. *Nano Lett.* **2006**, 6 (9), 2066-2069.

79. (a) von Hauff, E.; Dyakonov, V.; Parisi, J., Study of field effect mobility in PCBM films and P3HT:PCBM blends. *Sol Energ Mat Sol C* **2005**, 87 (1-4), 149-156; (b) Goh, C.; Kline, R. J.; McGehee, M. D.; Kadnikova, E. N.; Fréchet, J. M. J., Molecular-weight-dependent mobilities in regioregular poly(3-hexyl-thiophene) diodes. *Appl. Phys. Lett.* **2005**, 86 (12), 122110; (c) Schafferhans, J.; Baumann, A.; Wagenpfahl, A.; Deibel, C.; Dyakonov, V., Oxygen doping of P3HT:PCBM blends: Influence on trap states, charge carrier mobility and solar cell performance. *Org. Electron.* **2010**, 11 (10), 1693-1700; (d) Assadi, A.; Svensson, C.; Willander, M.; Inganäs, O., Field-effect mobility of poly(3-hexylthiophene). *Appl. Phys. Lett.* **1988**, 53 (3), 195-197; (e) Kline, R. J.; McGehee, M. D.; Kadnikova, E. N.; Liu, J.; Fréchet, J. M. J., Controlling the Field-Effect Mobility of Regioregular Polythiophene by Changing the Molecular Weight. *Adv. Mater.* **2003**, 15 (18), 1519-1522.

80. Ihn, K. J.; Moulton, J.; Smith, P., Whiskers of poly(3-alkylthiophene)s. *J. Polym. Sci., Part B: Polym. Phys.* **1993**, 31 (6), 735-742.

81. Sun, B.; Greenham, N. C., Improved efficiency of photovoltaics based on CdSe nanorods and poly(3-hexylthiophene) nanofibers. *Phys. Chem. Chem. Phys.* **2006**, 8 (30), 3557-3560.

82. Kim, J.; Yu, K.; Kim, H.; Kwon, S.; Kim, G.; Kwon, K.; Lee, K., Efficient Charge Extraction in Thick Bulk Heterojunction Solar Cells through Infiltrated Diffusion Doping. *Adv. Eng. Mater.* **2014**, 10.1002/aenm.201301502.

83. Dayal, S.; Kopidakis, N.; Olson, D. C.; Ginley, D. S.; Rumbles, G., Photovoltaic Devices with a Low Band Gap Polymer and CdSe Nanostructures Exceeding 3% Efficiency. *Nano Letters* **2009**, 10 (1), 239-242.

84. Carbone, L.; Kudera, S.; Carlino, E.; Parak, W. J.; Giannini, C.; Cingolani, R.; Manna, L., Multiple Wurtzite Twinning in CdTe Nanocrystals Induced by Methylphosphonic Acid. *J. Am. Chem. Soc.* **2005**, 128 (3), 748-755.

85. (a) Loewe, R. S.; Ewbank, P. C.; Liu, J.; Zhai, L.; McCullough, R. D., Regioregular, Head-to-Tail Coupled Poly(3-alkylthiophenes) Made Easy by the GRIM Method: Investigation of the Reaction and the Origin of Regioselectivity. *Macromolecules* **2001**, 34 (13), 4324-4333; (b) Loewe, R. S.; Khersonsky, S. M.; McCullough, R. D., A Simple Method to Prepare Head-to-Tail Coupled, Regioregular Poly(3-alkylthiophenes) Using Grignard Metathesis. *Adv. Mater.* **1999**, 11 (3), 250-253.

86. Shieh, F.; Saunders, A. E.; Korgel, B. A., General Shape Control of Colloidal CdS, CdSe, CdTe Quantum Rods and Quantum Rod Heterostructures. *J. Phys. Chem. B* **2005**, 109 (18), 8538-8542.

87. Khan, M. T.; Kaur, A.; Dhawan, S. K.; Chand, S., In-Situ growth of cadmium telluride nanocrystals in poly(3-hexylthiophene) matrix for photovoltaic application. *J. Appl. Phys.* **2011**, 110 (4), 044509-1-044509-7.

88. (a) Manna, L.; Milliron, D. J.; Meisel, A.; Scher, E. C.; Alivisatos, A. P., Controlled growth of tetrapod-branched inorganic nanocrystals. *Nat Mater* **2003**, 2 (6), 382-385; (b) Manna, L.; Scher, E. C.; Alivisatos, A. P., Synthesis of Soluble and Processable Rod-, Arrow-, Teardrop-, and Tetrapod-Shaped CdSe Nanocrystals. *Journal of the American Chemical Society* **2000**, 122 (51), 12700-12706.

89. Dang, C.; Lee, J.; Breen, C.; Steckel, J. S.; Coe-Sullivan, S.; Nurmikko, A., Red, green and blue lasing enabled by single-exciton gain in colloidal quantum dot films. *Nat Nano* **2012**, 7 (5), 335-339.

90. Meinardi, F.; Colombo, A.; Velizhanin, K. A.; Simonutti, R.; Lorenzon, M.; Beverina, L.; Viswanatha, R.; Klimov, V. I.; Brovelli, S., Large-area luminescent solar concentrators based on  $\lambda$ Stokes-shift-engineered/ nanocrystals in a mass-polymerized PMMA matrix. *Nat Photon* **2014**, *8* (5), 392-399.
91. Pal, B. N.; Ghosh, Y.; Brovelli, S.; Laocharoensuk, R.; Klimov, V. I.; Hollingsworth, J. A.; Htoon, H., 'Giant' CdSe/CdS Core/Shell Nanocrystal Quantum Dots As Efficient Electroluminescent Materials: Strong Influence of Shell Thickness on Light-Emitting Diode Performance. *Nano Letters* **2011**, *12* (1), 331-336.
92. Ivanov, S. A.; Nanda, J.; Piryatinski, A.; Achermann, M.; Balet, L. P.; Bezel, I. V.; Anikeeva, P. O.; Tretiak, S.; Klimov, V. I., Light Amplification Using Inverted Core/Shell Nanocrystals: Towards Lasing in the Single-Exciton Regime. *The Journal of Physical Chemistry B* **2004**, *108* (30), 10625-10630.
93. Zhang, Y.; Li, Y.; Yan, X.-P., Aqueous Layer-by-Layer Epitaxy of Type-II CdTe/CdSe Quantum Dots with Near-Infrared Fluorescence for Bioimaging Applications. *Small* **2009**, *5* (2), 185-189.
94. Xie, R.; Kolb, U.; Li, J.; Basché, T.; Mews, A., Synthesis and Characterization of Highly Luminescent CdSe-Core CdS/Zn<sub>0.5</sub>Cd<sub>0.5</sub>S/ZnS Multishell Nanocrystals. *Journal of the American Chemical Society* **2005**, *127* (20), 7480-7488.
95. Yu, W. W.; Qu, L.; Guo, W.; Peng, X., Experimental Determination of the Extinction Coefficient of CdTe, CdSe, and CdS Nanocrystals. *Chemistry of Materials* **2003**, *15* (14), 2854-2860.
96. (a) Reiss, P.; Bleuse, J.; Pron, A., Highly Luminescent CdSe/ZnSe Core/Shell Nanocrystals of Low Size Dispersion. *Nano Letters* **2002**, *2* (7), 781-784; (b) Dabbousi, B. O.; Rodriguez-Viejo, J.; Mikulec, F. V.; Heine, J. R.; Mattoussi, H.; Ober, R.; Jensen, K. F.; Bawendi, M. G., (CdSe)ZnS Core-Shell Quantum Dots: Synthesis and Characterization of a Size Series of Highly Luminescent Nanocrystallites. *The Journal of Physical Chemistry B* **1997**, *101* (46), 9463-9475.
97. Chen, Y.; Vela, J.; Htoon, H.; Casson, J. L.; Werder, D. J.; Bussian, D. A.; Klimov, V. I.; Hollingsworth, J. A., "Giant" Multishell CdSe Nanocrystal Quantum Dots with Suppressed Blinking. *Journal of the American Chemical Society* **2008**, *130* (15), 5026-5027.
98. She, C.; Fedin, I.; Dolzhenkov, D. S.; Demortière, A.; Schaller, R. D.; Pelton, M.; Talapin, D. V., Low-Threshold Stimulated Emission Using Colloidal Quantum Wells. *Nano Letters* **2014**, *14* (5), 2772-2777.
99. Bae, W. K.; Char, K.; Hur, H.; Lee, S., Single-Step Synthesis of Quantum Dots with Chemical Composition Gradients. *Chemistry of Materials* **2008**, *20* (2), 531-539.
100. Peng, Z. A.; Peng, X., Formation of High-Quality CdTe, CdSe, and CdS Nanocrystals Using CdO as Precursor. *Journal of the American Chemical Society* **2000**, *123* (1), 183-184.
101. Bae, W. K.; Nam, M. K.; Char, K.; Lee, S., Gram-Scale One-Pot Synthesis of Highly Luminescent Blue Emitting Cd<sub>1-x</sub>Zn<sub>x</sub>S/ZnS Nanocrystals. *Chemistry of Materials* **2008**, *20* (16), 5307-5313.
102. (a) Silva, A. C. A.; da Silva, S. W.; Morais, P. C.; Dantas, N. O., Shell Thickness Modulation in Ultrasmall CdSe/CdS<sub>x</sub>Se<sub>1-x</sub>/CdS Core/Shell Quantum Dots via 1-Thioglycerol. *ACS Nano* **2014**, *8* (2), 1913-1922; (b) Bae, W. K.; Padilha, L. A.; Park, Y.-S.; McDaniel, H.; Robel, I.; Pietryga, J. M.; Klimov, V. I., Controlled Alloying of the Core-Shell Interface in CdSe/CdS Quantum Dots for Suppression of Auger Recombination. *ACS Nano* **2013**, *7* (4), 3411-3419; (c) Boldt, K.; Kirkwood, N.; Beane, G. A.; Mulvaney,

P., Synthesis of Highly Luminescent and Photo-Stable, Graded Shell CdSe/Cd<sub>x</sub>Zn<sub>1-x</sub>S Nanoparticles by In Situ Alloying. *Chemistry of Materials* **2013**, 25 (23), 4731-4738.

## **VITA**

### **Jaehan Jung**

Jaehan was born in Pohang, Korea. He received B.S. in Materials Science and Engineering from Seoul National University in 2010. He first pursued a doctoral degree in Materials Science Engineering at Iowa State University at 2010, then transfer to Materials Science and Engineering at Georgia Institute of Technology in 2011.